Fatigue Behaviour of the Web-to-Flange Junction in a Glass Fibre-Reinforced Polymer Web-Core Sandwich Panel Bridge Deck Subjected to Bending

Delft University of Technology Master Thesis

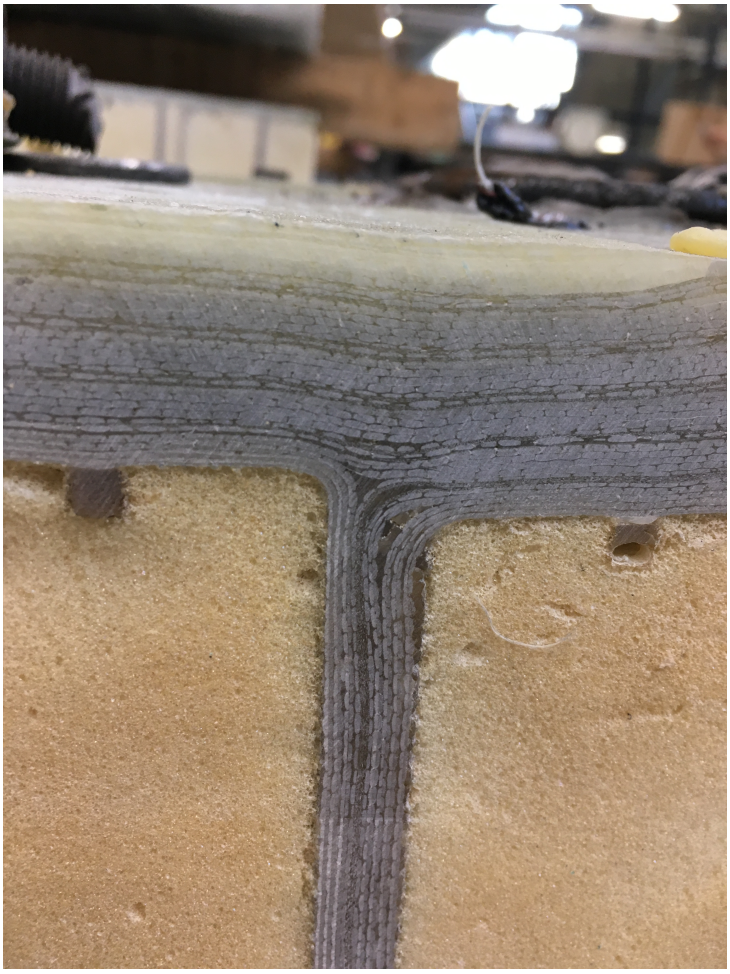

FATIGUE BEHAVIOUR OF THE WEB-TO-FLANGE JUNCTION IN A GLASS FIBRE-REINFORCED POLYMER WEB-CORE SANDWICH PANEL BRIDGE DECK SUBJECTED TO BENDING

DELFT UNIVERSITY OF TECHNOLOGY MASTER THESIS

to obtain the degree of Master of Science
at Delft University of Technology,
to be defended publicly on the 20th of August 2024

by

T.J. WHITE

Student number: 5411416

Thesis committee:

Dr. M. (Marko) Pavlović	First supervisor	Technical University of Delft
Dr.ir. F.P. (Frans) van der Meer	Second supervisor	Technical University of Delft
Dr. O. (Olena) Karpenko	Daily supervisor	Technical University of Delft

External committee members:

ir. E. (Liesbeth) Tromp	Company supervisor	RoyalHaskoningDHV
ir. LB (Lieuwe) Cornelissen	Daily supervisor	RoyalHaskoningDHV

dhr. G. (Giorgos) Stamoulis has significantly contributed to the creation of the dissertation.

CONTENTS

List of Figures

LIST OF TABLES

ABSTRACT

Many steel bridges in the Netherlands, built in the 1950s and 1960s, are nearing the end of their service life, with steel bridge decks suffering from fatigue damage due to high traffic loads. Replacing these decks with Glass Fibre Reinforced Polymer (GFRP) Web-Core Sandwich Panel (WCSP) decks is a potential solution due to their superior strength-to-weight ratio and better in-plane fatigue performance.

A critical aspect of using these bridge decks safely is verifying the fatigue life of the Web-to-Flange Junctions (WFJs), which connect the webs to the facing. Fatigue damage is known to occur in such components with changing cross-sections, leading to stress concentrations. Current design codes lack verification equations or S-N curves for this component, necessitating further research.

This research investigates the static an fatigue performance of the WFJ by performing tests and identifying key parameters influencing this response. Through testing, the static bending moment resistance and the dominant failure mode are determined. Using the safe life approach, an S-N curve is generated by measuring the number of cycles until crack initiation occurred during cyclic loading.

Static tests revealed a constant rotational stiffness followed by a significant reduction due to delamination. Fatigue tests showed progressive stiffness degradation and crack propagation, with some crack retardation indicating a stabilisation phase before ultimate failure. Finite Element Modelling (FEM) accurately predicted initial stiffness but overestimated post-crack rotational stiffness, suggesting the need to incorporate additional parameters like material stiffness degradation or cohesive zone modelling.

This research identified important parameters such as waviness, web thickness, and radius affecting the response of the WFJ. However, testing did not confirm the predicted linear relationships between web thickness, radius and moment resistance as suggested by equations given by Lekhnitskii. Additionally, no direct correlation was found between waviness and moment resistance. It was observed that specimens with greater web thickness often also had higher waviness, and it is hypothesised that these parameters influence each other which would explain the non-linear relationship found from testing. Future research is needed to verify this hypothesis and include methods for quantifying the 'waviness' parameter.

This research enhances the understanding of the static and fatigue behaviour of WFJs in GFRP Web-Core Sandwich Panel bridge decks. The findings reveal that the dominant failure mode of the WFJ subjected to bending is delamination, due to out-of-plane stresses, as predicted by equations given by Lekhnitskii. Therefore, it is suggested that

future design codes for FRPs incorporate these equations and delamination S-N curves to verify the fatigue safety of this component. Additionally, the WFJs were observed to be damage-tolerant, suggesting the potential for alternative design concepts to the fatigue life approach. Static tests revealed that although increased web thickness enhances the strength of the WFJs, it is also correlated with increased waviness, which is found from previous research to reduce strength. Future research could explore acceptable levels of crack growth and rotational stiffness degradation for safe bridge design, contributing to the development of design guidelines for GFRP WCSP, making it more viable to use these bridge decks in bridge renovations.

Keywords: Fibre waviness, GFRP, Bridge decks, Mechanical testing, Web-to-Flange Junction, crack retardation, delamination, static tests, fatigue tests, rotational stiffness, and bending moment resistance.

PREFACE

Dear Reader,

I am proud to present my MSc thesis, "Fatigue Behaviour of the Web-to-Flange Junction in a Glass Fibre-Reinforced Polymer Web-Core Sandwich Panel Bridge Deck Subjected to Bending". This work represents a significant milestone in my academic journey, and I am incredibly proud of the effort and dedication that went into its completion. The research was both challenging and rewarding, demanding considerable time, effort and perseverance.

I would like to express my deepest gratitude to my supervisors: Marko Pavlović, Liesbeth Tromp, Frans van der Meer, Olena Karpenko, and Lieuwe Cornelissen. Their guidance, expertise, and encouragement were invaluable throughout this process. I have learned so much from you. Special thanks are also due to Giogios Stamoulis, the lab technician, for his assistance with my experiments. Thank you for your time and patience. Peter de Vries assisted me in the lab preparations. A big thank you to Angeliki Christoforidou, Mathieu Koetsier and Tjeu Peeters for advising and assisting me. Thank you to Martijn Veltkamp and Nico Koster from Fibercore Europe BV for supplying the WCSP specimens and assisting with the cutting of the specimens. My gratitude extends to RoyalHaskoning DHV for providing me with the opportunity of doing my master thesis in collaboration with them. Specifically my manager Bart-Jan van der Gaag for his support. I would like to thank Vito Ros from RWS for assisting me in finding an interesting case study for my research. I am grateful to my family for their support and understanding. Their encouragement provided me with the strength to overcome the challenges I faced.

Thank you for taking the time to read my thesis. I hope you find it interesting and valuable.

T.J. White
Delft, August 2024

1

INTRODUCTION

1.1. RESEARCH MOTIVATION

1.1.1. RENOVATION CHALLENGE

In the Netherlands there are many bridges built in the 1950s and 1960s that are in need of renovation or replacement due to a combination of increased traffic loads, increased traffic volume and aging infrastructure. The Directorate-General of the Ministry of Infrastructure and Water Management of the Netherlands (Rijkswaterstaat (RWS)) has identified a large number of bridges which are in need of renovation or replacement in the near future. In the report (Rijkswaterstaat, 2022), RWS has identified that they own 17 NK60[1] steel bridges and 65 NK60 concrete bridges that are in need of renovation or replacement and they are expecting to spend €4 billion euros between 2023-2030 for the renovation or replacement of bridges.

1.1.2. USE OF GFRP WCSPS TO RENOVATE EXISTING BRIDGES

The use of Glass Fibre Reinforced Polymer (GFRP) Web-Core Sandwich Panel (WCSP) bridge decks (see Figure 1.1) present an interesting alternative, compared to more traditional materials such as steel and concrete, which could be a viable solution for this renovation challenge (Tromp, 2018). GFRP WCSP bridge decks have a high strength-to-weight ratio and a better in-plane fatigue performance than steel, making them ideal to replace existing bridge decks without significantly increasing the load on existing structures. However, for RWS to consider these GFRP WCSPs as a viable alternative, the safety and performance of these components needs to be validated through testing as widely accepted design codes for GFRP components are still in development. In the past fatigue damage to steel orthotropic decks reduced the fatigue life significantly and caused extensive economic damage. Therefore, it is important to be able to predict the fatigue life of these bridge decks.

[1] This is an abbreviation for 'not class 60', these are bridges that have be design for lower traffic loads than modern day traffic

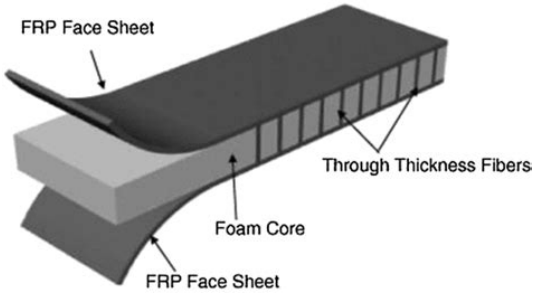

Figure 1.1: FRP Sandwich Panel System (ascelibrary.org)

1.1.3. WHY DO WE SEEN FATIGUE DAMAGE IN JUNCTIONS?

In steel bridges fatigue damage (cracks) is often found at junctions, such as the web-to-deck junction. This is because changes of the geometry in the cross-section lead to complex stress states in the material and high stress concentrations, see Figure 1.2. In steel bridges, these stress concentrations often occur at connections and welds, where the geometry of the structure changes abruptly, leading to localised stress peaks. Over time, the repeated application of traffic loads causes microscopic cracks to initiate at these stress concentration points. As the cycles of loading continue, these small cracks propagate and grow, eventually leading to significant structural damage and potential failure. The cyclic nature of the loads is key to this process, as it progressively weakens the material and leads to fatigue cracking.

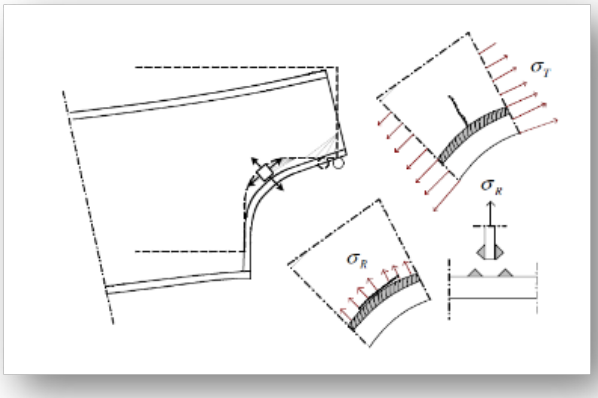

Figure 1.2: Complex stress state in changing cross-section (Haghani et al., 2012)

1.1.4. WHAT DO WE EXPECT FOR GFRP JUNCTIONS?

Fatigue damage in FRP junctions is primarily due to the cyclic stresses and the unique properties of composite materials. Due to the complex stress states occurring in junctions high stress concentrations occur in these junctions as well as Out-Of-Plane (OOP) tensile stresses. FRP laminates are particularly weak to OOP stresses as there are no fibres in this direction and therefore there is a risk of delamination occurring due to these stresses. Therefore, it is expected that WFJs, will be prone to delamination, a failure mode where layers of the composite separate. Due to a bending moment, out-of-plane stresses at these junctions can initiate cracks in the junctions. Over time, these cracks propagate due to the repeated loading, leading to delamination and eventual structural damage. The behaviour of FRP under fatigue is hypothesised to be influenced by factors such as fibre volume fraction, waviness, and web thickness, which affect the distribution and magnitude of stresses. Unlike steel, FRP lacks the ductility and plastic deformation capacity, making it more susceptible to sudden failures once cracks initiate and propagate. Thus, understanding and mitigating delamination through improved design and material optimisation are crucial for the longevity and reliability of FRP junctions in WCSP bridge decks.

1.2. PROBLEM STATEMENT

1.2.1. GAPS IN KNOWLEDGE

While GFRP composites are generally considered to have superior in-plane fatigue life performance compared to steel (Onderzoeksgroep Schoonmeersen, 2020a), predicting their fatigue behaviour is complex due to their anisotropic nature. Compared to steel GFRP components can have multiple fatigue failure modes interact and develop simultaneously (Mandell et al., 2003). On top of this, changes in the geometry of the cross-section of a component such as, joints, connections or junctions introduce peak stresses where small cracks are likely to initiate and propagate due to cyclic loading. Particularly for anisotropic materials such as GFRP composite the direction of these stresses is important as the strength of these materials is not the same in all directions. Especially for junctions as OOP stresses are likely to occur here and in this direction there are no fibres making it making the weakest direction in an FRP composite. Currently there are no specific equations or S-N curves (see Figure 1.3) for OOP-stresses, multi-axial laminates or geometrical details in the design codes for the WFJ component. This makes it harder to verify the fatigue life of this component forcing engineers to verify this component by the means of testing which can be expensive and time consuming.

1.2.2. AIMS OF RESEARCH

Current design codes lack specific S-N curves and guidelines for the Web-to-Flange Junction in a WCSP, leading to uncertainties in predicting their long-term performance and safety. This research aims to address these gaps in knowledge by investigating the static and fatigue performance of the WFJs, identifying key parameters influencing their performance and developing Finite Element Models (FEMs) to predict their behaviour, thereby enhancing the design and application of GFRP components in civil engineering.

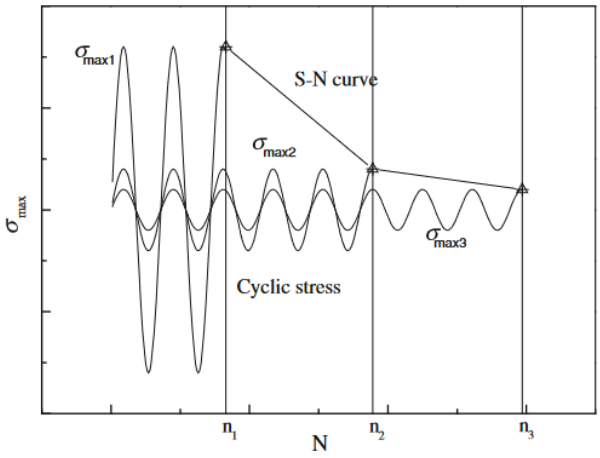

Figure 1.3: S-N curve from tests (Vassilopoulos and Keller, 2011)

1.3. RESEARCH QUESTIONS

The main research question in this study is:

What is the fatigue behaviour of the WFJ in a GFRP WCSP bridge deck subjected to bending?

This question is divided into three sub-questions:

1. What is the static and fatigue response of the WFJ subjected to bending?
2. What are the most important parameters determining this behaviour?
3. Can this behaviour be predicted by Finite Element Modelling (FEM)?

1.4. OBJECTIVES AND DELIVERABLES

The objective of this research is to investigate the fatigue behaviour of the WFJ subjected to bending. This involves understanding the static and fatigue response of the WFJs, identifying the critical parameters that influence their behaviour and developing Finite Element Models to predict this behaviour. The specific objectives include:

1. Determine the static strength, failure modes and rotational stiffness of the WFJ
2. Determine the fatigue life (for various load levels), identify fatigue failure modes, and construct an S-N curve of the WFJ subjected to bending.
3. Identify the most important parameters affecting the fatigue behaviour of the WFJ.

4. Develop and validate FEMs to simulate the static and fatigue response of the WFJ, predict the effects of fatigue damage on the rotational stiffness and durability and to verify the necessary parameters to predict this behaviour.

The deliverables for this research include:

1. Literature Review: A review of the existing knowledge on the materials, production and failure mechanisms, specifically focusing on the WFJ.

2. Test Report: Documentation of the test-setup, procedures, and results, including static and fatigue test data, analysis of failure modes and the constructed S-N curve.

3. Finite Element Models: FEMs that can simulate the rotational response of the damaged and non-damaged WFJs. These models will incorporate key parameters such as web thickness and radii from specific WFJ specimens so the accuracy can be compared to experimental data.

4. Research Report: A research report including the findings, methodology, analysis and conclusions of the study. This report will also address research questions and provide recommendations for the future manufacturing, design and fatigue validation of the WFJ.

1.5. SCOPE

This research project will evaluate existing damage/failure models and/or progressive failure algorithms instead of creating new ones.

Due to the constraints of the available timeline, the goal is to derive one component S-N curve from tests at a constant amplitude load level with an R ratio of R = 0.1. As a result, the consideration of variable amplitude loads, R values, and temperature effects will be excluded.

A component S-N curve will be derived for WFJs obtained from a single WCSP bridge deck fabricated by Fibercore Europe BV. This deck uses one type of unsaturated polyester combined with glass fibre in a supplier-specific lay-up scheme.

More research is needed and recommended to further develop the insights of this research into a more generically applicable S-N curve and predictive method.

2

LITERATURE REVIEW

In this chapter a review will be done on the existing knowledge on the materials, production and failure mechanisms, specifically focusing on the WFJ.

2.1. MATERIALS AND PRODUCTION

2.1.1. FIBRE REINFORCED POLYMER (FRP) COMPOSITES

'Composite materials' are materials composed of two or more constituent materials which are physically distinguishable making them heterogeneous. Combining materials in such a way to preserve their most relevant properties and enhance each other it allows for the creation of highly advantageous products. A well known example of such a product is reinforced concrete where the reinforcing steel gives the composite a high tensile strength and as a secondary benefit the concrete provides fire resistance and corrosion protection, resulting in a highly effective composite material.

Fibre Reinforced Polymer (FRP) composites consist of a polymer resin 'matrix' and reinforcing fibres, see Figure 2.1. The fibres provide stiffness and strength, in the direction of their orientation, and the resin allows for the transfer of the load to the fibres while also protecting the fibres and suppporting them against buckling.

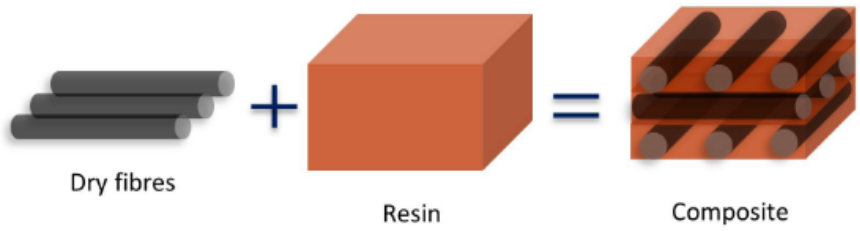

Figure 2.1: constituent components of FRP composite (Bohm et al., 2023)

2.2. FRP WEB-CORE SANDWICH PANEL

An FRP Sandwich Panel is a sandwich structure of two FRP facings running in parallel to each other with a lightweight non-structural core (often a type of foam is used) in between, see Figure 2.2. This is done to increase the height of the structure, thereby increasing the bending stiffness, without increasing the weight of the structure too much, see Figure 2.4. In 'web-core' sandwich panels the core is strengthened by vertical 'webs', connecting the top and bottom facings, hereby increasing the shear strength, resistance to buckling and debonding between the facings and the core, see Figure 2.3. There are multiple ways in which these panels can be designed and produced. In this research the focus will be on web-core sandwich panels designed and produced by FiberCore Europe BV, which has a bespoke and patented lay up scheme including so-called Z-layers explained further on.

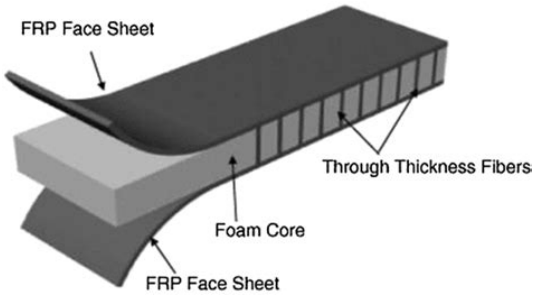

Figure 2.2: FRP Sandwich Panel System (Reis and Rizkalla, 2008)

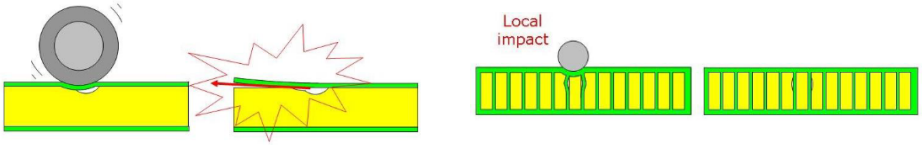

(a) Sandwich Panel (without webs)

(b) Web-Core Sandwich Panel

Figure 2.3: Web-Core vs. non-Web-Core (FiberCore Europe BV, 2007)

MANUFACTURING PROCESS OF FRP WEB-CORE SANDWICH PANEL

The manufacturing of Fibercore Europe web-core sandwich panel decks is done using the vacuum injection technique, see Figure 2.5. Hereby a fibre face sheet is first placed on a mold, which can be curved according to design, to create a curved bridge panel. Then the foam blocks which are wrapped with fibre sheets are placed on the fibre face sheet. After which the second fibre face sheet is placed on top. Then the whole package is sealed in an air-tight bag in which the resin can be infused into the fibre sheets according to the vacuum injection technique, see Figure 2.6.

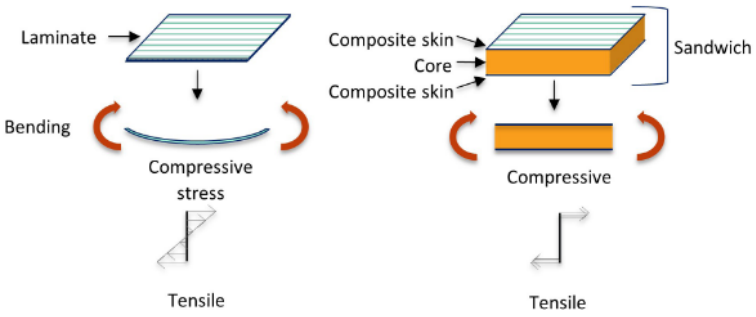

Figure 2.4: Sandwich structure (Bohm et al., 2023)

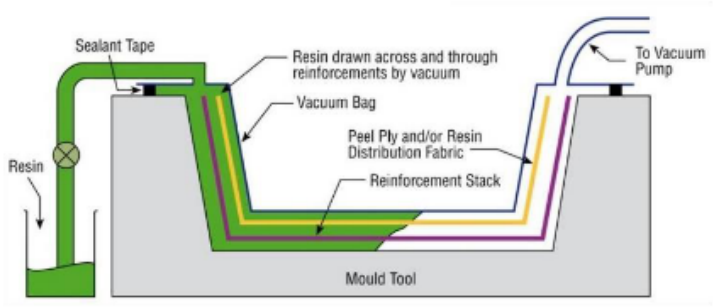

Figure 2.5: Vacuum infusion manufacturing process (FiberCore Europe BV, 2007)

Z-LAYERS

Fibercore Europe has developed a special technique in which some of the fibre layers run from the bottom face sheet, through the webs, and continue in the top face sheet. They call these layers 'Z-layers', and this technique is done to create a stronger connection between the face sheets and the webs, see Figure 2.7. These 'Z-layers' cause the WFJs to be non-symmetrical because they only enter the junction from one side, therefore the side without this 'Z-layer' is less stiff. This will affect the design setup of the WFJ later on.

2.3. THE WEB-TO-FLANGE JUNCTION

The Web-to-Flange Junction (WFJ) is a component in the WCSP which connects the facing of the sandwich panel to the webs, see Figure 2.8. FRP WFJs are composed of two L-junctions connected to the facing of the sandwich panel, with a resin-rich area in between that lacks fibres.

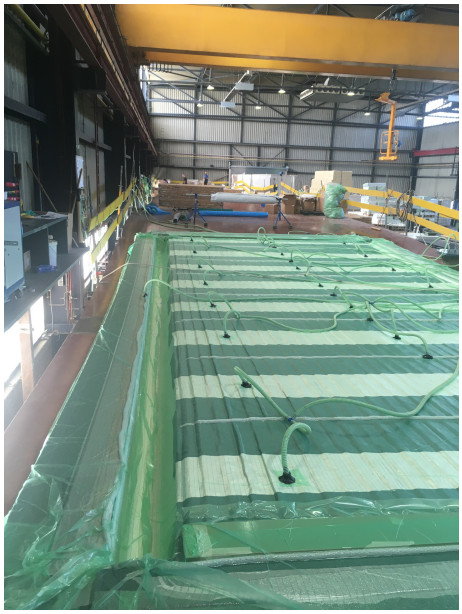

Figure 2.6: Web-Core Sandwich Panel production at Fibercore Europe (photo taken by Tom White)

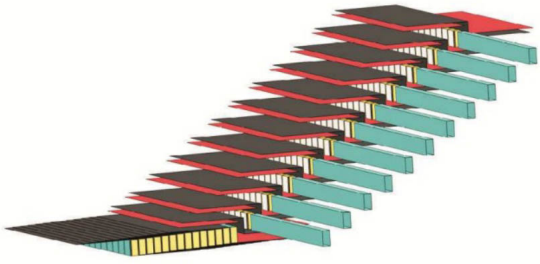

Figure 2.7: Z-layup (FiberCore Europe BV, 2007)

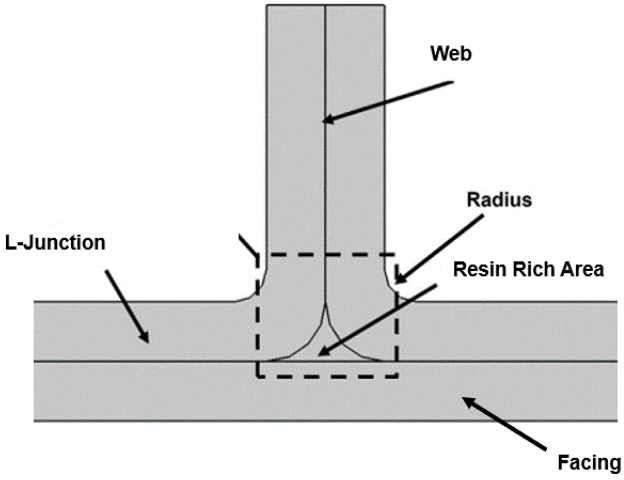

Figure 2.8: Web-to-Flange Junction (Burns et al., 2016)

2.4. MECHANICAL BEHAVIOUR OF FRPS

In general FRPs are anisotropic and inhomogeneous and therefore their behaviour is very different from the mechanical behaviour of metals and other isotropic materials (Vassilopoulos and Keller, 2011).

Because the orientation of the fibres mainly determines the behaviour of the composite, it is an important consideration in the design of FRP laminates. A laminate is constructed from multiple layers known as plies. When all the fibres are orientated in the same direction within the matrix it is referred to as a Unidirectional (UD). FRPs allow the designer to stack plies with different fibre orientations on top of each other, see Figure 2.9, thereby customising the strength and stiffness properties of the laminate in each direction to facilitate the designated function of the material.

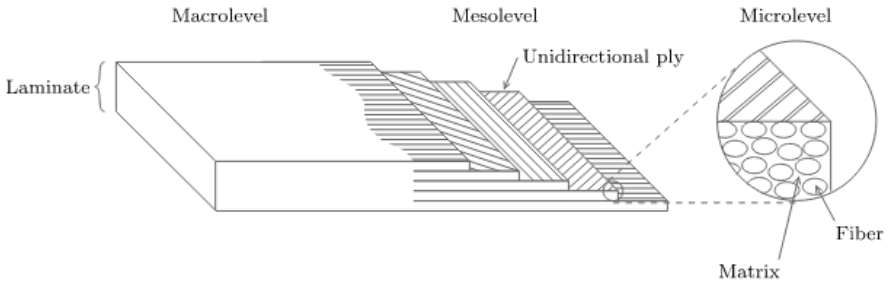

Figure 2.9: Laminate build up (Frans, 2012)

2.4.1. DEFINITION OF REFERENCE AXES IN FRP COMPOSITES

To indicate the orientations of the fibres in the various parts and layers, us is made of the axes conventions defined in the "TS19101: Design of fibre-polymer composite structures"(European Committee for Standardization, 2022).

In Figure 2.10, the convention for the local axes of a (UD) ply are shown. The axes 1 and 2 are the in-plane directions of the ply, with 1 being the direction of the fibre and 2 being the transverse direction to the fibres. Direction 3 is the out-of-plane direction of the ply.

In Figure 2.11, the convention for the global axes for a laminate built up with UD plies is shown. Here the x and y axis are the in-plane axis with the x-axis being the main load bearing direction of the laminate (the longitudinal direction) and y-axis being the transverse direction. The z-axis is for the out-of-plane direction of the laminate. The angle θ defines the orientation of each ply in relation to the laminate direction, measured counterclockwise from the local axis 1 of the ply.

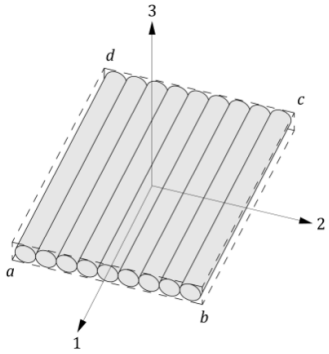

Figure 2.10: Reference axes (local) for UD ply (European Committee for Standardization, 2022)

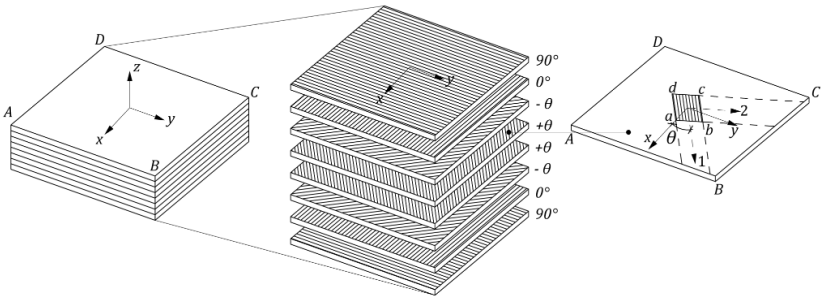

Figure 2.11: Reference axes (global) for laminate layup (European Committee for Standardization, 2022)

2.5. FAILURE MECHANISMS IN FRP COMPOSITES

Unlike metals, FRP does not crack and propagate in a single position but its failure is characterised by multiple failure modes. These are: delamination, matrix failure, fibre pull-out and fibre failure (Vassilopoulos and Keller, 2011). These failure modes can occur simultaneously to accumulate damage in the material. Because this research is on the fatigue behaviour of an FRP component with multi-directional fibre layups in a civil engineering structure, it is important to understand the failure mechanisms that can occur in such an MD laminate. *Fatigue of Fiber-reinforced Composites* (Vassilopoulos and Keller, 2011) describe the types of damage that can develop during the fatigue failure of an MD laminate as:

- **Matrix cracks:** These cracks will initially appear in one of the plies and can be transferred to adjacent plies under high stresses or they will continue to spread throughout the same ply under low stresses. These cracks can develop parallel or transverse to the loading direction and may cause delamination or fibre fractures.

- **Layer delamination:** When the strain field in an MD laminate develops in such a way that not all layers in the laminate can comply with the the strain compatibility equations, interlaminar stresses develop and lead to delamination of adjacent layers. Also delamination can occur when out-of-plain stresses are introduced to the laminate. When this happens the layers will act independently and not as part of a MD laminate. This causes a large reduction to the local moment of inertia and resistance to bending.
- **Interface failure:** Interface failure is when the interface between the matrix and the fibres fails, and cracks occur in this region.
- **Fibre fracture:** This is usually the last stage of damage accumulation in an FRP composite. The fibres are the main load-bearing component in the composite and when they fail the whole material usually fails.

Often the described failure modes happen simultaneously at different locations in the loaded material. Therefore it is not easy to identify the main failure mode of a MD laminate and it is recommended to assign one of the failure modes as the dominant one (Vassilopoulos and Keller, 2011).

The failure mode between the plies (delamination) are those of classical fracture mechanics (Zhang, 2018).The opening mode caused by normal tensile stress (Mode I), the shear mode (Mode II), and the tearing mode (Mode III) as seen in Figure 2.12.

1. Mode I (opening)
2. Mode II (sliding)
3. Mode III (tearing)

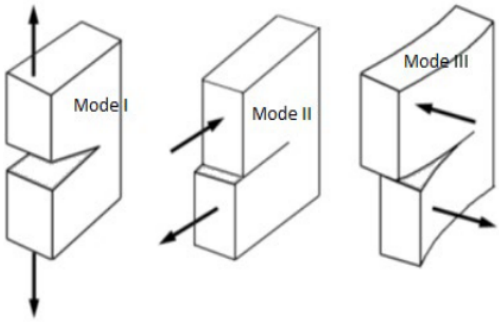

Figure 2.12: FRP composite fracture modes (Zhang, 2018)

2.6. FIBRE WAVINESS AND ITS EFFECT ON WFJ BEHAVIOUR

Bridge decks are typically designed with idealised material properties and structural geometry assumptions. However, manufacturing-induced imperfections, such as waviness, can reduce these design limits. Resin-rich zones and out-of-plane waviness can induce stress concentrations and fibre misalignments, influencing failure. (Coogler et al., 2005) observed that fibre waviness can be particularly pronounced within flange-web joints (WFJs).

Research has been conducted to identify the effect of ply waviness on the ultimate behaviour and stiffness of WFJs. "Fibre waviness in pultruded bridge deck profiles: Geometric characterisation and consequences on ultimate behaviour" (Sebastian, 2018) performed statically determined cantilever bending tests on WFJs in a pultruded GFRP bridge deck. These tests revealed that failure always occurred by fracture of the wavy fibre-resin interfaces within the WFJs. The strongest joint had the least amount of waviness. Additionally, it was found that fibre waviness influences the effective section flexural stiffness and, consequently, the effective material modulus along the flange.

Similarly, (Poulton et al., 2024) conducted cantilever tests on WFJs in a pultruded GFRP bridge deck and found that a 0.8 mm increase in wrinkle amplitude (waviness) led to a 92% increase in peak shear strain, which was the dominant strain in these tests.

In conclusion, fibre waviness can be particularly pronounced in WFJs, inducing stress concentrations that affect failure and reduce the strength of the WFJ component. Tests have shown that WFJs with higher amounts of waviness exhibit decreased strength and that fibre waviness also influences the effective section flexural stiffness.

2.7. APPROACHES TO PREDICTING THE FATIGUE LIFE OF FRPS

For predicting the fatigue life of structural components made of composites, at least three alternative design concepts could be used: the damage-tolerant, fail-safe and the safe-life design concepts (Vassilopoulos and Keller, 2011).

- **damage tolerant;** is where a certain amount of damage is tolerated.
- **fail-safe;** assumes residual strength or stiffness can be correlated to fatigue life via a valid criterion.
- **safe-life;** the effective design stress (S) (or strain) corresponds to number of load cycles (N) via the $S-N$ (or $\epsilon-N$) curve. There must be no noticeable damage due to fatigue during the designed lifetime of the structure.

Currently there is no established methodology for the life prediction of engineering FRP structures (Vassilopoulos and Keller, 2011). Therefore to verify the safety of a structure or component, numerous specimens must be tested until failure, which costs time and money. There are three methods in which these specimens can be analysed to predict their fatigue life:

1. Fatigue Life Prediction based on S-N curves;
2. Phenomenological approach, which is based on material degradation;
3. Progressive Damage Modelling, which models progressive damage in the laminate and crack propagation.

2.8. STRESSES IN A CURVED BEAM

When loads are applied to the curved Web-Flange-Junction (WFJ) a different stress state occurs compared to a straight beam, this is because the curved section of the WFJ. In a straight beam the neutral axis of the section coincides with its centroidal axis and the stress distribution in the beam is linear. However in a curved beam the neutral axis of the section is shifted towards the centre of curvature of the beam causing a non-linear stress distribution (Engineer's Edge, n.d.), see Figure 2.13. This non-linear stress distribution can cause high tensile stresses at the inner radius when a positive bending moment is applied. For isotropic materials this is where the first 'fibre' will likely fail.

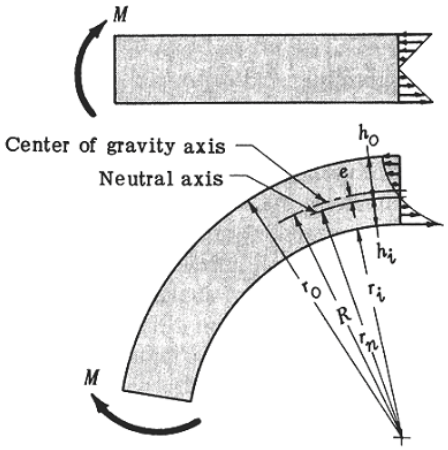

Figure 2.13: Stress in curved beam (Engineer's Edge, n.d.)

2.8.1. STRESSES IN A CURVED BEAM DUE TO BENDING

For an laminated anisotropic material such as FRP also through-thickness tensile stresses could be critical in a curved beam, where these stresses are perpendicular to the fibre direction, which is the weak direction of the material. To calculate these stresses occurring in the curved beam of an anisotropic material due to a bending moment (see Figure 2.14), (Lekhnitskii et al., 1968) give in "*Anisotropic plates*" the following equations (2.1, 2.2, 2.5 and 2.6) to determine the tangential and radial stress distribution in a anisotropic homogeneous curved beam under pure bending. These tangential and radial stress distributions are given for 'open' and 'closed' bending mode in the Figures 2.17 and 2.16.

Equations to calculate the radial (σ_r) and tangential (σ_θ) stresses in a curved beam subjected to a constant bending moment are; equation 2.1 and 2.2.

$$\sigma_r = -\frac{M}{R_o^2 bg}\left(1 - \frac{1-c^{k+1}}{1-c^{2k}}\left(\frac{r}{R_o}\right)^{k-1} - \frac{1-c^{k+1}}{1-c^{2k}}c^{k+1}\left(\frac{R_o}{r}\right)^{k+1}\right) \tag{2.1}$$

$$\sigma_\theta = -\frac{M}{R_o^2 bg}\left(1 - \frac{1-c^{k+1}}{1-c^{2k}}k\left(\frac{r}{R_o}\right)^{k-1} + \frac{1-c^{k+1}}{1-c^{2k}}kc^{k+1}\left(\frac{R_o}{r}\right)^{k+1}\right) \tag{2.2}$$

$$\tau_{r\theta} = 0 \tag{2.3}$$

Where:

$k = \left(\frac{E_\theta}{E_r}\right)^{\frac{1}{2}}$

$c = \frac{R_i}{R_o}$

$g = \frac{1-c^2}{2} - \frac{k}{k+1}\frac{(1-c^{k+1})^2}{1-c^{2k}} + \frac{kc^2}{k-1}\frac{(1-c^{k-1})^2}{1-c^{2k}}$

R_i = inner radius

R_o = outer radius

The radial location where the maximum radial stress occurs is given by:

$$r = \left(\frac{(k+1)(1-c^{k-1})c(R_i R_o)^k}{(k-1)(1-c^{k+1})}\right)^{\frac{1}{2}k} \tag{2.4}$$

Equations for an end load on a curved beam are given by equation 2.5 and 2.6, 2.7 see Figure 2.15

$$\sigma_r = \frac{P}{R_o b g_1}\frac{R_o}{r}\left(\left(\frac{r}{R_o}\right)^\beta + c^\beta\left(\frac{R_o}{r}\right)^\beta - 1 - c^\beta\right)\sin(\theta+\omega) \tag{2.5}$$

$$\sigma_\theta = \frac{P}{R_o b g_1}\frac{R_o}{r}\left((1+\beta)\left(\frac{r}{R_o}\right)^\beta + (1-\beta)c^\beta\left(\frac{R_o}{r}\right)^\beta - 1 - c^\beta\right)\sin(\theta+\omega) \tag{2.6}$$

$$\tau_{r\theta} = \frac{-P}{R_o b g_1}\frac{R_o}{r}\left(\left(\frac{r}{R_o}\right)^\beta + c^\beta\left(\frac{R_o}{r}\right)^\beta - 1 - c^\beta\right)\cos(\theta+\omega) \tag{2.7}$$

The radial location where the maximum radial stress occurs, for $\beta > 1$ is given by:

$$r = \left(\frac{R_o^\beta}{2(1-\beta)}\left(1 + c^\beta - \left((1+c^\beta)^2 + 4c^\beta\left(\beta^2 - 1\right)\right)^{\frac{1}{2}}\right)\right)^{\frac{1}{\beta}} \tag{2.8}$$

Where:

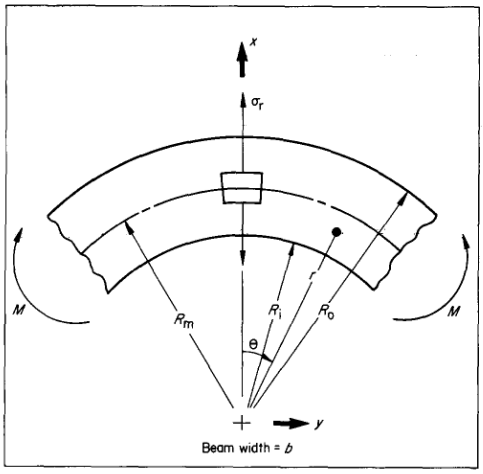

Figure 2.14: Uniform bending moment on curved beam (Kedward et al., 1989)

- $c = \frac{R_i}{R_o}$
- $\beta = \left(1 + \frac{E_\theta}{E_r}(1 - 2\nu_{r\theta} + \frac{E_\theta}{G_{r\theta}}\right)^{\frac{1}{2}}$
- $g_1 = \frac{2}{\beta}(1 - c^\beta) + (1 + c^\beta)\ln(c)$
- θ = Polar coordinate
- ω = Angle defining direction of end load

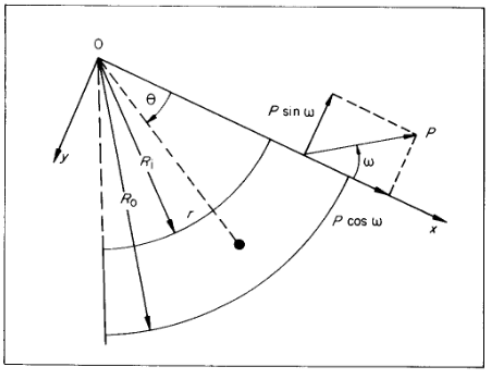

Figure 2.15: End load on a curved beam (Kedward et al., 1989)

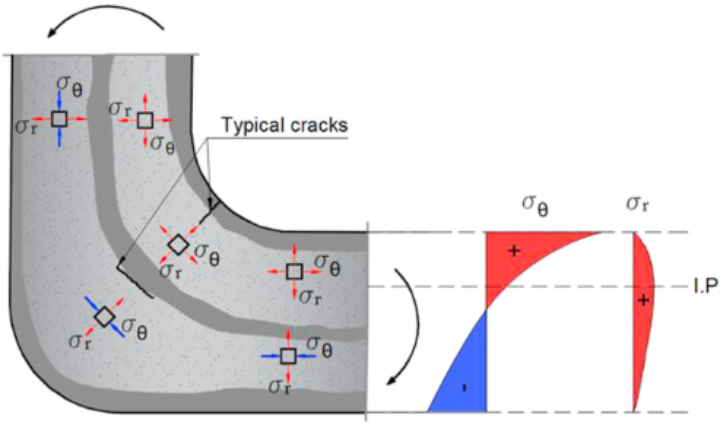

Figure 2.16: Tangential and radial stress distribution in a anisotropic homogeneous curved beam under pure bending, in 'open' bending mode (Cintra et al., 2021)

In order to use these equations to calculate the stress state in a WFJ subjected to bending (Cintra et al., 2021) superimposed the stress states of two L-junctions in order to obtain the stress state in a WFJ as seen in Figure 2.18. Expected is that the out-of-plane stresses will be most critical for a composite laminate.

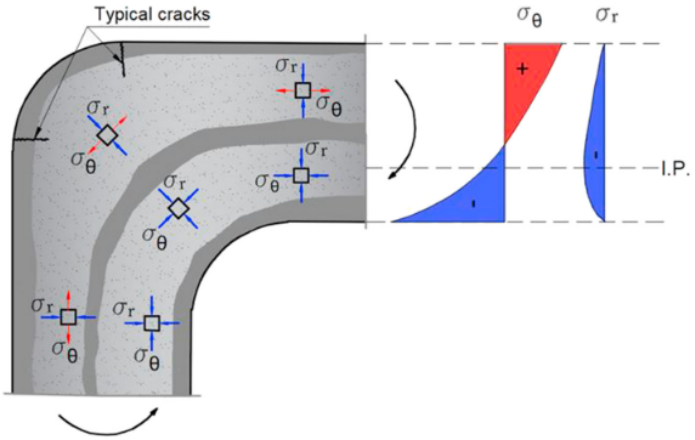

Figure 2.17: Tangential and radial stress distribution in a anisotropic homogeneous curved beam under pure bending, in 'closed' bending mode (Cintra et al., 2021)

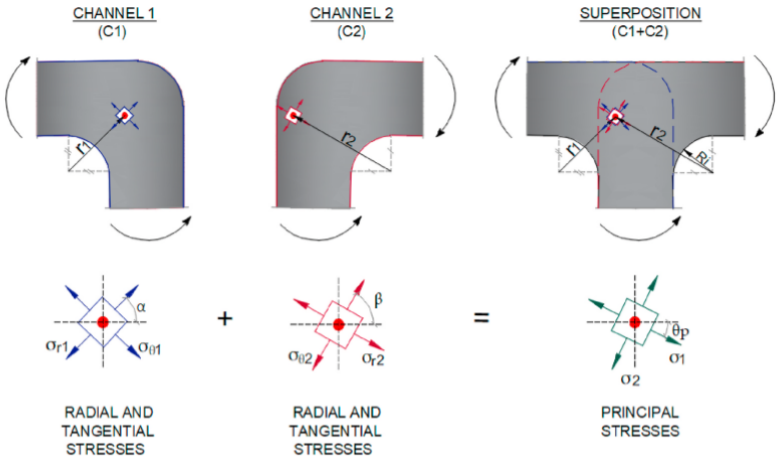

Figure 2.18: Superposition of stresses in L-Junction (Cintra et al., 2021)

2.8.2. IMPORTANT PARAMETERS IN A COMPOSITE CURVED BEAM SUBJECTED TO BENDING

The equations given by (Lekhnitskii et al., 1968) give insight into the important parameters effecting the response of a WFJ subjected to bending. (Cintra et al., 2021) used these equations to better understand the damage process and to obtain an order of magnitude of stresses at cracking in GFRP pultruded WFJs subjected to bending. In their research the radial (σ_r) and tangential (σ_θ) stresses were calculated at the radial (r) location of the crack onset of WFJ specimens using these equations. The parameters of the specimens needed for these calculation are:

- R_i; the internal radius.
- R_o; the external radius.
- E_θ; the tangential stiffness modulus.
- E_r; the radial stiffness modulus.

In the research conducted by (Cintra et al., 2021) the outer radius was assumed to be the inner radius plus the specimens' thickness ($R_o = R_i + t$) as a simplification. The radial modulus E_r was assumed to be 95% of E_θ, based on the average ratio of theoretical moduli resulting from a rule of mixtures approach. As the value k in these equations is a ratio between the E_θ and E_r, this constant will always equal $k = (\frac{1}{0.95})^{\frac{1}{2}} = 1.026$ as a result of this assumption regardless of the E_θ found for each specimen. These assumptions result in the following parameters needed to calculate the radial (σ_r) and tangential (σ_θ) stresses at the location of the crack:

- R_i; the internal radius.
- t; web thickness.

In conclusion, this indicates that only these two parameters are necessary to determine the failure response of the WFJ, provided the dominant failure mode corresponds to one of the four failure modes shown in Figure 2.19.

2.8.3. FAILURE MODES OF WFJ

Based on the analytical equations provided in section 2.8.1, the most likely failure modes in a WFJ subjected to bending are illustrated in Figure 2.19. Cracks are most likely to occur at four specific locations due to peaks in either out-of-plane or in-plane stresses.

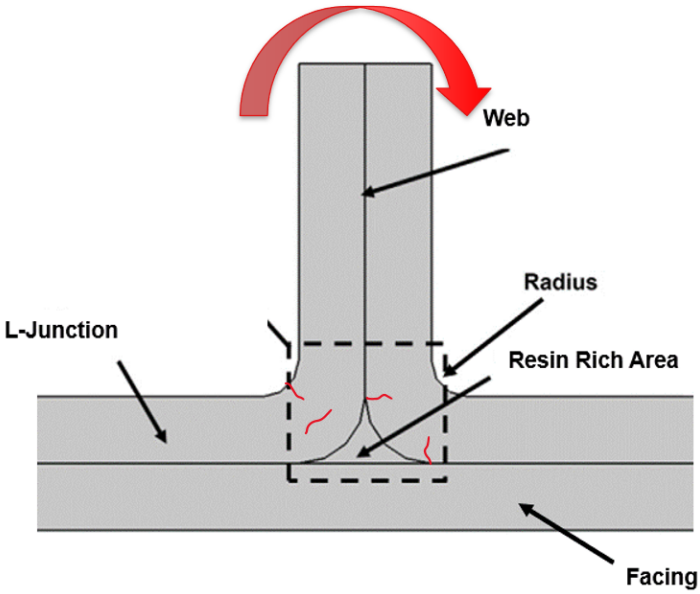

Figure 2.19: Typical cracks in WFJ subjected to bending (in red)

2.9. DESIGN CODES

2.9.1. FATIGUE LIFE VALIDATION OF STEEL JUNCTIONS

In the '*EN 1993-1-9:2005, Eurocode 3: Design of steel structures - Part 1-9: Fatigue*' (CEN, 2005), 'detail categories' are given for the fatigue verification of certain steel construction details. The number given to a particular detail for a given direction of stress fluctuation indicates which fatigue strength curve to use for the fatigue life assessment. The detail category number indicates the reference fatigue strength in N/mm^2 (CEN, 2005), see Figure 2.20. These detail categories were made by obtaining empirical data on fatigue tests on these steel details. These same detail categories do not yet exist but could also be constructed for composite details, however because composite is a anisotropic material the direction in which the direct stress range $\Delta\sigma_R$ is working on the composite material is important and must be taken into account for composite detail categories.

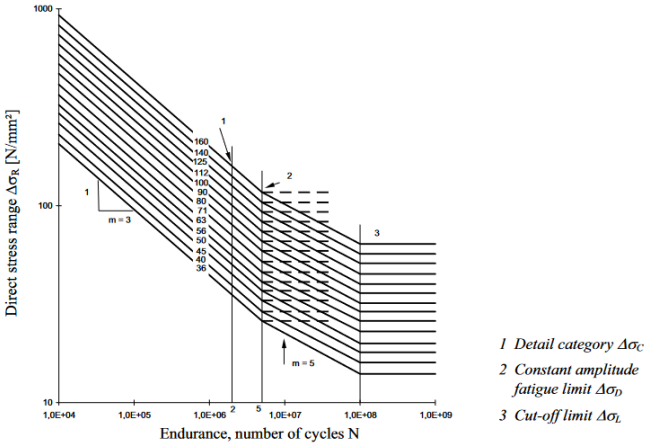

Figure 2.20: S-N curve for different detail categories (CEN, 2005)

2.9.2. FRP DESIGN CODES

Because FRP is a relatively new construction material in Civil Engineering there is a lack of knowledge. Currently there is no Eurocode for FRPs but there is a widely accepted Technical Specification (European Committee for Standardization, 2022). The state of the art is that there are currently a few recommendations for design codes of FRP bridges:

- *Prospect for new guidance in the design of FRP* (Ascione et al., 2016)
- *Fibre-reinforced Polymer Bridges – Guidance for Designers* (Mottram and Henderson, 2018)
- "TS19101: Design of fibre-polymer composite structures" (European Committee for Standardization, 2022)

- *Aanbeveling 96:2019 Vezelversterkte kunststoffen in bouwkundige en civiel-technische draagconstructies* (CROW-CUR, 2019)
- *CD 368: Design of Fibre Reinforced Polymer Bridges and Highway Structures* (Standards for Highways England, 2020)
- *Guide Specifications for Design of FRP Pedestrian Bridges* (American Association of State Highway and Transportation Officials, 2008)

However, these are still incomplete. Currently a Technical Specification (European Committee for Standardization, 2022) exists which can be used in parallel with national guidelines at the European level in the future. Eventually, this specification will be converted into a Eurocode (Onderzoeksgroep Schoonmeersen, 2020b). In the ""“TS19101: Design of fibre-polymer composite structures”"", fatigue verification is included. However, it does not rely on predictive methods; instead, it requires verification through testing. This approach ensures that the fatigue performance of fibre-polymer composite structures is based on empirical data rather than theoretical predictions.

The aim is, that once a Eurocode exists for FRP structures that is on par with the Eurocodes for other structural materials such as Steel and Concrete this will make designing civil structures with FRP become more accessible and reliable. In this case the material could be considered a worthy alternative to more traditional building materials such as steel and reinforced concrete (van IJselmuijden and Tromp, 2013).

There is a knowledge gap. This research provides more insight in the fatigue behaviour of complex FRP components by:

- Experimental Testing: Performing experimental tests to derive an S-N curve for a composite WFJ.
- Develop or adapt existing fatigue failure theories to predict the failure of such WFJs.
- Identifying fatigue failure mechanisms of the WFJ on which future design codes can base their verification methods on.

STATE OF ART: FRP FATIGUE DESIGN

It is known that the in-plane fatigue life of FRP composites is generally more favourable compared to steel (Vassilopoulos and Keller, 2011). In the white paper "*Ontwerpmethodes en softwarematige analysetechnieken / Design Methods and Software Analysis Techniques*" (Onderzoeksgroep Schoonmeersen, 2020a) the S-N curves of a few category details of steel are compared to the S-N curves of FRP consisting of E-glass UD plies and a polyester matrix with a 45% fiber volume fraction, as seen in Figure 2.21. It can be seen in this Figure that the fatigue performance of FRPs is superior to steel after 10^7 cycles, which is an important area for bridge design. However it is important to note that the fatigue performance of FRP when loaded 90 degrees, or out-of-plane, in relation to the fibre direction is usually much lower. The relevance of comparison with steel details is

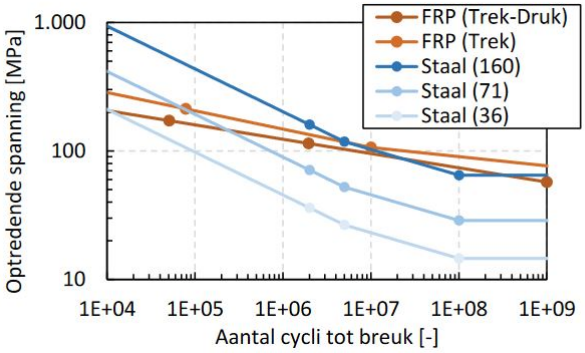

Figure 2.21: Comparison of Steel and FRP S-N curves (Onderzoeksgroep Schoonmeersen, 2020a)

therefore limited.

Continuing with the afore mentioned recommendations for design codes the design recommendations/equations specifically for the fatigue performance of FRPs will be discussed from a few of these recommendations in the following paragraphs.

Prospect for new guidance in the design of FRP (JRC REPORT) & *Aanbeveling 96:2019 Vezelversterkte kunststoffen in bouwkundige en civiel-technische draagconstructies* (CUR96)
Beginning with the JRC report and CUR96 these will be discussed together because their recommendations for fatigue design of FRP are very similar. They both provide an equation that describes a so called "S-N curve", Eqn. 2.9, to determine the fatigue life of a component subjected to a Constant Amplitude (CA) load, which is defined as such in the case that the maximum and minimum values of the load amplitude does not exceed 10% of the permanent load.

$$\log(N) = k \cdot \log\left(\frac{\gamma_M \cdot \sigma_{max}}{\eta_c \cdot B}\right) \tag{2.9}$$

Where:

- N is the number of cycles to failure:
- k is a regression parameter, to be determined from tests;
- σ_{max} is the maximum cyclic stress occurring;
- B is the characteristic failure stress of the laminate at 1 cycle;
- γ_M is the material factor for fatigue;
- η_c is the conversion factor for fatigue.

The evaluation of fatigue with a Variable Amplitude (VA) load should be based on Miner's linear damage rule, Eqn. 2.10

$$D = \sum_{i}^{M} \frac{n_i}{N_i} \leq 1 \tag{2.10}$$

Where:

- n_i is the number of cycles occurring in a load of a specific size and R value;
- N_i is the number of cycles to failure for a specific size and R value;
- M is the number of loads with a specific size and R value.

The JRC report refers to an annex to that describes how to derive an S-N diagram from test results.

The JRC says this about finding the S-N curve from components:

"If the local details are uncertain (e.g. if the fibre mat is of variable waviness), then confident prediction of local fatigue life can be difficult. In such cases, the designer might consider proof testing of the component (such as the cellular deck including the fatigue-critical joints of complex geometry) in fatigue, to produce S-N curves for the component. In order to maximize the integrity of the results from such tests, care should be taken to reproduce the actual local contact load distribution on the component as far as possible." (Ascione et al., 2016)

The CUR96 provides a table and a S-N curve for FRP laminates for specific properties, but for more complex geometries and stress states in multiple directions it also prescribes to derive the S-N curves from tests.

The testing procedure prescribed by both reports is to perform at least three fatigue tests at three different load amplitudes and these test must range from $1 \cdot 10^3$ cycles to at least $5 \cdot 10^5$ cycles. The test geometry should be similar to the one seen in Figure 2.22.

This testing procedure, known as a 'coupon test' is to derive the S-N curves for FRP laminates loaded in-plane with non-complex geometries. For components such as a WFJs, no standard procedures are described.

CD 368: Design of Fibre Reinforced Polymer Bridges and Highway Structures (CD368)
The CD368 (which replaces the BD 90/05) does not provide any equations or S-N curves for the fatigue design verification of FRP bridges. It states that fatigue limit state verification should be based on the S-N line of the same material and of the fatigue load type under consideration, expressed as an R value for CA loading. For VA loading the evaluations should be done based on Miner's linear damage rule eq:2.10. The S-N curve must come from previous testing when available otherwise new tests should be done.

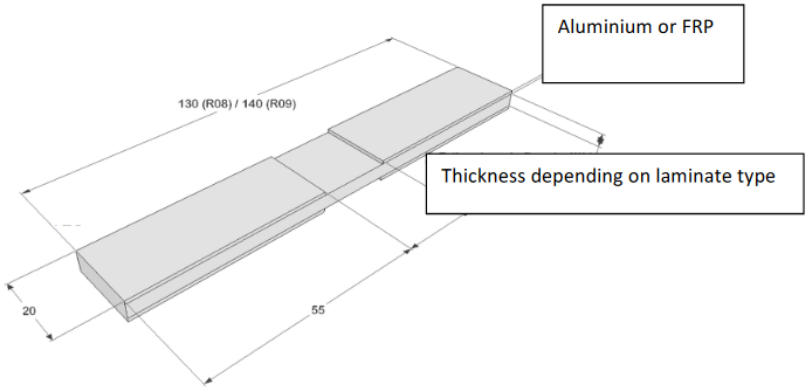

Figure 2.22: Fatigue test geometry (Ascione et al., 2016)

The CD368 does however provide more information on the tests that must be performed and the manner of which therein, see Figure 2.23.

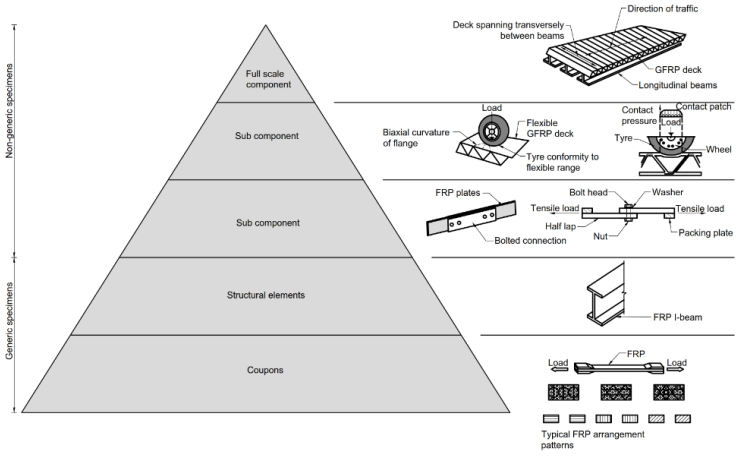

Figure 2.23: Rouchon pyramid of composites materials certification (Standards for Highways England, 2020)

A summary of the the description of a fatigue test of an FRP bridge deck prescribed by the CD368 is as follows:

- A single wheel load test according to the paper (Sebastian et al., 2017), seen in Figure 2.24;
- The test load shall be applied by a steel loading plate 200 mm x 200 mm square and at least 30 mm thick, faced with a 12 mm thick cork pad;

- the result of a fatigue test shall be deemed a 'pass' if 10^7 cycles are completed without detectable cracking or failure.

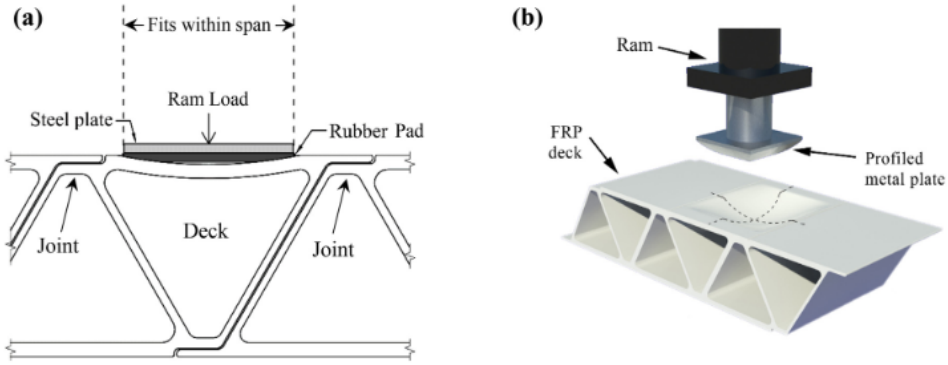

Figure 2.24: Single wheel load test (Sebastian et al., 2017)

This load configuration should be used in future research when the fatigue behaviour of the WFJs found in this research is verified in the context of a large scale deck component. Due to the small scale of the WFJ component tested in this research, the issue of load introduction is not part of the scope of the test.

2.10. SUMMARY

This chapter reviews the current knowledge on materials production and failure mechanisms, with a focus on the Web-to-Flange Junction (WFJ) in Glass Fibre Reinforced Polymer (GFRP) Web-Core Sandwich Panel bridge decks.

Fatigue failure mechanisms in GFRP composites are varied and can occur simultaneously, interacting in ways that make fatigue life prediction complex. Previous research indicates that fibre waviness, particularly pronounced in WFJs, can cause stress concentrations that lead to premature failure. This suggests that waviness is a critical parameter influencing the response of the WFJ.

Analytical equations are given by Lekhnitskii (Lekhnitskii et al., 1968) to determine the in-plane and out-of-plane stresses in a composite beam subjected to bending can be used to predict the likely failure modes of the WFJ. Given that the weakest direction of any GFRP composite is the out-of-plane direction and that these stresses occur in curved beams, these stresses are likely to cause mode 1 delamination in a WFJ subjected to bending. These equations highlight the importance of web thickness and radius in predicting this response.

Currently, existing design codes do not include equations to validate the static and fatigue safety of WFJs. To address this gap, tests are necessary to determine if a dominant

failure mode can be identified for WFJs under bending. If the dominant failure mode aligns with the predictions made by Lekhnitskii's analytical equations (Lekhnitskii et al., 1968), these equations can be used to predict such failures. This would increase our understanding of the parameters influencing this response and improve the safety of GFRP Web-Core Sandwich Panel bridge decks.

3

METHODOLOGY

In this chapter the methodology used in this research is explained which is used to investigate the fatigue behaviour of the WFJ. To investigate the fatigue behaviour of the WFJ subjected to bending, static and fatigue tests were performed on WFJ specimens retrieved form a WCSP bridge deck provided by Fibercore Europe BV. This methodology is guided by the safe-life approach, which dictates that there is no damage tolerated during the service life of a component. Therefore the main focus of these tests are to find what damage occurs to the specimens and when this damage initiates. Additionally analytical methods are used to identify the most important parameters dictating the behaviour of the WFJ based on the observed failure modes from testing. Also Finite Element Analysis is used (elaborated on in chapter 5) to investigate weather the identified important parameters are sufficient to predict the response of the WFJ and to investigate the stresses developing in the WFJ after an initial crack has occurred.

3.1. SAFE-LIFE APPROACH

For the determining of the fatigue life of the WFJ the safe-life approach is chosen. This approach dictates that a component is deemed safe until any damage occurs in the component whether or not the component can still withstand loads or not.

This conservative approach aligns with the current method of verifying the fatigue life of junctions in newly constructed steel bridges using S-N curves. The S-N curve indicates how many cycles a component or material can sustain at a certain constant stress amplitude until damage occurs. Secondly because there is little precedent on the fatigue life of the GFRP WFJ it is wise to start this investigation with the most conservative approach, where future research could build on this research using a less conservative approach when more knowledge is obtained. Finally, another benefit of this approach is that it allows for a focus on the WFJ component without needing to consider its behaviour in a larger context, such as the Web-Core Sandwich Panel. In contrast, other approaches require determining the extent of damage that can be tolerated or how a

secondary load path can be established. Where this larger context is very 'case study' dependant making the results of such research less generic.

A downside to this approach is that it may be overly conservative, potentially preventing the material from being used to its fullest capacity and thereby increasing the costs of component design. This research aims to provide initial insights into whether the WFJ component can still resist loads even after sustaining initial damage.

3.2. WFJ SPECIMENS

3.2.1. WFJ SPECIMEN RETRIEVAL

The WFJ specimens are retrieved from a single WCSP provided by Fibercore Europe BV, with material properties given in Tables 3.1 and 3.2. See also appendix A for more material properties. First sections with a width of 80 mm were cut from WCSP sections, as seen in Figure 3.1. This width was chosen to minimise the effect of edge effects. Then the foam core is removed from these sections, as the foam has no structural purpose so it is removed to avoid interfering with the testing process. Finally the specimens are cut along the cutting lines show in Figure 3.2, to obtain the final WFJ component as seen in Figure 3.3. The dimensions of each WFJ specimen were measured with a caliper. The thickness of webs are measured at 3 locations, just after the junction, in the middle and at the end of the web and the average thickness of these three measurements is taken. The thickness of the deck is measured with a caliper at four locations, twice at both ends and once just before the junction and once just after the junction. Also here the average thickness of the four measurements is taken. The measurement of all the specimens are given in appendix B. As the radius is also determined to be an important parameter the radii of the WFJ specimens are measured using the GOM Correlate software by fitting a circle to the radius. The radius of the L-Junction is then determined to be the radius of the fitted circle, see Figure 3.4.

Table 3.1: Type op FRP

Fibres	Part	Production method
E-glass/UP High Vf, 1962 (kg/m^3)	Flange	Infusion
E-glass/UP Low Vf, 1576 (kg/m^3)	Web	Infusion

Table 3.2: Typical materials properties, Design values

Material	Tensile modulus (Long) (MPa)	Tensile strength (Long) (MPa)	Max strain (Long)	Poisson ratio
FRP (Flange)	42000	855	0,0201	0,27
FRP (Web)	22000	136	0,015	0,27

Figure 3.1: Specimen with a width of 80 mm

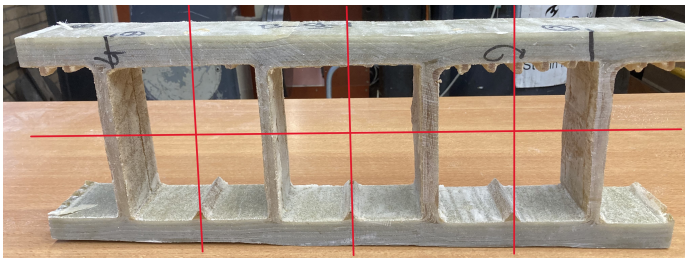

Figure 3.2: Specimen with foam removed and cutting lines indicated

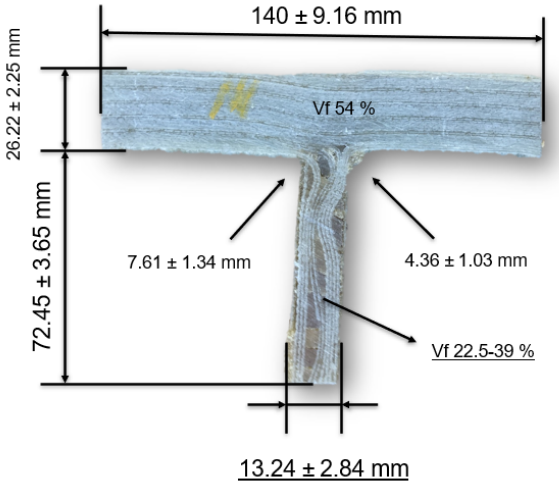

Figure 3.3: WFJ dimensions

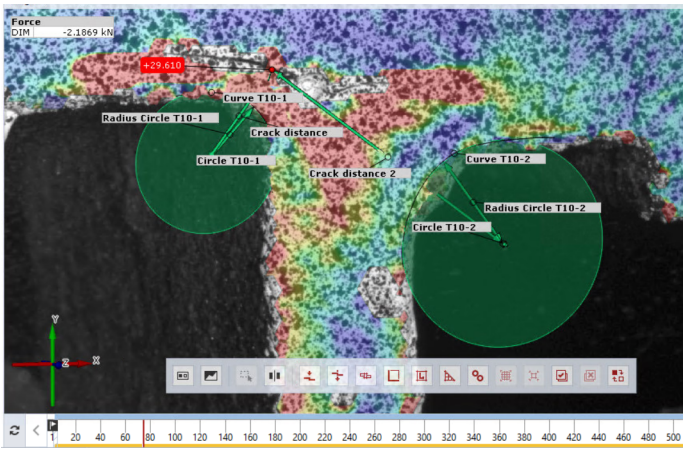

Figure 3.4: Measurement of radius in GOM Correlate

3.2.2. CATEGORISATION OF THE WFJ SPECIMENS

TOP AND BOTTOM SPECIMENS

The WFJ specimens were categorised labelled as Top (T) or Bottom (B) specimens. This distinction is important because the WCSP bridge decks are fabricated upside down, resulting in the bottom side (during fabrication) being smoother due to direct contact with the mould and having the whole weight of the bridge deck being pressed down on it. After fabrication this bottom side is then right side up, making the smoother side the top surface for easier application of additional layers, such as asphalt, and providing a better finish for the bridge deck users.

Z-LAYER

The web consists of layers from the wrap on each side and a Z-layer, as discussed in Chapter 2 section 2.2. This Z-layer comes from one side into the junction and therefore the deck thickness is slightly larger on this side, and it is assumed that the junction strength is also larger on this side because the T-junction can be seen as two L-junctions added together (Cintra et al., 2021) where the L-junction on one side consists of only the wrap layer and the L-junction on the other side consists of the wrap layer and the Z-layer. The side where this Z-layer enters the junction is denoted with a "Z" on all specimens. Since the side without the Z-layer is assumed to be weaker, all specimens are tested with the Z-layer on top. This is done so that the non Z-layer side is tested in the weaker 'open' bending mode.

WAVINESS OBSERVATIONS

It is observed that there is quite a large variation in web thickness between the WFJ specimens, as seen in Figure 3.3. Because all the specimens have the same number of plies (this was also verified visually by counting the plies, see Figures 3.5 and 3.6) a larger web thickness with the same amount of plies corresponds with a lower fibre volume fraction (V_f). This lower V_f is also observed to correspond with increased waviness of the plies. The (unimpregnated) fibre cloth becomes wrinkled, and during production, the foam blocks cannot be compressed further. Consequently, the void is filled with resin during infusion. This increase in waviness is likely to have an effect on the strength of the WFJ because, as discussed in section 2.6 of chapter 2, fibre waviness is may induce stress concentrations causing premature failure of the component. To account for this waviness factor an imperfection rating is given to the WFJ specimens based on visual inspection.

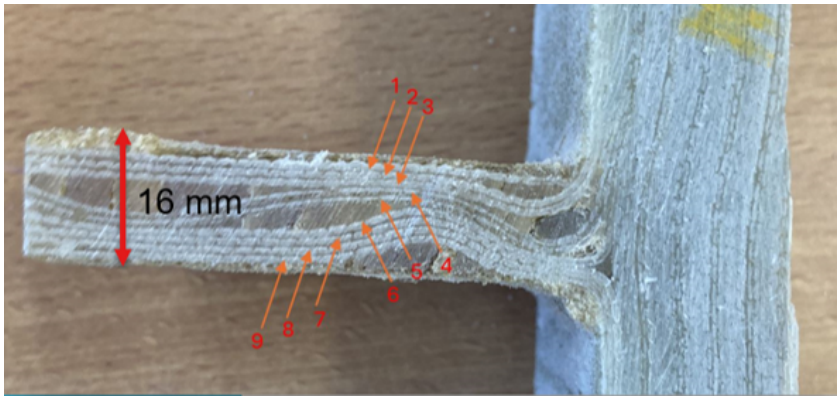

Figure 3.5: Plies Web B1 Specimen (9-double plies indicated)

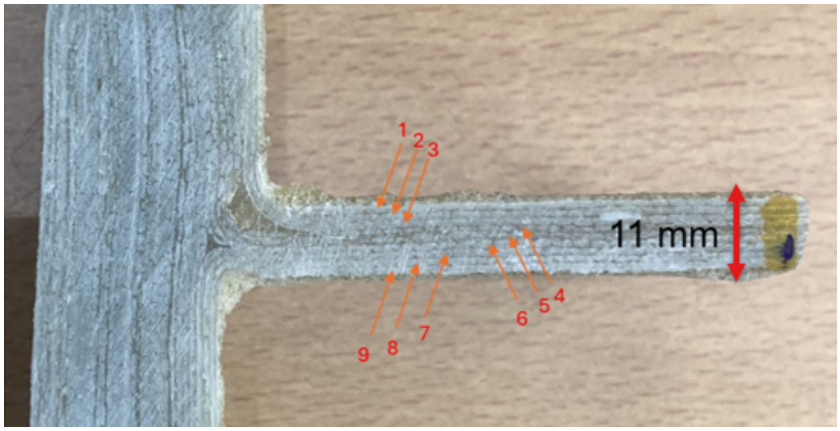

Figure 3.6: Plies Web B1 Specimen (9-double plies indicated)

3.2.3. IMPERFECTION RATING

The WFJs are categorised according to an imperfection rating based on a visual inspection of the junctions. The imperfection rating scale ranged from 1 to 3, where 1 indicates significant imperfections, and 3 indicates minimal imperfections. And example of specimens with imperfection rating of 1,2 and 3 can be seen in Figure 3.7. When assessing imperfections, the 'waviness' of the plies is evaluated. This waviness occurs when the plies are not aligned parallel to the outer geometry of the WFJ. It is observed that waviness of the plies led to gaps in the component, which are subsequently filled by resin. As a consequence, the component is thicker and the fibre volume fraction (V_f) lower.

Figure 3.7: examples of specimens with imperfection ratings of 1, 2 and 3

1. Significant imperfections
2. Moderate imperfections
3. Minimal imperfections

Because there is a direct relationship between the web thickness and fibre waviness in the specimens, the web thickness is plotted against the imperfection rating in the graph seen in Figure 3.8. This graph shows that the specimens with the lowest amount of waviness (imperfection rating 3) tend to have a smaller web thickness and the opposite appears to be true for the specimens with a high amount of waviness (imperfection rating 1). However, this is not always the case, especially with specimens that have 'moderate imperfections'. Imperfections can occur before the web, decreasing the imperfection score but having little effect on the web thickness, as seen in specimen T12 in Figure 3.9, which has an imperfection rating of 2.

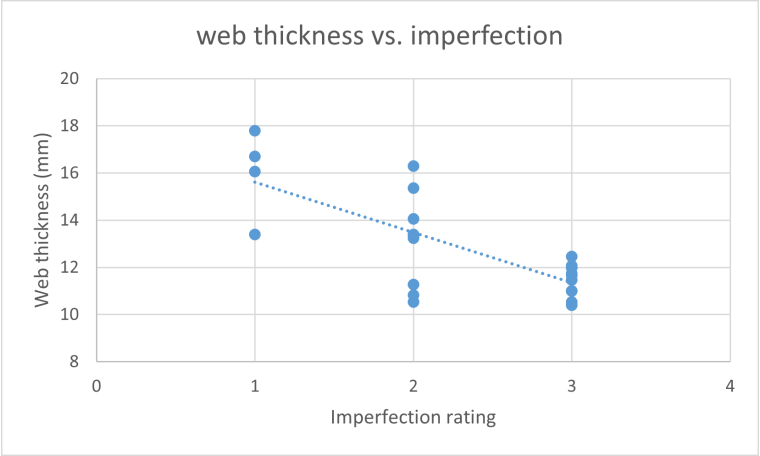

Figure 3.8: web thickness - imperfection rating plot

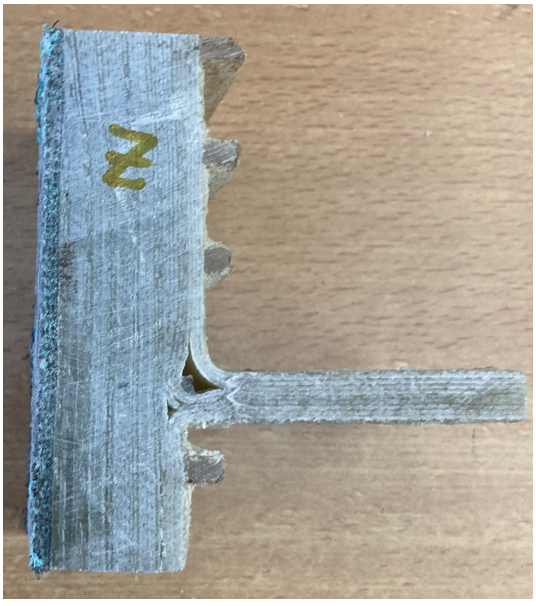

Figure 3.9: Specimen T12, with imperfection rating 2 and a web thickness of 10.53 mm

3.3. TEST SET-UP CONFIGURATION

3.3.1. TEST SET-UP DESIGN

The test-setup consists of two WFJs glued together in a three-point bending test setup, as seen in Figure 3.10. This creates a statically determined system, that when loaded at the top of the flanges, introduces bending at the WFJs of both specimens simultaneously. This test-setup allows for testing of the non-standard geometry of the WFJ in a commonly used test-setup format; the three-point bending test, where two junctions are tested simultaneously.

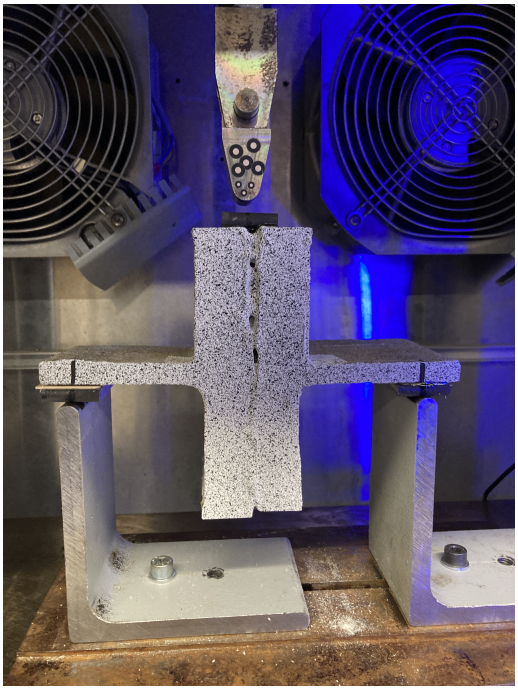

Figure 3.10: Test-Setup in testing machine

3.3.2. SPECIMEN PREPARATION

To create this test-setup the two WFJs are glued together at the flanges using structural adhesive quick-set epoxy. When necessary, clamps are used to attach two WFJs when surface coatings impended proper adhesion. Specimens are combined base on having the same Top (T) and Bottom (B) denomination, the same imperfection rating, and having a comparable web thickness. This is done to combine WFJ specimens with similar geometries, hypothesised to have a similar response.

Steel tabs ($25x6x80mm^3$) are glued at the ends of the webs to ensure vertical alignment and facilitate force transmission during testing. To measure strains and the ro-

tation angle of each WFJ during testing, a thin layer of white non-reflective paint was applied to one side of the specimens, followed by a random black speckle pattern using a spray gun. This preparation enables the Digital Image Correlation (DIC) system to capture strain data, see section 3.3.5.

3.3.3. TESTING MACHINE

The Universal Testing Machine (UTM-25) with a maximum capacity of 15kN was calibrated and used for applying vertical loads to the flanges of the specimens from the top. The calibration report is provided in Appendix C of the report.

3.3.4. TESTING PROCEDURE

STATIC TEST PROCEDURE

The static tests are performed in order to determine the mean static strength for the fatigue tests, to determine the dominant failure mode and to determine the rotational stiffness of the WFJ. The mean strength is chosen to approximate the actual strength of the component and material. The characteristic strength can be calculated afterwards for design purposes. Additional static tests are performed on WFJs with fatigue damage in order to measure the rotational stiffness degradation due to fatigue damage. Static tests are conducted by applying a displacement of 1 mm per minute. The maximum force was estimated to be between 2.4 to 6.4 kN.

FATIGUE TEST PROCEDURE

The fatigue tests aim to identify the number of cycles until crack initiation, construct the S-N curve of the WFJ, and determine its fatigue life. Additionally, these tests help identify the dominant fatigue failure mode, crack propagation, and stiffness degradation.

The load ratios used to determine the fatigue performance of a component and to construct a Constant Life Diagram (CLD) are as follows (CROW-CUR, 2019):

- $R = -0.1$; for altering tensile and compressive loads;
- $R = 0.1$; for altering tensile loads only;
- $R = 10$; for altering compressive loads only;

Where the R ratio is the ratio between the maximum and minimum load.

$$R = \frac{\sigma_{min}}{\sigma_{max}} \tag{3.1}$$

The most critical stresses for the WFJ are expected to be out-of-plane (OOP) tensile stresses discussed in section 2.8 of chapter 2. Research by (Cintra et al., 2021) found that the WFJs tested in 'open' bending mode, thus subjected to tensile stresses, had the least amount of moment resistance. Therefore, the fatigue tests are performed in a load control mode with a stress ratio of $R = \frac{\sigma_{min}}{\sigma_{max}} = 0.1$. This situation occurs when the deck is loaded by movable traffic loads causing the WFJ to bend in one direction.

The cyclic loading pattern was a sinusoidal wave at a frequency of 4 Hz for higher load levels and up to 12 Hz for lower load levels. The thermal effect, measured with an E96 FLIR Advanced Thermal Imaging Camera, was deemed insignificant, with temperatures remaining below a 4°C increase compared to the ambient room temperature. This increase was primarily caused by the lights needed for the DIC system heating the specimen.

Fatigue load levels are chosen based on the mean moment resistance strength of samples obtained from static tensile tests. The fatigue tests are performed at 70%, 60%, 50%, 40%, 30% and 20% of the mean static strength found from the static strength tests with two WFJs per load level.

3.3.5. DATA COLLECTION

FORCE-DISPLACEMENT DATA

During the testing, the force and displacement are recorded by the UTM-25 testing machine. This data is needed to determine the force resistance of the WFJs, which is half the force applied by the machine for each WFJ in this statically determined system. Additionally strains and rotations of the WFJs are captured using the Digital Image Correlation (DIC) system. By using the GOM Correlate software, the photographs taken by the DIC system and the speckled pattern on the specimens can be analysed to determine the strains and displacements of the specimens.

STRAIN DATA

The DIC system is used to identify the locations of the highest strain and to locate where crack initiation occurs, see Figure 3.11. A virtual extensometer (10 (mm)) is used to measure the strain at failure using the GOM Correlate software. The extensometer is placed perpendicular to the failure crack, see Figure 3.12. This 'failure strain' is used to determine crack initiation during the fatigue tests.

To determine the tensile stresses the junction are subjected to during the fatigue, tests the nominal stress is calculated using the strain data. This is the maximum tensile stress in the web before the radius as result of the bending moment load. To determine the nominal stress, a curve along the height of the web is made in the GOM Correlate software to read the strain along the height of the web, see Figure 3.13. Using the E modulus calculated from composite laminate theory and the relationship $\sigma = E\epsilon$, the nominal stress is determined.

ROTATIONAL ANGLE DATA

Also measurements of the rotations of each WFJ individually is captured by the DIC system, as seen in Figure 3.14. This is done by analysing the captured images using the GOM Correlate software. In this software two lines are constructed: one line passing through and parallel to the web and anther passing through and parallel to the flange. The software measures the relative angles between these lines to capture the rotation of

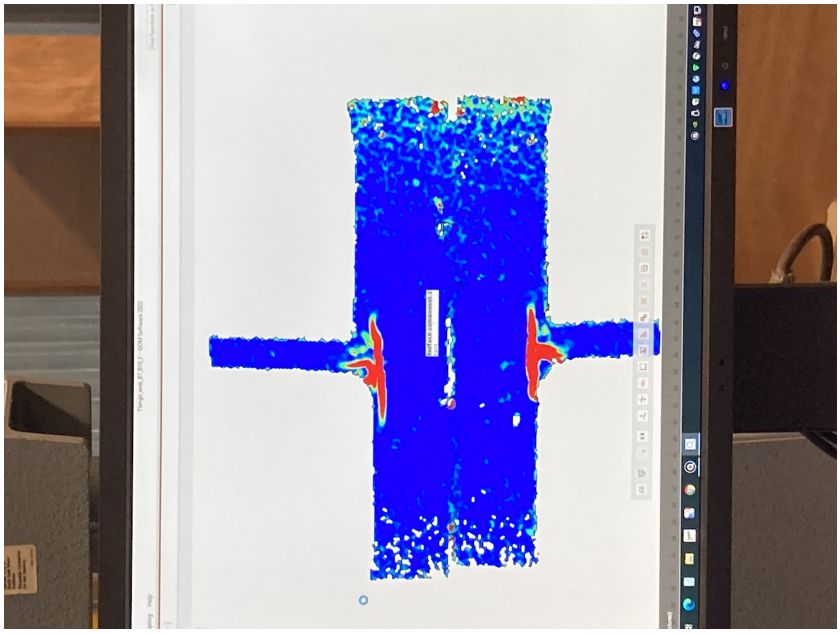

Figure 3.11: B7-B10 DIC data

the junction under loading. In combination with the applied bending load this data is used to calculate the rotational stiffness of the WFJ. This data collection allows to capture the force-displacement, rotational stiffness and failure mode of the WFJ during testing.

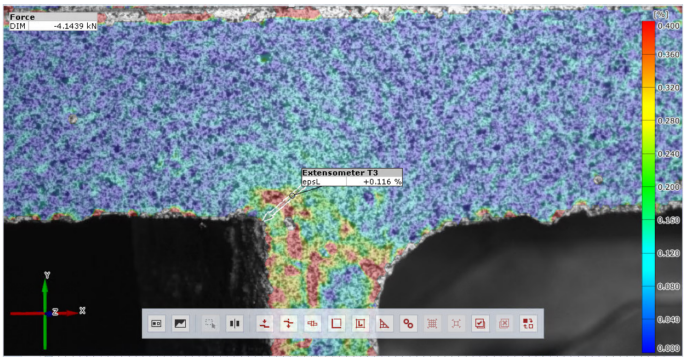

Figure 3.12: extensometer GOM software, specimen T3

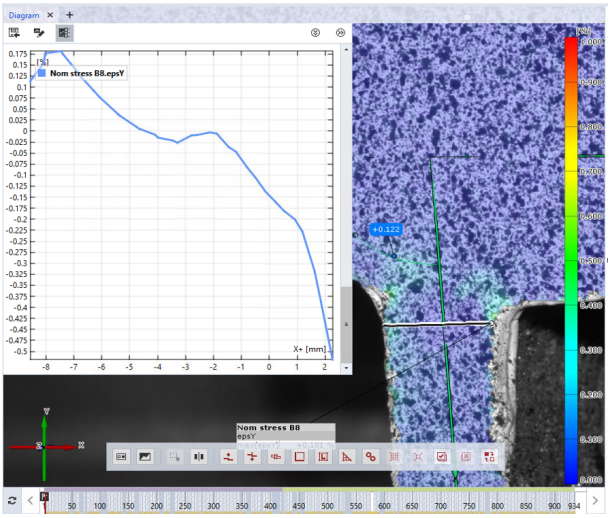

Figure 3.13: nominal strain, specimen B8

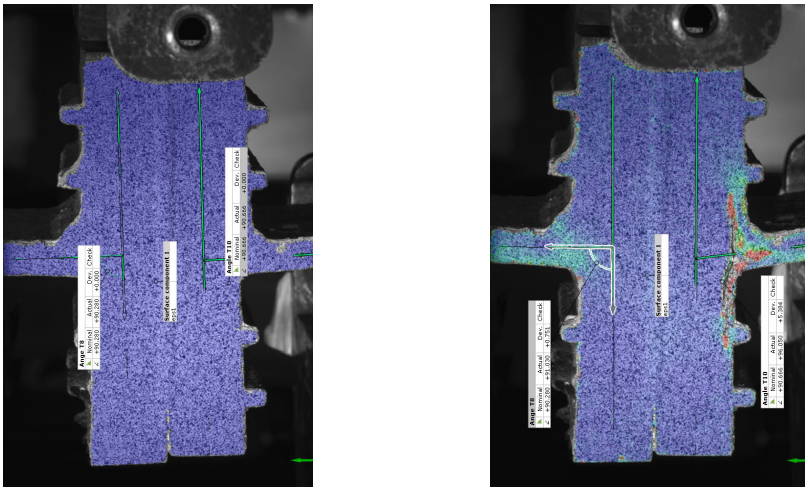

(a) undeformed shape

(b) deformed shape

Figure 3.14: Angle of rotation measurement through GOM software

3.4. SUMMARY

In this chapter, the methodology used to investigate the fatigue behaviour of the WFJ subjected to bending is given. The methodology follows the safe-life approach, which dictates that no damage is tolerated during the service life of the component. This approach is chosen for its conservative nature, aligning with current practices for steel bridge junctions and allowing the focus to remain on the WFJ component. To investigate the WFJ response according to this approach, static and fatigue tests are performed on WFJ specimens retrieved from a WCSP provided by Fibercore Europe BV. Static tests determined the static strength, failure mode, and rotational stiffness, which informed the subsequent fatigue tests aimed at identifying fatigue strength and failure modes, and constructing an S-N curve. Additionally, analytical methods are used to identify the critical parameters influencing WFJ behaviour, and Finite Element Analysis (FEA) is employed (which is given in chapter 5) to validate these parameters and investigate stress distributions post-crack initiation. The chapter detailed the specimen preparation, test setup configuration, including the use of a Universal Testing Machine (UTM-25) and a Digital Image Correlation (DIC) system, and the procedures for static and fatigue testing. Data collection focused on capturing force, displacement, strain, and rotational data in order to understand the mechanical response and failure mechanisms of the WFJs.

4

TEST RESULTS

The chapter presents the findings from the experimental tests conducted to assess the static and fatigue response the WFJ. The primary objective of these tests is to determine the static strength, failure modes, and rotational stiffness of the WFJs, as well as to evaluate their fatigue strength, identify fatigue failure modes, and construct an S-N curve. The chapter details the results from both static and cyclic tests, offering insights into the mechanical behaviour of the WFJs subjected to bending. Additionally, it explores the impact of critical parameters, such as web thickness, radii and waviness, on the performance and durability of the junctions. By analysing the experimental data, this chapter answers the sub-questions 1 and 2:

1. What is the static and fatigue response of the WFJ subjected to bending?
2. What are the most important parameters determining this behaviour?

4.1. STATIC TEST RESULTS

4.1.1. STATIC STRENGTH

To determine the static strength of the WFJ, five static tests are performed. The results of these tests are summarised in Table 4.1 and illustrated in Figure 4.1. In the table the moment resistance (M_r) at the failure moment is given per mm width of the specimens. Also the radial location of the crack is given (r_{crack}) and a that location the OOP stress is calculated (σ_r) using the equations given in section 2.8.1 of chapter 2. The OOP stress calculations can be found in appendix D.

The failure moment corresponds to the point on the force-displacement curve where the material or structure reaches its maximum load just before failure. This is determined from the force-displacement graph, specifically at the moment when the force increases linearly until it reaches a maximum and ceases to increase further. In all cases, one side of the WFJ failed before the other, providing the static strength resistance for one WFJ per test.

Table 4.1: Static test results WFJ

WFJ	Imperfection rating 1=bad, 3=good	Web Thickness (mm)	M_r/width (kN*mm/mm)	r_{crack} (mm)	σ_r (MPa)
T10	3	11.67	1.667	8.15	28.48
T5	1	13.4	2.053	6.57	30.08
T3	2	15.4	1.632	5.37	21.32
B2	1	16.7	1.283	12.05	7.23
T4	3	11.0	1.358	7.48	20.56
mean		13.6	1.599		19.32
StDv		2.4	0.30		9.73
CoV,%		17.7	19.0		50.4
char,val			0.89		

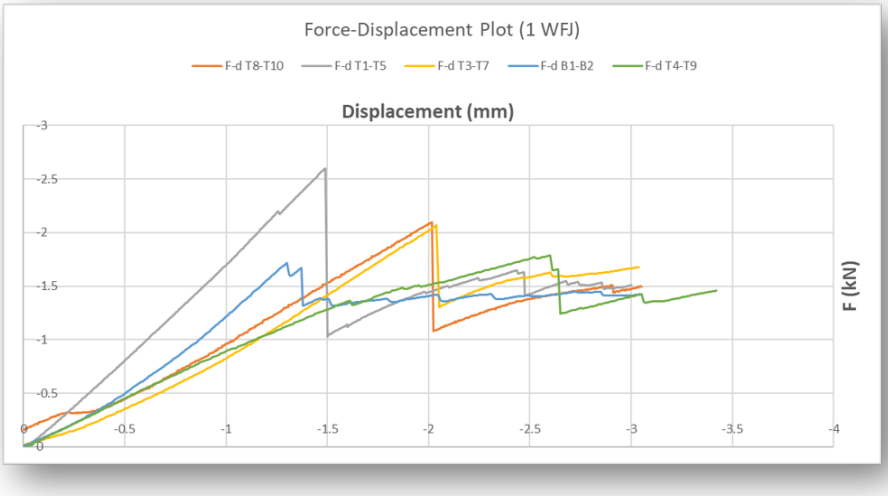

Figure 4.1: Force-Displacement plots static test results

RESULTS OVERVIEW

- Mean Static Strength: The mean static strength obtained from the tests was calculated to be 1.599 kNmm/mm.
- Coefficient of Variation: The variability in the static strength results, indicated by the coefficient of variation, was found to be 19.0%. This high variation suggests inherent uncertainties in determining both static and fatigue strengths of the WFJ.
- Characteristic Value: Using the coefficient of variation and the mean value, the characteristic value of the static strength was determined to be 0.89 kNmm/mm. This calculation follows the design standard ("NEN-EN 1990:2002+A1:2019 Eurocode - Grondslagen van het constructief ontwerp", 2002) which requires a minimum of three static tests to determine the characteristic value of a component's static resistance.

OBSERVATIONS

The significant variation in the static strength results is attributed to differences in specimen properties such as web thickness, radius and waviness of the plies. These factors contribute to deviations in response, with the web thickness playing a crucial role as it directly influences the section modulus. Additional analysis on how these 'important parameters' influenced the test results is given in section 4.3.

4.1.2. FAILURE MODE

From the static tests conducted on the WFJ specimens, a consistent failure pattern was observed. During these tests, only one of the two junctions failed each time. The primary failure mode identified was a delamination crack initiating in the radius of the junction in an 'open' bending mode and propagating through the flange. This crack appeared as a straight line running parallel to the flange. Interestingly, no cracks are observed in the web itself, which could have been expected due to shear stresses induced by bending. Notably, the crack consistently originated at the interface between the 'Wrap-layer' and the 'UD-layer' of the laminate layup. This failure mode was more clearly seen on the non-patterned side of the specimens, where the crack propagation was evident along this interface, see Figure 4.2. The Digital Image Correlation (DIC) data reveals two regions of high strain moments before crack initiation: one within the flange running parallel to it and another following the curvature of the junction, overlapping both the flange and the web. These strain regions align with the typical cracks predicted by radial stresses in a curved beam loaded in an 'open' mode. The observed cracks and their locations underscore the critical role of the interface between laminate layers and OOP tensile stresses in the failure of WFJs under static loading conditions.

FAILURE STRAIN

Using a virtual extensometer ($10mm$) in the GOM Correlate software the strain at the crack location before failure is measured, as explained in section 3.3.5 of chapter 3. These recorded strains are given in the graph in Figure 4.3 and a mean failure strain of 0.122% was recorded and is used to determine crack initiation during the fatigue tests.

Figure 4.2: Static tests failure modes

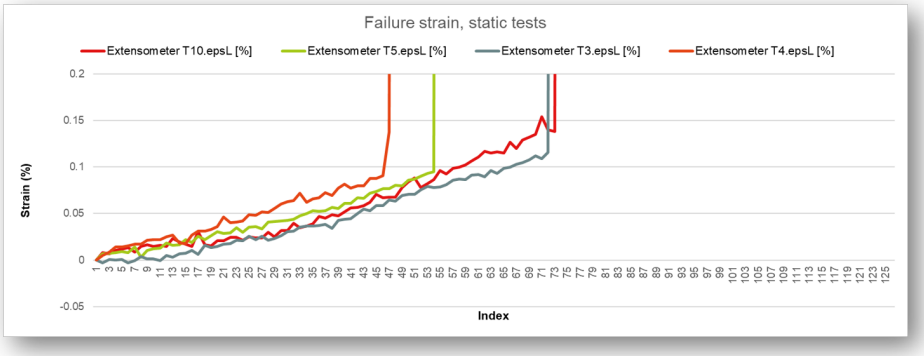

Figure 4.3: Strains at crack location

4.1.3. ROTATIONAL STIFFNESS

The rotational stiffness of the WFJ is determined using data collected from the static tests, see the graph in Figure 4.4. The angle of rotation during the testing is obtained from the Digital Image Correlation (DIC) system, which allowed for the measurement of the relative rotations between the web and flange. This method negates the influence of flexural effects on the web. The results indicates significant variability in the rotational stiffness values among the different WFJ specimens, correlating closely with their failure strengths.

The rotational stiffness data shows significant variation, influenced by factors such as web thickness, radius, and the presence of imperfections. This variability aligns with the differences observed in static strength, underscoring the importance of these parameters in determining the mechanical performance of WFJs.

Junction T5, shown in Figure 4.5, exhibited the highest rotational stiffness. It has a web thickness of 13.4 mm, which is close to the mean web thickness of 13.24 mm, a radius of 3.84 mm, which is lower than the mean radius of 4.36 mm, and an imperfection rating of 1 due to fiber waviness and large resin-rich areas on the Z-side.

In contrast, Junction T3, shown in Figure 4.6, exhibited one of the lowest rotational stiffness values. This junction has a web thickness of 15.37 mm, which is higher than the mean web thickness of 13.24 mm, a radius of 2.89 mm, which is lower than the mean radius of 4.36 mm, and an imperfection rating of 2 due to fibre waviness.

Basic mechanics suggest that an increase in web thickness and an increase in the stiffness of the FRP material (a higher V_f) will result in higher rotational stiffness of the WFJ. The analysis of these two junctions suggests that achieving a balance between these parameters results in a WFJ with high rotational stiffness, as shown by Junction T5, which was measured to have the highest rotational stiffness despite having only an average web thickness. In the specimens used for this research, those with a larger web thickness have the lowest V_f, and the specimens with the highest V_f have the smallest web thickness (explained in section 3.2.2 of chapter 3). More testing is needed where one of these two variables is kept constant to draw more definitive conclusions.

Regarding fibre waviness and imperfection rating, Junction T5 shows that a large amount of fibre waviness and resin-rich areas may be present, yet the rotational stiffness of the specimen can remain high. In this specimen, the imperfections are mostly located on the Z-side of the junction, whereas the non-Z side is tested and ultimately fails. This suggests that the location of the imperfections within the junction could be more important than initially recognised, indicating a need for a more robust approach to measuring and identifying these imperfections.

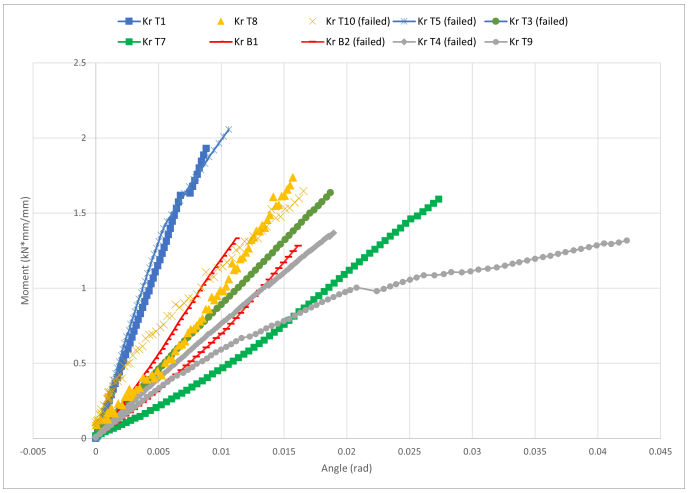

Figure 4.4: Rotational stiffness (Kr) static tests

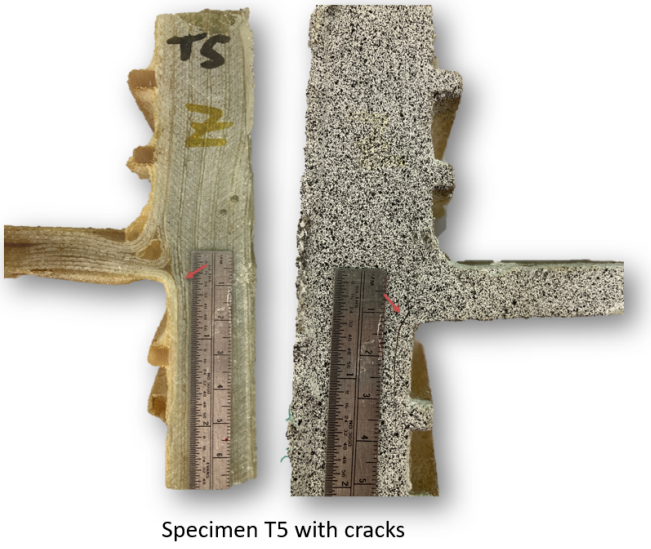

Figure 4.5: Specimen T5 with crack

Figure 4.6: Specimen T3 with crack

4.2. FATIGUE TEST RESULTS

4.2.1. NOMINAL STRESS

To determine the stress the junctions are subjected to during the fatigue tests, the maximum bending stress applied at the first load cycle is calculated. This is done before the junction, where the strain distribution is still linear and unaffected by the geometry of the junction, hence the term 'nominal stress'. The calculation uses the maximum strain recorded by the DIC system, as explained in Section 3.3.5 of Chapter 3. The results of this nominal stress are used to construct the S-N curve. These results are presented in Table 4.2.

Table 4.2: Results nominal strains and stresses from GOM software

WFJ	F (N)	strain DIC (%)	nom_stress (Mpa)
B7	1500	0.4	52.05
B10	1500	0.379	49.3
B4	1000	0.275	35.8
B9	1000	0.156	20.2
B6	400	0.055	7.2
B8	400	0.181	23.6
T2	1200	0.237	30.8
T6	1200	0.155	20.1
B11	600	0.134	17.4
T11	600	0.11	14.3
T11	800	0.104	13.5
T11	1000	0.146	19.0

4.2.2. FATIGUE LIFE

The results from the fatigue tests can be seen in Figure 4.7. The stiffness of the test set-up is calculated by dividing the force by the displacement and plotted against the number of cycles. The red dots on the results graphs indicate the points at which crack initiation occurred in one of the junctions, as determined by the strain limit. Interestingly, some junctions exhibited cracking immediately during the first cycle, which is likely because the variance in dimensions between the specimens which is explained in section 3.2.2 of chapter 3. When this occurred the test was continued to gain insight in the crack propagation, stiffness degradation and to observe if the a crack would initiated at the second junction.

Despite the early cracking observed in some junctions, a notable finding was that there was never a substantial drop-off in stiffness, even after enduring up to 10^6 cycles. This suggests that while the junctions experienced initial damage, their overall structural integrity remained largely intact over an extended period of cyclic loading. This behaviour indicates a degree of damage tolerance in the WFJs, as they continued to maintain their load-bearing capacity despite the presence of cracks. These results underscore

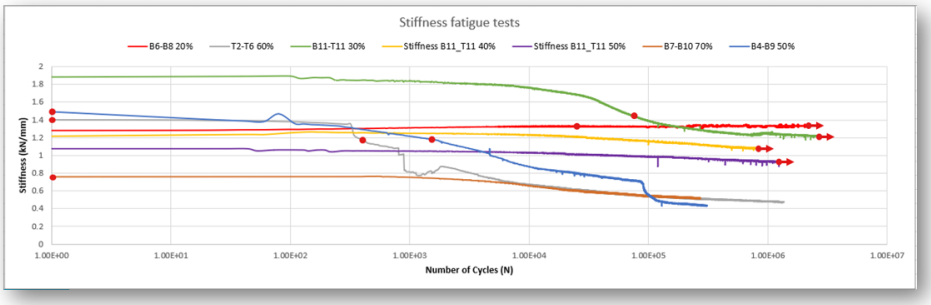

Figure 4.7: Stiffness degradation during fatigue tests (red dots indicate crack initiation)

the importance of understanding and optimising the variability in specimen quality to enhance the predictability and durability of WFJ components.

4.2.3. CRACK DEVELOPMENT DURING STIFFNESS DEGRADATION

For the test specimens B4-B9 and T2-T6, significant stiffness degradation was measured during the fatigue tests. To understand how stiffness degrades as cracks initiate and grow, the crack length is measured for both junctions at specific moments during the fatigue tests where stiffness degradation occurred. These measurements are shown in the graph in Figure 4.8 and correspond to the crack lengths given in Tables 4.3 and 4.4.

In specimen T2-T6, the crack initiated in junction T6 at the first cycle, and later a crack initiated in the second junction T2, corresponding with a significant drop in stiffness. Initially, the cracks grew quite quickly in both junctions, but towards the end, the crack growth slowed down as the stiffness degradation also stabilised.

For specimen B4-B9, no cracks were visible when stiffness degradation began around 1×10^3 cycles. During the stiffness degradation phase, a crack initiated in specimen B9 and grew quickly at first. Just before 1×10^5 cycles, there was a significant drop in stiffness degradation, and a crack became visible in junction B4. After this drop, the stiffness degradation stabilised, and the crack development slowed down.

These two tests show that when a crack initiates in the WFJs, it is initially quite large and corresponds to a drop in stiffness. Initially, the crack grows quickly, but later on, the crack growth slows down, corresponding with a stabilization of the stiffness degradation.

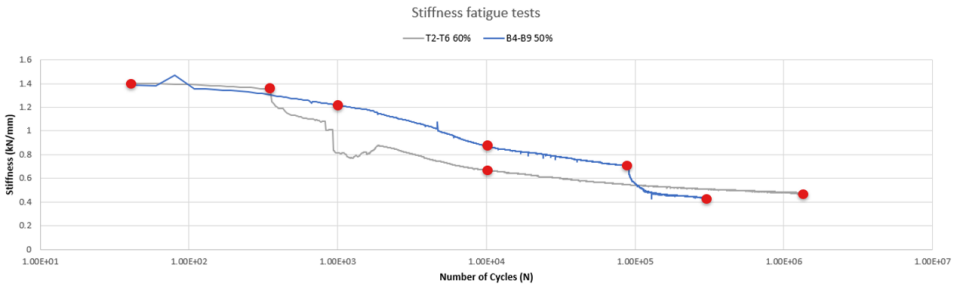

Figure 4.8: Crack length measurements during stiffness degradation. Red dots indicate the crack length measurements provided in Tables 4.3 and 4.4.

Table 4.3: Crack lengths of specimen B4-B9 in (mm)

Specimen	B4-B9	
Junction	B4	B9
cycle 1×10^3	-	-
cycle 1×10^4	-	13.87
cycle 9.15×10^4	15.4	20.68
final cycle	19.4	21.3

Table 4.4: Crack lengths of specimen T2-T6 in (mm)

Specimen	T2-T6	
Junction	T2	T6
cycle 1	-	15.9
cycle 923	9.1	29.14
cycle 1×10^4	21.82	31.52
cycle 1×10^5	29.75	32.49
final cycle	35.4	35.8

Figure 4.9: Fatigue failure mode

4.2.4. FAILURE MODE

The failure modes observed in the fatigue tests of WFJ specimens are notably similar to those seen in the static tests, see Figures 4.9, 4.10 and 4.11. Typically, cracks initiated in the flange at the height of the web and propagated in the direction of the flange. However, there are two significant differences in the fatigue tests compared to the static tests.

Firstly, the cracks observed during the fatigue tests are generally smaller in size. This reduction in crack size is attributed to the lower loads applied during the fatigue tests compared to the static tests. Secondly, for most of the fatigue tests a crack initiated in both junctions in the specimen during the tests, whereas a crack only tended to initiated in one junction during the static tests. This is likely due to the longer duration of fatigue tests, allowing more time for stresses to redistribute after the first junction cracks, leading to a delamination crack in the second junction.

Additionally, in some specimens (B10 and B11 seen in Figure 4.11), cracks are observed at the inside of the radius. These cracks are identified as failures of the excess resin on the outside of the junction, rather than failures of the actual fibres, indicating no significant impact on the structural integrity of the junctions.

CRACK RETARDATION

A phenomenon observed during the fatigue tests was fibre bridging, see Figures 4.13 and 4.14. This occurs when fibres span across a crack, resisting its propagation. As the crack grows, the number of bridging fibres increases, providing additional resistance to crack growth. Fibre bridging thus plays a crucial role in enhancing the durability of the WFJs by resisting crack propagation under cyclic loading conditions.

When a crack has initiated in the WFJ prying forces act on the crack tips causing the

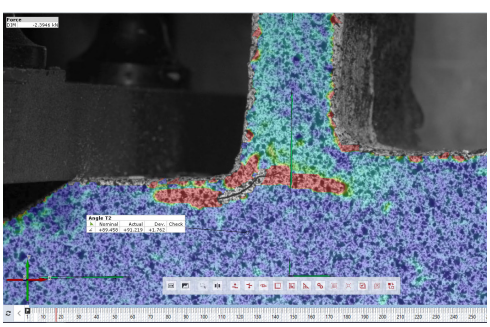

(a) crack in specimen T2, fatigue test

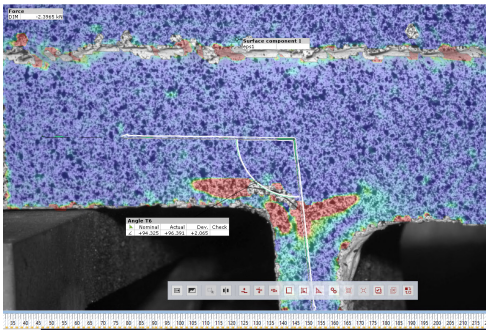

(b) crack in specimen T6, fatigue test

Figure 4.10: Cracks in fatigue test specimens T2-T6

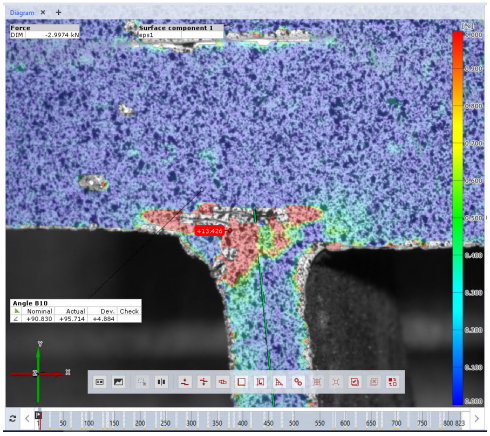

(a) crack in specimen B10

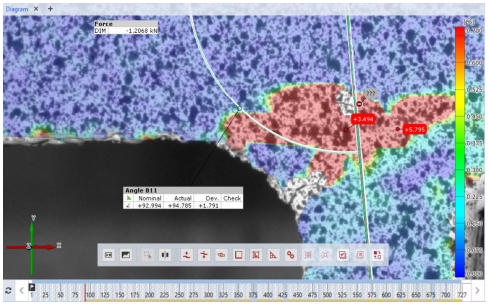

(b) crack in specimen B11

Figure 4.11: Cracks in fatigue test specimens T10-B11

crack to grow by the mode 1 delamination. Because the web is subjected to a bending moment at one crack tip there are tensile forces and at the other crack tip compressive forces that together try to counteract the effective moment where the length of the crack is their lever arm (as illustrated in Figure 4.12). However as the crack grows this lever arm also grows so that the prying stresses reduce if the effective bending moment remains constant (this is also seen in the FEMs given in chapter 5 section 5.2.2). That is why the force resisting capacity of the WFJ can increase after crack initiation and there is retardation of the crack during fatigue tests where the maximum load and thus maximum moment is kept constant.

Of these two phenomena, prying force reduction is the most prominent, as it also explains the sustained moment resistance in the WFJ after crack initiation, whereas crack retardation does not.

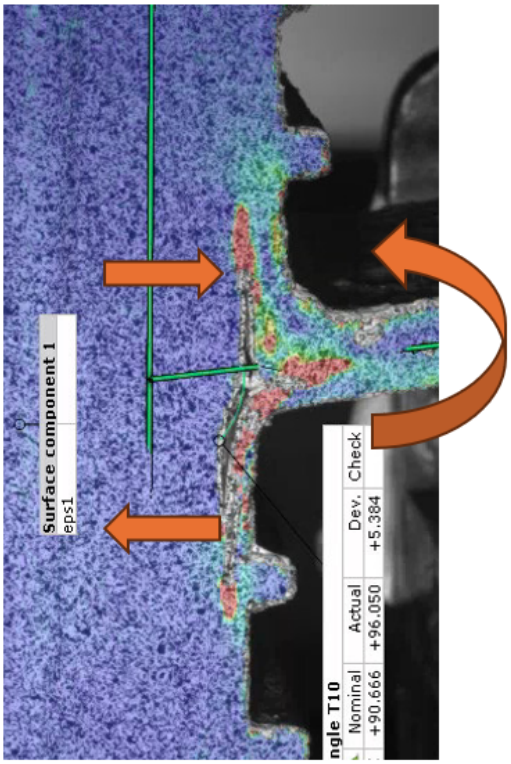

Figure 4.12: Illustration on resisting prying forces at crack tips

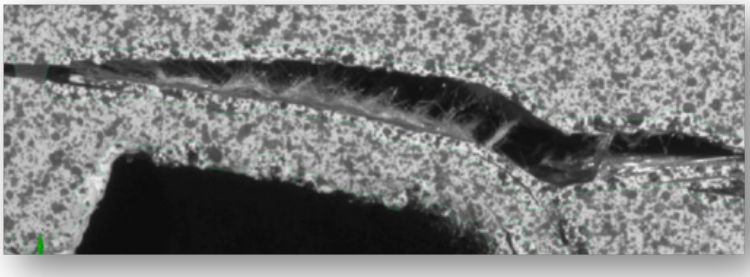

Figure 4.13: Fibre bridging observed from testing

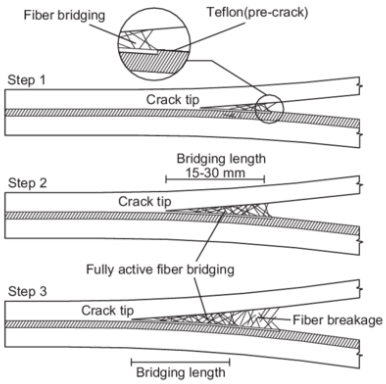

Figure 4.14: Schematic illustration of short fibre bridging development (Shahverdi et al., 2011)

4.2.5. S-N CURVE

The S-N curve is generated using the nominal bending stress given in Table 4.2 and the number of cycles at which the crack initiation strain limit is reached in the specimen. The S-N test data can be found in Appendix E.

The S-N curve is constructed according to the (eq:4.1) where a linear S-N relationship is assumed using the following equations:

$$\log(N) = A + B\log(\sigma_{max}) \tag{4.1}$$

By substituting $\log N$ with Y and $\log(\sigma_{max})$ with X we get the following equation (eq:4.2) from (ASTM International, 2015).

$$\bar{Y} = \hat{A} + \hat{B}\bar{X} \tag{4.2}$$

Where the 'overbar' ($\bar{Y}$) denotes average and the 'caret' ($\hat{A}$) denotes an estimate value. $\hat{B}$ and $\hat{B}$ are calculated using the following equations 4.3 and 4.4.

$$\hat{A} = \bar{Y} - \hat{B}\bar{X} \tag{4.3}$$

$$\hat{B} = \frac{\sum_{i=1}^{k}(X_i - \bar{X})(Y_i - \bar{Y})}{\sum_{i=1}^{k}(X_i - \bar{X})^2} \tag{4.4}$$

Using these equations gives us the values $\hat{A} = 16.788$ and $\hat{B} = -10.112$ as seen in Figure 4.15.

A MN curve is also given for the same test data in the graph in Figure 4.16. This format is more convenient for assessing the fatigue life of the WFJ during design, where the Moment is given per with unit length of the WFJ ($kN \cdot mm/mm$).

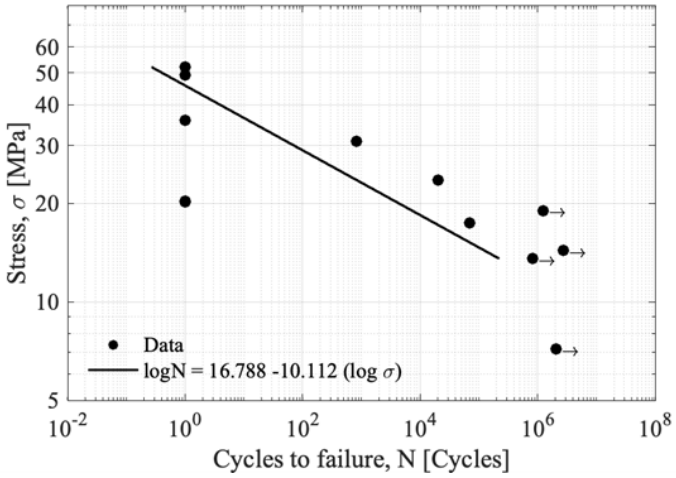

Figure 4.15: S-N curve of the WFJ component tests (Karpenko et al., 2024)

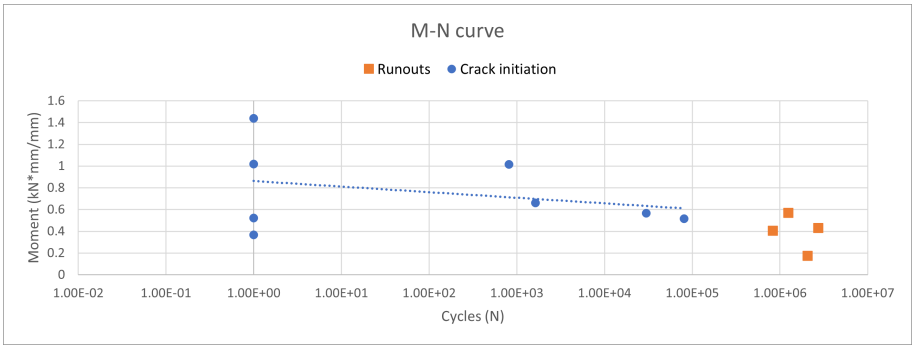

Figure 4.16: MN curve of the WFJ component tests

4.3. IMPORTANT PARAMETERS

Because the dominant failure mode of delamination in the junctions is identified from both the static and fatigue tests. The important parameters influencing this failure can be investigated using analytical equations for a composite curved beam under a constant bending moment given by Lekhnitskii.

The important parameters identified in Sections 2.8.2 and 2.6 of Chapter 2 dictating the crack initiation response are:

- waviness;
- web thickness;
- radius;

The influence of these parameters is investigated by plotting the moment resistance ($M_r = kNmm/mm$) of the WFJ found from testing against each of these parameters. These plots are compared to the theoretical moment resistance ($M_{r,eq}$) found from the equations given in section 2.8.1 of chapter 2, by rearranging the equations as follows (example of equation 2.1):

$$\frac{M}{b} = -\frac{R_o^2 g \sigma_r}{\left(1 - \frac{1-c^{k+1}}{1-c^{2k}}\left(\frac{r}{R_o}\right)^{k-1} - \frac{1-c^{k+1}}{1-c^{2k}}c^{k+1}\left(\frac{R_o}{r}\right)^{k+1}\right)} = \frac{kNmm}{mm} \tag{4.5}$$

This is done for web thickness and radius, but not for waviness as this parameter is not included in the equations. If this fibre waviness parameter would be included in this equation it would need to decrease the moment resistance based on an increased fibre waviness, as explained in section 2.6 of chapter 2. A statistical approach is recommended due to the likely random nature of fibre waviness and the fact that this equation does not account for individual fibres.

For the theoretical moment resistance calculation the value for σ_r is chosen to be $\sigma_r = 24MPa$. This is the transverse tensile strength of the material given by the manufacturer given for the material corresponding to a V_f of 27%. The exact value of this parameter is not crucial for this comparison, it is only essential that it remains constant.

4.3.1. EFFECT WEB THICKNESS

The theoretical moment resistance is calculated using equation 4.5 and varying the web thickness (w_t) parameter while keeping the other parameters constant. The moment resistance for varying web thicknesses is shown in the graph in Figure 4.17. The equation predicts an increase in moment resistance with an increase in web thickness. The test results indicate that this trend in followed uptil a certain web thickness after which the moment resistance of the WFJ drops of with an increased web thickness. Thus from the test results it is found that the web thickness has a positive and negative correlation with the web thickness. It appears from the test results that there might be a parabolic relationship with the web thickness and moment resistance (indicated by the orange dotted

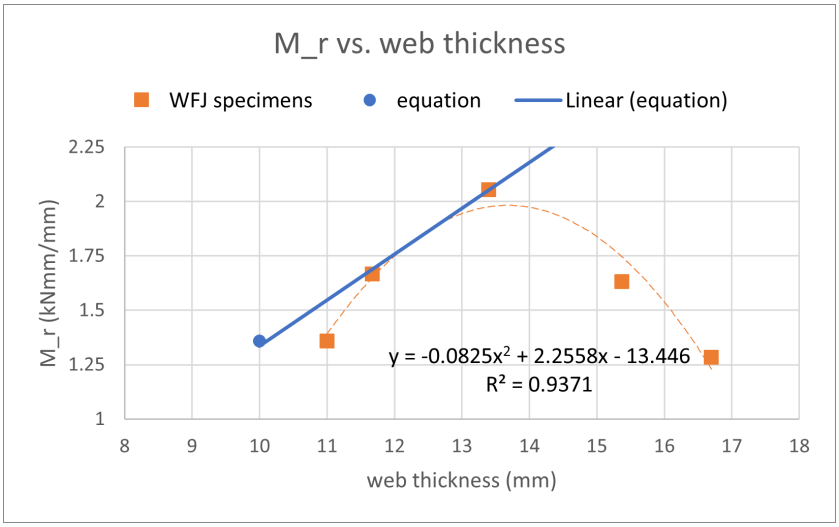

Figure 4.17: Moment resistance vs. web thickness plot

line) indicating that there might be another parameter correlated to the web thickness that effects the moment resistance of the WFJ. This suggests that an increase in web thickness may correlate with an increase in fibre waviness, as identified in chapter 3, and that this increase in fibre waviness causes the moment resistance to decrease.

4.3.2. EFFECT RADIUS

The theoretical moment resistance is calculated using equation 4.5 and varying the inner radius (R_i) parameter while keeping the other parameters constant. The moment resistance for varying web thicknesses is shown in the graph in Figure 4.18. The equation predicts an increase in moment resistance with an increase in radius. The test result indicate neither a positive or negative correlation between the inner radius and the moment resistance of the WFJ.

4.3.3. EFFECT WAVINESS

In the graph in Figure 4.19 the moment resistance of the WFJ specimens is given plotted against the imperfection rating. All the specimens are given an imperfection rating from 1-3 where 1 corresponds to a more imperfections and an increased amount of waviness and 3 is given to specimens with a low amount of imperfections and low waviness as explained in section 3.2.3 of chapter 3. From the literature reviewed in section 2.6 of chapter 2 it is expected that an increased amount of waviness will increase the likelihood of stress concentrations causing the WFJ to fail prematurely. However from test results no such conclusion can be drawn as the specimen with the highest moment resistance as with the lowest moment resistance are the ones with the lowest imperfection rating and thus the highest amount of imperfections.

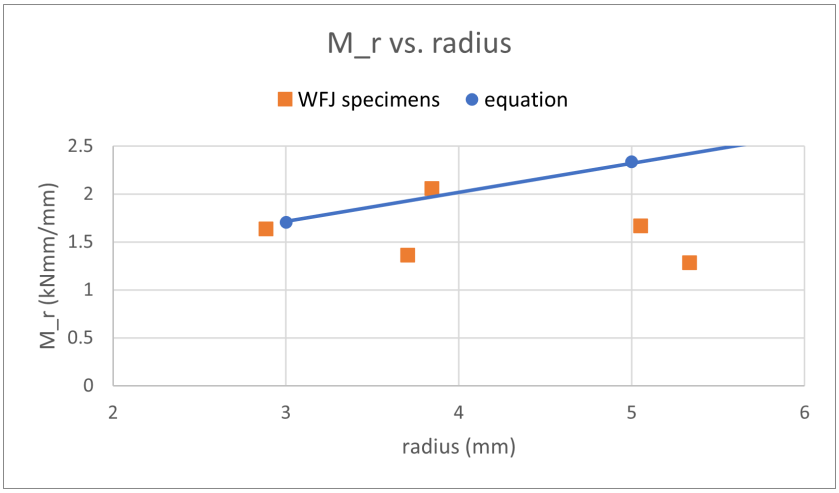

Figure 4.18: Moment resistance vs. radius plot

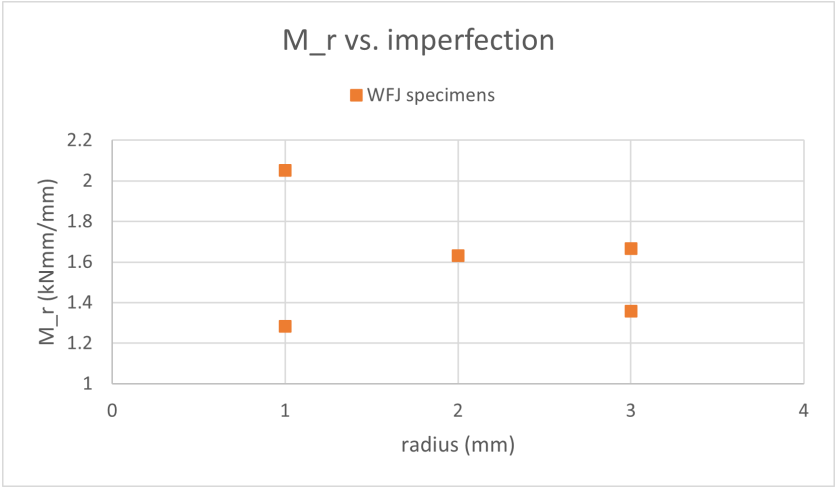

Figure 4.19: Moment resistance vs. imperfection rating plot

In conclusion the theoretical moment resistance is equal or higher that the moment resistance found from testing. The linear relationships between the parameters web thickness and radius correlated to an increased moment resistance predicted by the theoretical equations is not observed from testing. The imperfection rating given to the specimens to investigate the correlation between an increase in waviness and a decrease in moment resistance. From the test results it is not found that there is a negative relationship between an increased amount of waviness and a decrease in moment resistance.

4.4. STATIC TEST RESULTS OF WFJS WITH FATIGUE CRACK

Because it was observed from tests that the WFJ showed damage tolerant behaviour additional static tests are conducted to investigate the post-crack behaviour of the WFJ. These tests aimed to understand how the junctions responded after the initial delamination crack had formed. Specimens are subjected to controlled loading to observe the force-displacement relationship beyond the point of initial failure. The results (seen Table 4.5 and Figure 4.20) show that after the initial crack, the junctions exhibited a significant reduction in stiffness, but they did not lose all their load-bearing capacity. Instead, the WFJs developed a post-crack mechanism where they could still resist loads through increased rotation, allowing the structure to redistribute stresses. This post-crack behaviour indicated a certain level of ductility in the junctions, enabling them to sustain additional deformation and loads despite the presence of cracks. These findings highlight the importance of considering post-crack performance in the design and analysis of the WFJs as additional moment resistance capacity is still available after delimitation crack initiation.

Table 4.5: Stiffness and strength of WFJ with crack

Specimen	WFJ	Static strength (kN)	Kr DIC (kN*mm/mm*rad)	crack length (mm)
B7-B10	B7	2.43	8	39.6
B7-B10	B10	2.43	9.8	25.7
B4-B9	B4	1.47	6.4	19.4
B4-B9	B9	1.47	5.2	21.3
B6-B8	B6	1.21	69	0
B6-B8	B8	1.21	15.5	0
T2-T6	T2	2.67	10.6	35.4
T2-T6	T6	2.67	8.8	35.8
B11-T11	B11	2.43	15.7	22.7
B11-T11	T11	2.43	163	0
B12-T12	B12	2.25	14.3	15.2
B12-T12	T12	2.25	43	6.2
mean		2.06	29.6	19.6
StDv		0.57	45.65	14.45
CoV,%		27.42		

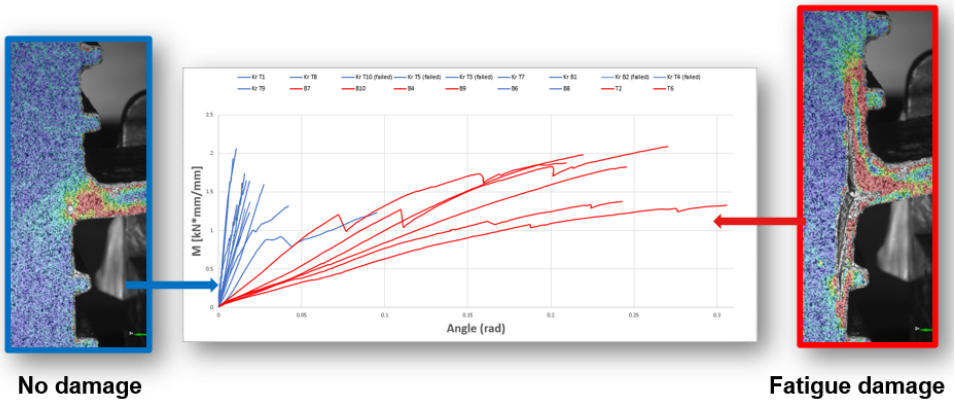

Figure 4.20: Moment rotation plot of WFJs with and without crack

4.5. CONCLUSIONS

In this chapter the findings from experimental tests conducted to assess the static and fatigue response of the WFJ specimens are presented. The primary objectives are to determine the static strength, failure modes, and rotational stiffness of the WFJs, as well as to evaluate their fatigue strength, identify fatigue failure modes, and construct an S-N curve. Static tests reveals that WFJs typically failed through delamination initiated at the interface between laminate layers due to Out-Of-Plane (OOP) tensile stresses, with significant variability in strength attributed to differences in web thickness and waviness. Fatigue tests showed that while some junctions cracked early due to specimen variance, there was no substantial drop-off in stiffness even after 10^6 cycles, indicating damage tolerance.

The important parameters identified in Section 2.8.2 of Chapter 2 effecting the crack initiation response are waviness, web thickness, and radius. The moment resistance at crack initiation from the test results is compared with theoretical predictions. It is found from the test results that web thickness has a non-linear relationship with moment resistance in contrary to the theoretical predictions. It is hypothesised that this is because of correlation between web thickness and waviness found in Section 3.2.3 of Chapter 3. Whereas an increased web thickness is predicted to increase the moment resistance of the WFJ, this is correlated with an increased waviness which is predicted to decrease the moment resistance of the WFJ. A linear relationship between increased radius and an increased moment resistance predicted by the theoretical equations is also not found. This could also be caused due to the same effect of waviness.

The static tests on WFJs with fatigue cracks revealed that after the initial delamination crack, the junctions showed a significant reduction in stiffness but retained some load-bearing capacity. They developed a post-crack mechanism allowing them to resist loads through increased rotation, indicating a level of ductility. This behaviour indicates the consideration of post-crack performance in WFJ design, as they can still sustain additional loads despite the presence of cracks.

5

FINITE ELEMENT MODELLING OF THE WFJ

This chapter focuses on the methodology of developing and validating Finite Element Models (FEMs) to predict the stiffness and stiffness reduction due to fatigue cracks in the WFJ. These FEMs also implement the important parameters effecting this behaviour found in chapter 2 and the dominant failure mode found in chapter 4. This chapter aims to answer the third sub-question of the research:

"Can the fatigue behaviour of the WFJ be predicted by Finite Element Modelling (FEM)?"

5.1. DEVELOPMENT OF FE MODELS

5.1.1. MODELLING APPROACH

The FE model of the WFJ is constructed by combining two L-Junctions together and adding a flange section to create the WFJ, see Figure 5.1. In these L-junctions important parameters identified in chapter 2 are included such as, the web thickness and the inner radius. The outer radius of the L-junction is considered as the outer radius plus the thickness of the L-junction, which simplified the model to have a constant width cross-section. This approach is done so that important parameters influencing the mechanical behaviour of the WFJ are modelled.

5.1.2. MATERIAL PROPERTIES

The material properties for the FRP composites are modelled as homogenised materials using classical laminate theory. Table 5.1 lists the homogenised properties used in the FEMs. For the resin rich area between the two L-Junctions(see Figure 5.2) the modulus of elasticity for Unsaturated polyester (UP) used in the WFJ is obtained from (Ronald Grefhorst, 2020) and the poisson ratio for polyester is obtained from (Hindawi, 2019) and are given in Table 5.2.

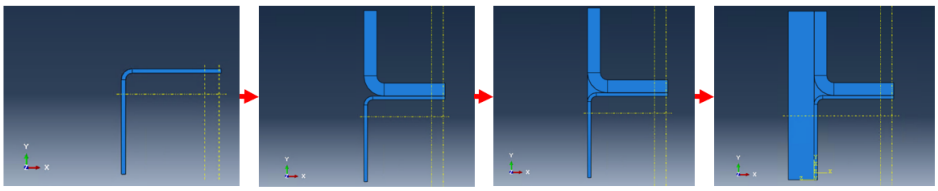

Figure 5.1: Assembly of WFJ in FEM

Table 5.1: Homogenised Properties for FEM (stiffness moduli in MPa)

Part	Vf%	E1	E2	E3	v12	v13	v23	G12	G13	G23
Web	36	13013	13013	13013	0,37	0,37	0,37	6668	6668	5036
Flange	54	19559	33119	19559	0,16	0,26	0,16	5578	5578	5484

Table 5.2: Material properties of Unsaturated polyester (UP)

Modulus of elasticity (MPa)	3300
Poisson ratio	0.44

5.1.3. MESH

The mesh is constructed from solid elements using linear hexahedral elements of type C3D8R. Each of the parts, as shown in Figure 5.1, has been meshed separately and the mesh density is determined based on the thickness of the part and its importance to the analysis. The two L-Junctions have the most dense mesh because they include the most important parameters and are the locations where the highest stresses/deformations occur. For specimen T2 for example, the bottom L-Junction has a mesh size of 1 mm for a thickness of 3 mm and the top L-Junction has a mesh size of 2 mm for a thickness of 11.08 mm.

5.1.4. LOAD AND BOUNDARY CONDITIONS

The load and boundary conditions are applied to the WFJ model in Abaqus, as shown in Figure 5.3. The flange is fixed, and the load is applied over an area with a center-to-center distance of 60 mm from the inner flange to create a bending moment similar to that during the physical tests. This setup created a cantilever configuration, which is statically determined. The WFJ is clamped at the side edge, with all displacements and rotations fixed (U1 = U2 = U3 = UR1 = UR2 = UR3 = 0). The maximum resistance load measured during testing is used as the applied load in the FEMs.

5.1.5. MODELLING OF CRACKS

As observed from the test results the presence of cracks, is a significant factor affecting the rotational stiffness of the WFJ. To model this, the surface-to-surface contact between the flange and L-junction is removed for the length of the crack, see Figure 5.4. For instance, in specimen T2, a fatigue crack of 35 mm is observed, which grew to 45 mm after

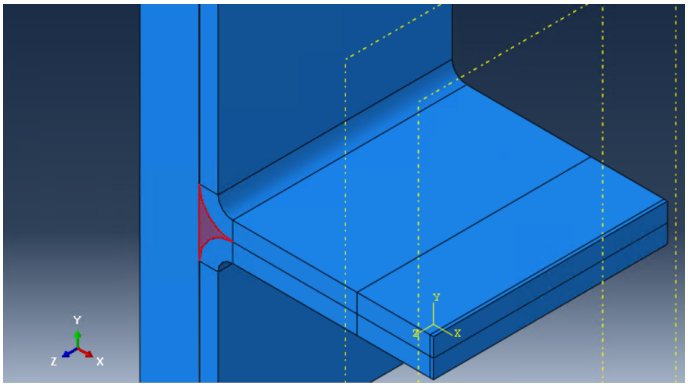

Figure 5.2: Modelling of the Resin rich area in the WFJ

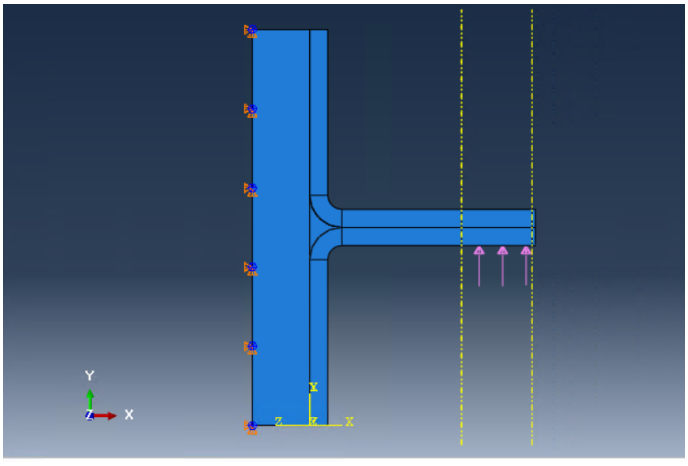

Figure 5.3: WFJ load and boundary conditions in Abaqus

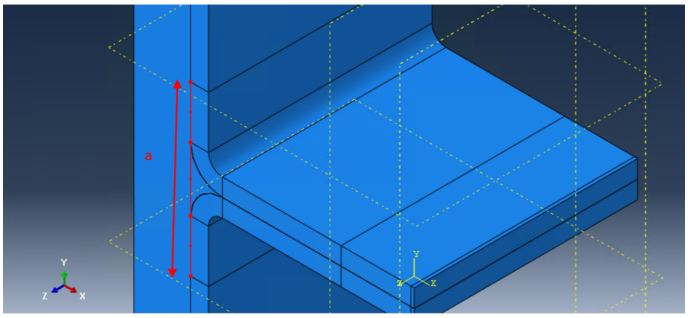

Figure 5.4: Modelling of crack length a

static testing. This crack is modelled by creating a discontinuity in the FEM to simulate the lack of bond and the resulting stress concentration at the crack tips. The crack length and location are measured using the GOM Correlate software, ensuring accurate representation in the FEM.

5.1.6. GEOMETRY PARAMETERS

The geometry parameters for the L-junctions and the WFJ are defined to ensure the model's accuracy and representation of the test specimens, see Figure 5.5. The dimensions of the L-junctions, including web thickness, flange thickness, flange height, and radii, are measured from the physical specimens. These dimensions are hypothesised to be critical for predicting the rotational stiffness of the specimens in the FEM. Tables 5.3 and 5.4 provide the geometry parameters used for specimens T4 and T2, respectively.

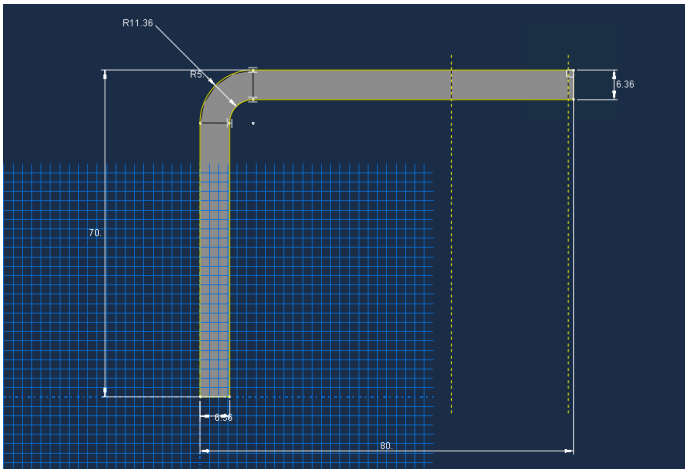

Figure 5.5: L-Junction Dimensions

Table 5.3: Geometry T4

Parameter	Value
WFJ	T4
Web thickness (mm)	11
Flange thickness (mm)	27.25
flange height (mm)	142
width (mm)	79
hw_1	65
hw_2	66
Web length (mm)	69.75
$R1$ (mm)	3.70
$R2$ (mm)	9.53
r_{crack} (mm)	7.47
$R1_{\text{out}}$ (mm)	14.70
$R2_{\text{out}}$ (mm)	20.53
Fail Junction (kN)	1.788
Imperfection rating	3

5.2. MODEL VALIDATION WITH EXPERIMENTAL DATA

The validation of the Finite Element Models (FEMs) is conducted by comparing the simulation results with the experimental data obtained from static tests of the WFJ specimens. This process involves analysing rotational stiffness, vertical displacement, and stress distributions to assess the accuracy and reliability of the FEMs.

5.2.1. NON-CRACKED WFJ

For the non-cracked WFJ, specimen T4 is used as a reference. The FEM results for specimen T4 can be found in Table 5.5, showed a very close match with the experimental data in terms of rotational stiffness. The applied force and resulting bending moment produced similar rotations in both the FEM and the physical tests, indicating that the web thickness and radii are crucial parameters for accurately modelling the rotational stiffness of the WFJ. It is important to note that the rotation measured using the GOM Correlate software is more precise, isolating the rotation of a single WFJ and providing a more accurate measurement as explained in section 3.3.5 of chapter 3. In contrast, the FE program lacks such tool, and therefore the bending of the web is also included in the rotation calculation, making it not a perfect comparison with the test specimen.

There is a significant difference in vertical displacement recorded by the testing machine (UTM-25), with the experimental setup showing more than twice the displacement observed in the FEM. The vertical displacement is also measured using the DIC data by measuring the displacement of a fixed point on the WFJ as seen in Figure 5.11. Here the measured displacement of 1.445 mm is much closer to the 1.352 mm found

Table 5.4: Geometry T2

Parameter	**Value**
Number	T2 (with crack)
Web thickness (mm)	14.067
Flange thickness (mm)	29.5
Flange height (mm)	146
Width (mm)	81
Web length (mm)	66.5
$R1$ (mm)	4.58
$R2$ (mm)	6.22
r_{crack} (mm)	7.57
$R1_{out}$ (mm)	20.54
$R2_{out}$ (mm)	22.47
Fail Junction (kN)	1.62
crack length (mm)	44.87
Imperfection rating	2

in the FE model. The DIC data is considered more accurate and reliable, and thus more representative of the actual displacement of the specimen. This discrepancy in displacement is likely due to the additional displacements in the test system, such as those from the second WFJ and the compression at the contact points. The FEM, being a simplified representation, did not account for these factors, leading to the observed difference.

Table 5.5: Comparison results specimen T4 Test vs. FEM

	T4 specimen	T4 FEM
Moment (kN*mm/mm)	1.358	1.358
Vertical displacement (UTM-25) (mm)	2.601	1.352
Vertical displacement (DIC) (mm)	1.445	1.352
Rotation (rad)	0.0189	0.0183
Kr (kN*mm/mm*rad)	74.074	73.941
OOP Stress (MPa)	20.559	24.40

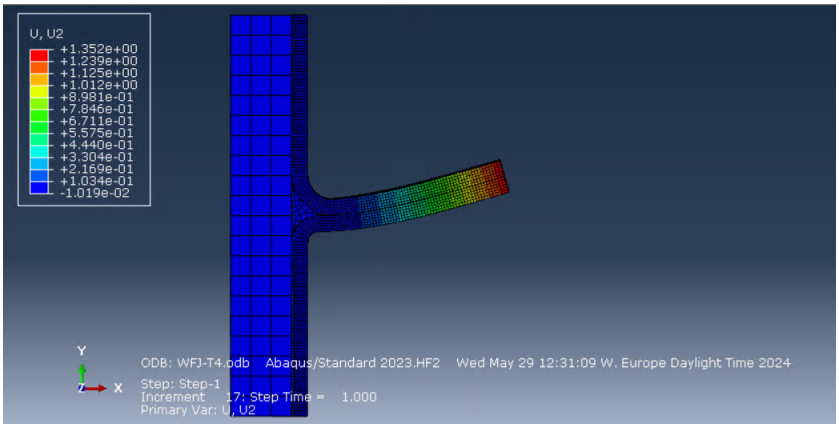

Figure 5.6: Deformation of T4 FEM

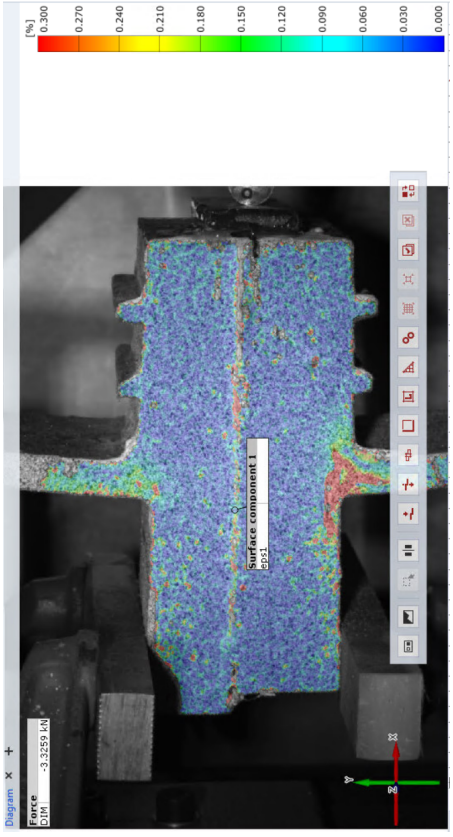

Figure 5.7: Test of T4 specimen

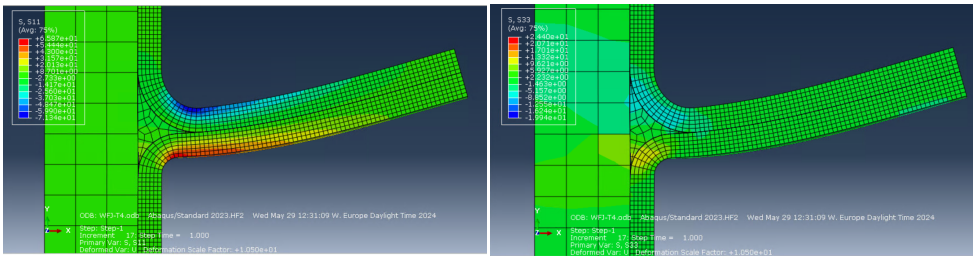

(a) Stress in fibre direction (MPa)

(b) OOP stress (MPa)

Figure 5.8: Stresses in WFJ T4 (MPa)

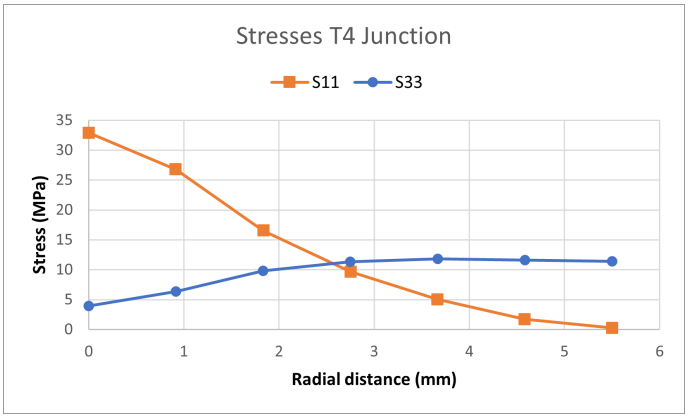

Figure 5.9: Stress plot of Junction T4

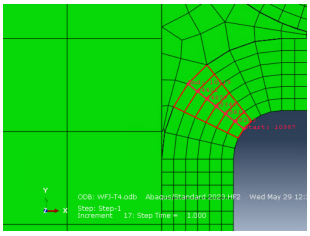

Figure 5.10: Plot line T4

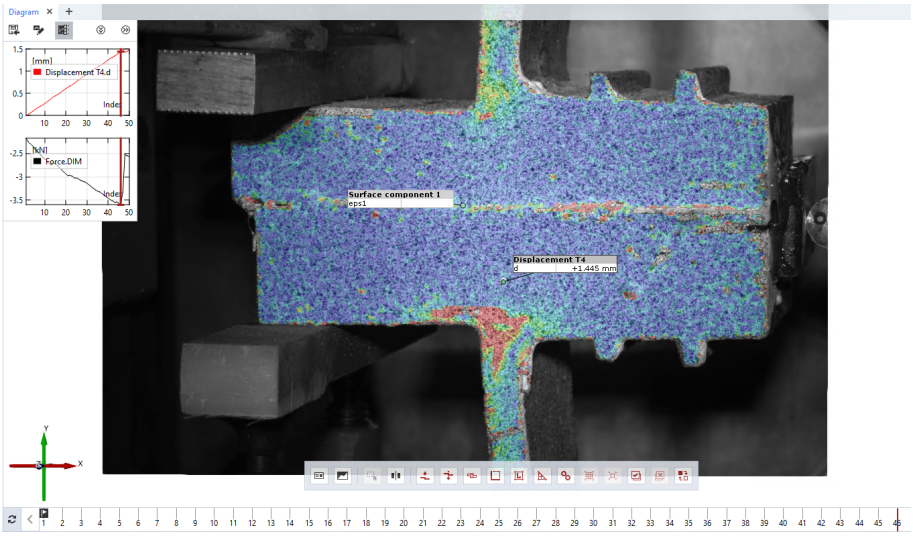

Figure 5.11: Displacement measurement of T4 DIC data

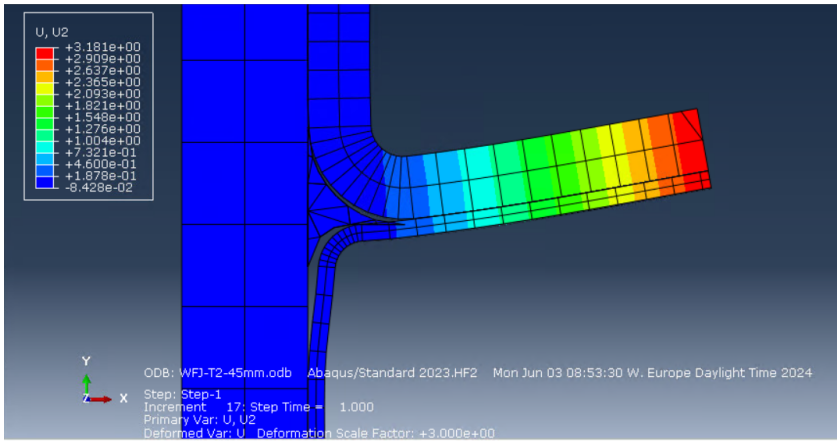

Figure 5.12: Deformation of T2 FEM, with 45 *mm* crack

5.2.2. CRACKED WFJ

The FEM of the cracked WFJ, specifically specimen T2 with a fatigue crack of 35 *mm* that grew to 45 *mm* during static testing, is used to evaluate the model's ability to simulate the effect of cracks on rotational stiffness. The presence of the crack is modelled by removing the surface-to-surface contact in the affected area, which allowed for more flexibility and increases rotation in the junction. The FEM results for the cracked specimen showed a reduction in rotational stiffness, aligning with the experimental observations (see Table 5.6 and Figure 5.12). However, the FEM underestimated the stiffness reduction by approximately 23.6%. This underestimation indicates that additional parameters are needed to more accurately predict the rotational stiffness of the WFJ with a crack. These parameters could be a degradation of material stiffness or the use of cohesive zone modelling.

Table 5.6: Comparison results Test vs. FEM, T2

	T2 specimen	T2 FEM
Crack length (mm)	44.87	44.87
Moment (kN*mm/mm)	1.20	1.20
Vertical displacement (mm)	5.85	3.181
Rotation (rad)	0.072	0.053
Kr (kN*mm/mm*rad)	17.28	22.61

STRESS ANALYSIS OF CRACK GROWTH

In specimen T2, after fatigue testing, a crack length of 35 *mm* is observed, which extended to 45 *mm* during subsequent static testing (see Figure 5.14). The FEM included these crack lengths by removing the surface-to-surface contact along the crack path, thus replicating the stress concentration and deformation behaviour seen in the physi-

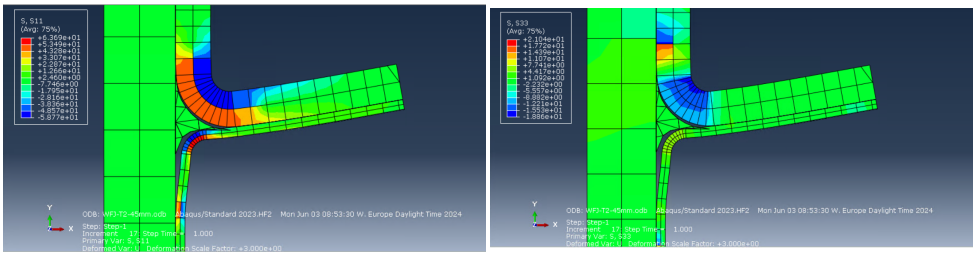

(a) Stress in fibre direction (MPa)

(b) OOP stress (MPa)

Figure 5.13: Stresses in WFJ T2 (MPa)

cal tests.

The stress analysis, shown in Figure 5.14, reveals that as the crack length increases, the stress at the crack tips decreases. This phenomenon is attributed to the increases lever arm effect at the crack tips, which results in smaller stresses reacting to the applied bending moment. For instance, the OOP stress (S33) at the crack tip for a 35 mm crack is 13.8 MPa, while for a 45 mm crack, it reduced to 6.0 MPa. This reduction in stress at the crack tip with increasing crack length suggests a retardation of crack growth, indicating that the ultimate resistance load can be sustained even as the WFJ begins to crack.

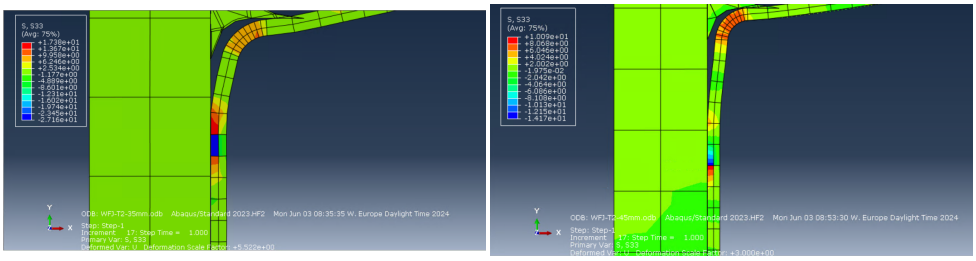

(a) 35 mm crack (13.8 MPa at crack tip)

(b) 45 mm crack (6.0 MPa at crack tip)

Figure 5.14: Through Thickness Stress (S33) at crack tip WFJ T2 (MPa)

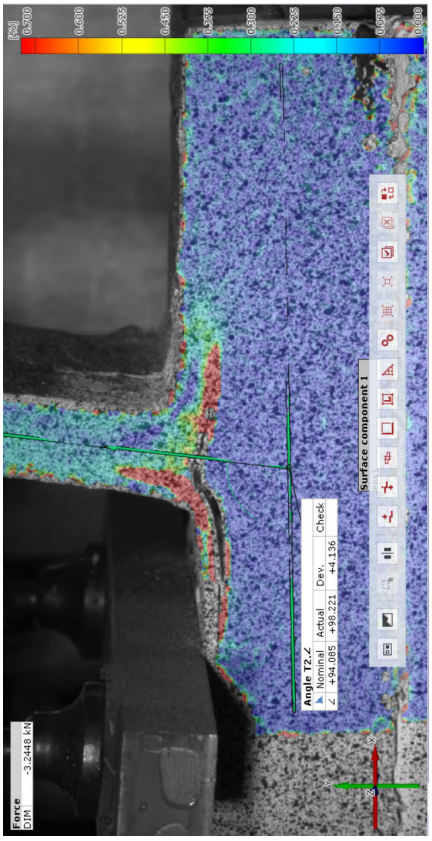

Figure 5.15: 45 *mm* crack after static testing in test specimen T2

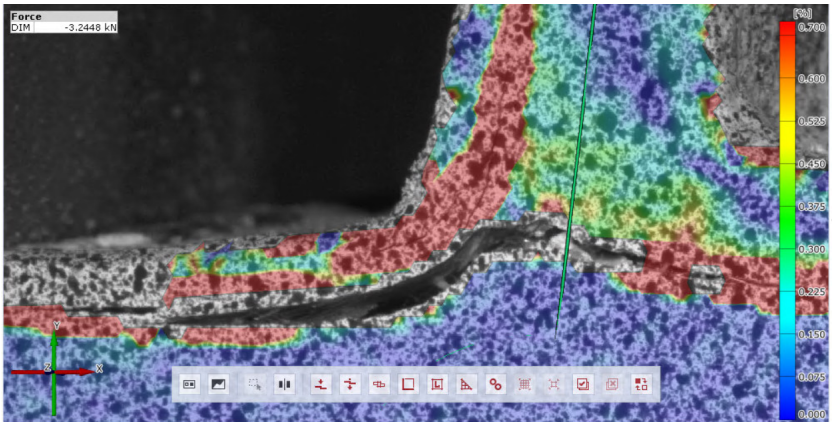

Figure 5.16: small cracks specimen T2

5.3. PREDICTIVE CAPABILITIES OF FEM

The Finite Element Models (FEMs) developed for the Web-Flange Junction (WFJ) demonstrated predictive capabilities in simulating the mechanical behaviour under static loading conditions. The FEM of the non-cracked WFJ closely matched the experimental results, showing less than 1% difference in rotational stiffness. This confirms that the key geometric parameters, such as web thickness and radii, are crucial and sufficient for accurately modelling the rotational stiffness of the WFJ.

However, the FEM for the WFJ with a 45 mm crack, while effectively demonstrating the increases flexibility and rotation due to the crack, showed a 23.6% underestimation in stiffness reduction compared to the experimental results. This discrepancy indicates that additional parameters are necessary to more accurately predict the rotational stiffness of the WFJ with crack, such as the material stiffness degradation or the appliance of cohesive zone modelling.

The analysis also reveals that greater crack lengths resulted in lower stresses at the crack tips, explaining the retardation in crack growth and the increases ultimate load resistance observed after crack initiation in chapter 4. The FEMs provided valuable insights into the stress distribution and deformation patterns, validating their use in predicting the fatigue behaviour of the WFJs. Despite the limitations, the FEMs proved to be effective tools for understanding the impact of important parameters on the response of WFJs.

6

DISCUSSION

In this chapter, the findings of this research are discussed, interpreting their significance and implications. It examines their effect on the use Web-Core Sandwich Panel bridge decks and on verifying the fatigue life of the WFJ component. Also, the chapter reviews the limitations of the methodology and the results of this research is examined, aiming to provide a balanced perspective on the research outcomes. Finally, it offers recommendations for future research to address these limitations and enhance the impact of future studies.

6.1. INTERPRETATION OF STATIC AND FATIGUE BEHAVIOUR

6.1.1. STATIC BEHAVIOUR

The static tests consistently showed delamination as the primary failure mode at the same location, making the WFJ response to bending more predictable. However, the variability in the specimens resulted in a wide range of test outcomes. This variability provided an opportunity to investigate the impact of critical parameters on the performance of WFJs.

These findings allow designers to optimise the component based on the identified failure mode and the key parameters influencing this response. Also future research of the performance of WFJ should focus on this failure mode and weather this is still the dominant failure mode under different loading conditions.

6.1.2. FATIGUE BEHAVIOUR

Fatigue tests also revealed mode 1 delamination as the predominant failure mode, with observed crack retardation behaviour indicating a stabilisation phase before failure. This consistent failure mode simplifies the analysis and highlights the critical areas for improving fatigue resistance.

This dominant failure mode is particularly interesting because verifying the safety of FRP composites is often complicated by the presence of multiple failure modes, which can vary depending on the layup. However, for this component under this specific loading case, this research indicates that potentially only one main failure mode needs to be verified. This would simplify the verification process for designers. Additionally, this understanding allows designers to optimise the WFJ component based on the identified failure mode and the key parameters influencing this response. It also opens up the possibility of implementing measures to enhance resistance to Mode 1 delamination. Existing research provides insights on how to achieve this (Wang and Soutis, 2017, Burns et al., 2015).

S-N CURVE

Constructing an S-N curve presented challenges, as some WFJs either failed on the first cycle or did not fail within the test duration. The slope of the S-N derived for the WFJ in this research given in section 4.2.5 of Chapter 4 is $k = -10.112$. In comparison, the general S-N curve slope for steel is -3 (CEN, 2005), see Figure 6.2, indicating that this component has a better fatigue life than steel and also indicating that the fatigue performance for OOP tensile stresses in GFRPs is better than that of steel.

Because in a few of the specimens the crack initiated at the first cycle this skews the test results and has a negative influence on the S-N curve generated. An alternative S-N curve is generated where the 1 cycle crack initiation tests are left out, given in Figure 6.1, with a slope of $k = -19.58$. This indicates that the fatigue life of the WFJ component could be much better if the fatigue tests are performed in such a way that the 1st cycle crack initiation could be avoided.

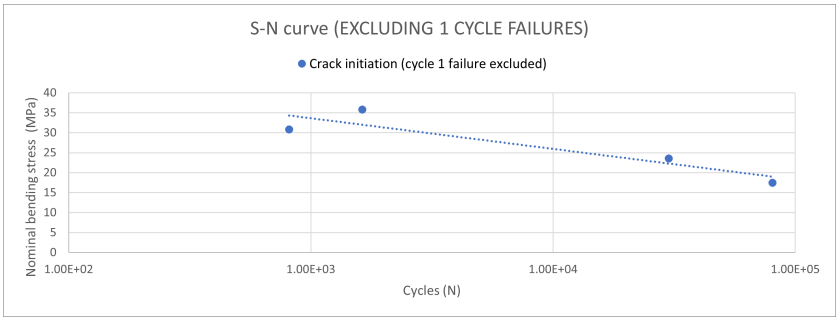

Figure 6.1: S-N curve excluding the crack initiation at 1st cycle

There is limited information available on the out-of-plane (OOP) tensile stress fatigue life for GFRP composites. When examining comparable S-N curves, we find that the WFJ has a worse fatigue life than GFRP coupons stressed in the off-axis direction 90° with an R value of $R = 0.1$ with a slope of $k = -14.29$ given by (Vassilopoulos and Keller, 2011), see Figure 6.3. Additionally, the WFJs fatigue life is inferior to that of CFRP L-bent

coupons, which have found to have a S-N curve slope of $k = -21.60$ by (Allegri, 2019), see Figure 6.4.

This indicates that while the OOP tensile stress fatigue life for GFRP found in this research is higher than that of steel, it is lower than that of comparable S-N curves from FRP composites. This highlights the fact that OOP tensile stresses could be more critical for the fatigue life GFRP components and designers should take these stresses into consideration for their fatigue design. Also the current design codes don't provide S-N curves for OOP tensile stresses for GFRP materials. It would be recommended to include these S-N curves in the design codes derived from standardised tests such as the (ASTM, 2004), which is the standard test method for measuring the curved beam strength of a FRP composites. If these S-N curves would be added to the design standards it would allow designers to verify the safety of GFRP components where OOP tensile stresses are the most critical fatigue stresses.

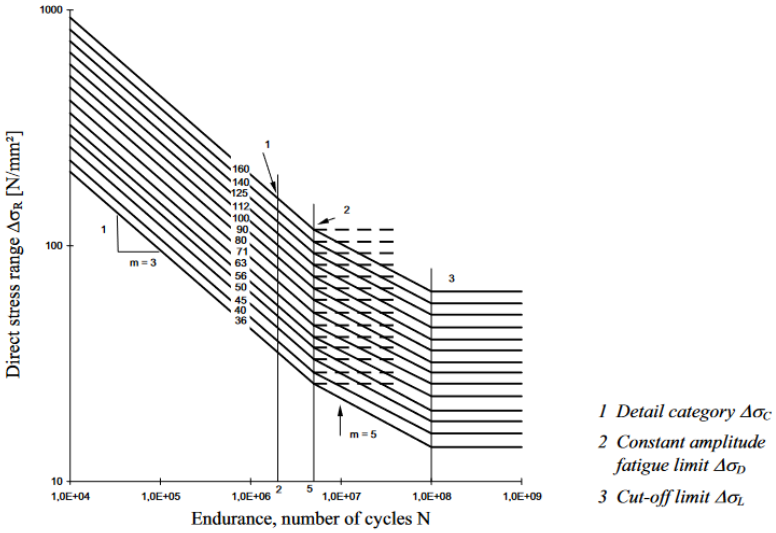

Figure 6.2: S-N curve for steel (CEN, 2005)

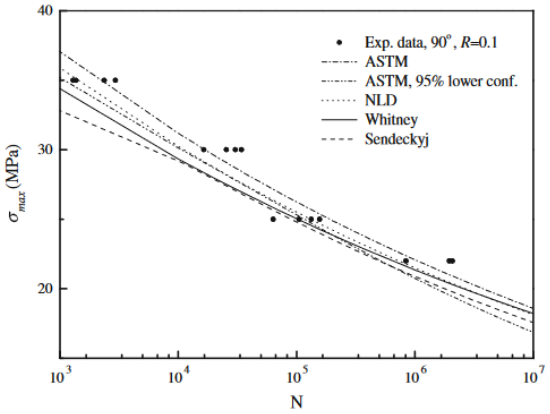

Figure 6.3: Reliability-based S–N curves for 90° off-axis specimens, R = 0.1(Vassilopoulos and Keller, 2011)

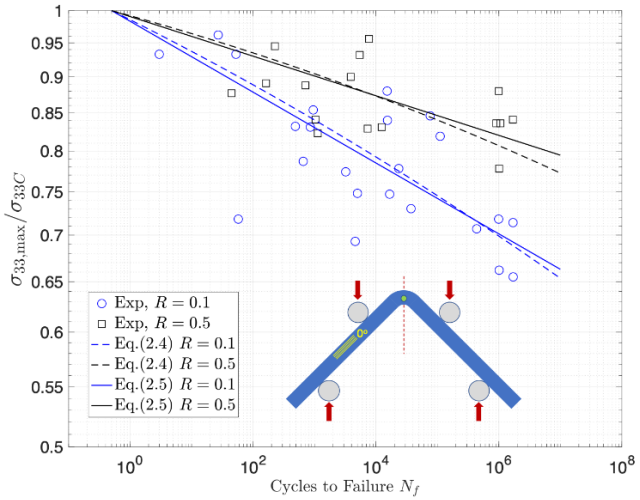

Figure 6.4: S-N curves for delamination onset under inter-laminar tension in IM7/8552 L-bend coupons; experimental data from (Allegri, 2019)

6.2. REVIEW OF SAFE-LIFE APPROACH

In this research the safe-life approach is used to determine the fatigue life of the WFJ. Using this approach the fatigue life is determined to be the number of cycles the WFJ can sustain until a crack is initiated. These test results are used to construct an S-N curve to predict the fatigue life of the WFJ.

While the safe-life approach has its benefits (discussed in chapter 3) it also has notable drawbacks. The requirement for components to remain damage-free often leads to overly conservative designs, resulting in increased material usage and higher costs.

6.2.1. CONSIDERATION OF DAMAGE-TOLERANT APPROACH

During the fatigue tests in a number of WFJ specimens a delamination crack already initiated at the first cycle, below the mean static strength load found from testing. However, the test results indicated that after the initial delamination crack, WFJs did not fail immediately but exhibited a post-crack mechanism allowing them to sustain additional loads. This behaviour suggests that WFJs possess a certain level of damage tolerance, where the structure can redistribute stresses and maintain integrity even after initial damage. Adopting a damage-tolerant approach would involve periodic monitoring of the junctions, employing non-destructive evaluation techniques to detect early signs of damage, and implementing repair strategies to extend the service life of the structure.

Given the test results from this research, a damage-tolerant approach might be more appropriate for WFJs in GFRP WCSP bridge decks. The damage-tolerant approach accepts that some level of damage, such as small cracks or delamination, is inevitable under cyclic loading. Instead of designing for absolute damage prevention, this approach focuses on the ability of the structure to tolerate and manage damage through regular inspection, maintenance, and repair.

6.3. IMPORTANT PARAMETERS AFFECTING WFJ PERFORMANCE

Key parameters influencing WFJ performance include waviness, web thickness, radii, with web thickness and waviness likely having the most significant impact. With this knowledge designers can optimise the performance of the WFJ by accounting for these parameters.

6.4. COMPARISON OF EXPERIMENTAL RESULTS WITH FEM PREDICTIONS

The FEM model accurately predicted the rotational stiffness of non-cracked WFJs, although this may be coincidental. For WFJs with a fatigue crack, the FEM model overestimated rotational stiffness, indicating the need for additional parameters to enhance prediction accuracy. Potential improvements include incorporating material stiffness reduction and cohesive zone modelling to better simulate the behaviour of cracked WFJs.

This accuracy could potentially be part coincidence as the bending of the web is also included in the displacement in the FE model as for the test specimen this bending of the web could be ignored by the GOM Correlate software.

6.5. IMPLICATIONS FOR DESIGN AND MANUFACTURING

To enhance the performance and reliability of WFJs, efforts should focus on reducing imperfections during manufacturing. Ensuring uniform web thickness and minimising waviness can potentially improve the mechanical performance and fatigue resistance of the junctions.

6.6. LIMITATIONS OF RESEARCH

The methodology of this research aimed to determine the fatigue life of the Web-to-Flange Junction (WFJ) component using the safe-life approach. This involved determining the static strength of the WFJ through static tests and conducting fatigue tests based on percentages of the mean static strength. The fatigue life was assessed at the moment of crack initiation. Analytical equations web thickness, and radius as important parameters influencing the crack response to bending of the web. Prior research (Sebastian, 2018, Trask et al., 2012) identified fibre waviness as an important parameter effecting this response. To account for the waviness parameter, specimens were categorised by imperfection ratings based on visual inspection.

A novel experimental strategy was devised wherein two WFJs were glued together and placed in a three-point bending test setup, allowing both junctions to be loaded by statically determined forces from the supports. While this setup simplified the testing process, it had limitations. In static tests, only one junction typically failed, and during fatigue tests, the internal bending moment redistribution could be altered if the rotational stiffness of one junction decreased significantly due to cracking. Specimens were combined based on similar imperfection ratings and web thickness to maximise symmetry. However, the imperfection rating was partly subjective and non-quantifiable, and no linear relationship between the imperfection rating and the moment resistance of the WFJ was found.

(Sebastian, 2018) suggests using a sharp-pointed marker to highlight dots on transparent plastic sheeting to determine the waviness profile and define equations that closely fit particularly wavy profiles, see Figure 6.5. Additionally, all specimens in this research were sourced from a single bridge deck with the same layup from one supplier. This limits the generalisability of the findings. Future studies should include additional tests on WFJs with different layups and geometries to investigate the response and sensitivity to imperfections.

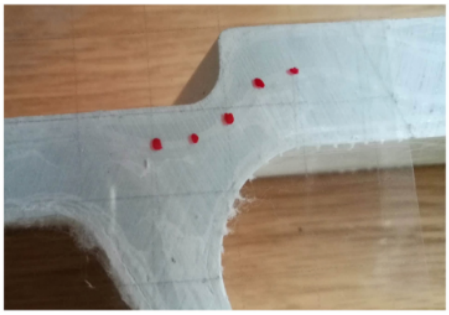

(a)

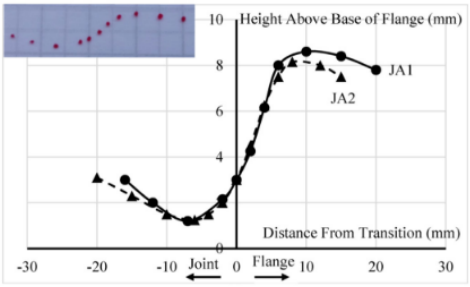

(b)

Figure 6.5: Defining fibre waviness using pointer marker and line fitting (Sebastian, 2018)

6.7. FUTURE RESEARCH

Future research should focus on several key areas to build on the limitations in the findings of this research:

- Quantitative Waviness Measurement: Implementing more quantitative methods for characterising waviness, such as those suggested by (Sebastian, 2018), will improve the precision of the measurements and their correlation with the structural performance of WFJs. Using statistical approaches to determine the effects of waviness on the fatigue of the decks.

- Diverse Load Types: Expanding the research to include different load types, such as rolling loads from wheels and different R values, will provide a more comprehensive understanding of the WFJ's behaviour under various real-world conditions. This will help in developing more robust predictive models for crack propagation and panel performance. As these different load types might have an effect on the crack propagation.

- Delamination Focus: Future research should concentrate on the delamination failure mode and the out-of-plane (OOP) stresses that cause it. Developing S-N curves based on these OOP stresses will aid designers to verify the fatigue life of components where this is the dominant failure mode and enhance the predictability of fatigue life in WFJs.

- Variety of Panels and Suppliers: Including a broader variety of panel combinations from multiple suppliers will help generalise the findings and ensure their applicability across different manufacturing processes and composite lay-ups.

- Enhanced Experimental Setups: Using alternative test setups, such as in (Cintra et al., 2021, Yanes-Armas et al., 2016), that involve the testing of one single WFJ independently could lead to more accurate and reliable results.

By addressing these areas, future research can build on the understanding of the fatigue behaviour of WFJs in GFRP Web-Core Sandwich Panels, leading to improved design practices and enhanced durability and safety of these bridge decks.

7

Conclusions and Recommendations

7.1. Summary of Key Findings

The research aimed to investigate the fatigue behaviour of the web-to-flange junctions (WFJs) in a glass fibre reinforced polymer (GFRP) web-core sandwich panel bridge deck subjected to bending. The key findings from the test results and further analysis are:

- Mode 1 delamination is dominant failure mode for both static and fatigue behaviour caused by OOP tensile stresses.
- Fatigue tests showed progressive stiffness degradation and crack retardation, indicating a stabilisation phase before ultimate failure. After the delamination crack initiates, a post-crack mechanism develops, ensuring the WFJs still have some bending moment resistance. From FEM analysis it was found that the stresses at the crack tips reduce as the crack grows. This, combined with fibre bridging, leads to crack retardation.
- The most important parameters effecting the delamination crack initiation response are; web thickness, radii and waviness. A direct correlation between each of these parameters and rotational stiffness was not found from the test results. This is likely because there was a correlation between web thickness and fibre waviness.
- Finite Element Modelling successfully predicted the rotational stiffness of the WFJ specimen before crack initiation validating the influence of the important parameters
- FEM overestimated the rotational stiffness of the WFJ of the post-crack response, indicating the need for additional parameters such as material stiffness degradation or cohesive zone modelling.
- After crack initiation, moment resistance remains but rotational stiffness degrades.

7.2. ANSWERS TO RESEARCH QUESTIONS

The research aimed to understand the fatigue behaviour of the Web-Flange Junction (WFJ) in a Glass Fibre Reinforced Polymer (GFRP) Web-Core Sandwich Panel (WCSP) deck subjected to bending. The study addressed the following key research questions:

1. What is the static and fatigue response of the WFJ subjected to bending?

    - The static tests revealed significant variability in the static strength and rotational stiffness of the WFJs, influenced by factors such as web thickness and waviness. The failure modes were consistent, with delamination cracks typically initiating at the interface between the 'wrap' layer and the 'UD-layer' (see Figure 7.1). The fatigue tests also showed delamination as the dominate failure mode. While the WFJs specimens showed a high sensitivity to delamination cracks, some specimens already having crack initiation at the first cycle. After a delamination crack occurred the specimens were observed to be damage tolerant with a stabilisation of stiffness degradation and crack propagation.

2. What are the most important parameters determining this behaviour?

    - The study identified web thickness, radius and waviness as critical parameters affecting crack initiation response of the WFJs. Analytical methods highlighted the significance of these parameters in determining the mechanical behaviour and failure modes of the junctions. A linear relationship between these parameters and the bending moment resistance, as predicted by the analytical equations, was not found. This is likely due to a correlation between web thickness and fibre waviness, found in section 3.2.3 of chapter 3 (see Figures 7.2 and 7.3).

3. Can this behaviour be predicted by Finite Element Modelling (FEM)?

    - The developed FEM was successful in predicting the rotational stiffness of the WFJ without cracks. Validating the important parameters needed to predict this response. The FEM model of the WFJ with fatigue crack was less successful in predicting this response overestimating the rotational stiffness of the specimen. This indicates that additional parameters are needed to predict the behaviour of the WFJ with fatigue crack such as material stiffness degradation or cohesive zone modelling. However, this FEM did give insight into the reduction of stresses at the crack tips with an increasing crack length.

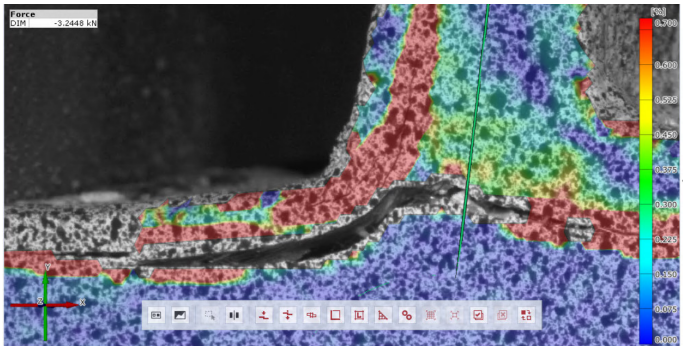

Figure 7.1: Mode 1 Delamination crack (Specimen T2)

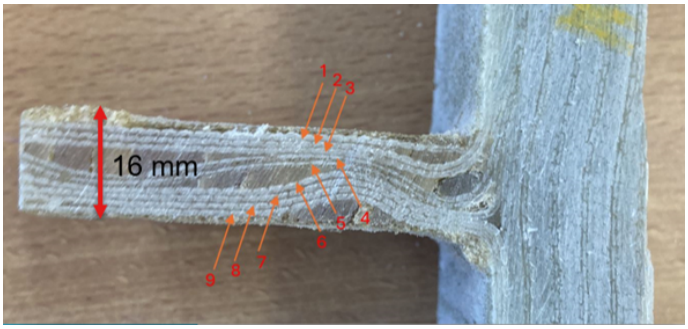

Figure 7.2: More fibre waviness with larger web thickness (Specimen B1) (9-double plies indicated)

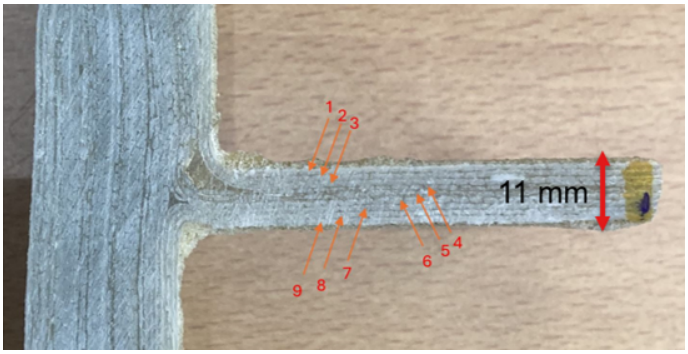

Figure 7.3: Less fibre waviness with smaller web thickness (Specimen B7) (9-double plies indicated)

7.3. SUMMARY OF WFJ RESPONSE

The force-displacement curves generated during the tests highlight three distinct regions in the response of the junctions: initial stiffness, crack initiation, and post-crack behaviour, see Figures 7.4 and 7.5. Initially, the junctions exhibit a linear elastic response, characterised by a constant rotational stiffness. As the load increased, a delamination crack initiated, leading to a significant drop in moment resistance and rotational stiffness. Despite this, the junctions retain some load-bearing capacity due to the formation of a post-crack mechanism that allows the structure to resist additional deformation through increased rotation. This behaviour indicates that while the junctions are prone to initial cracking, they can still support some load even after the initial delamination occurs.

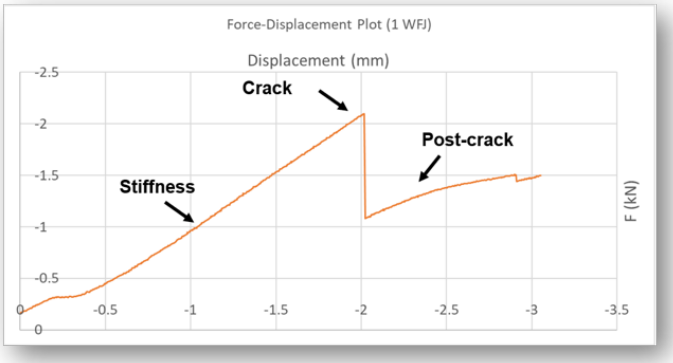

Figure 7.4: Web-to-Flange Junction Force-Displacement Plot and response regions

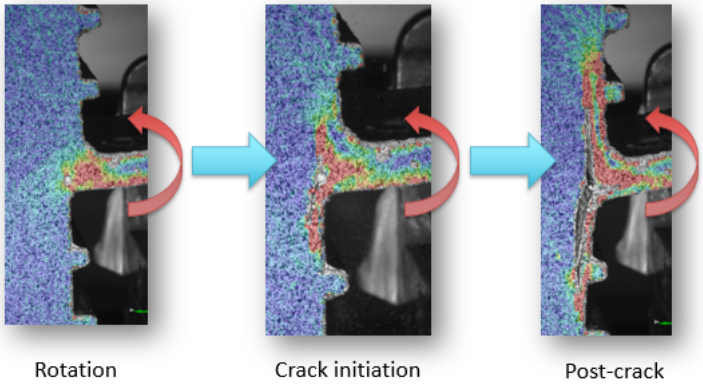

Figure 7.5: Web-to-Flange Junction Response to bending of the web

7.4. RECOMMENDATIONS FOR DESIGN AND MANUFACTURING

The future perspective of this research emphasises addressing the dominant failure mode identified, which is delamination of the web-to-flange junctions (WFJs). To enhance the design and predictability of WFJs, it is recommended that equations to calculate out-of-plane (OOP) stress in curved beams be incorporated into the Eurocode (EC) along with delamination S-N curves. This integration will enable designers to better predict the fatigue performance of WFJs with reduced reliance on extensive testing. Additionally, improving production processes to minimise imperfections such as waviness and variations in web thickness will likely increase the predictability of WFJ behaviour.

7.5. RECOMMENDATIONS FOR FUTURE RESEARCH

Given the damage-tolerant nature of WFJs observed during testing, a damage-tolerant design approach should be considered. This will require further research into crack growth behaviour and the acceptable reduction in rotational stiffness. There are various methods to enhance delamination resistance in WFJs (Wang and Soutis, 2017, Burns et al., 2015), and future research could focus on exploring these techniques to improve the structural integrity and durability of GFRP sandwich panels.

BIBLIOGRAPHY

Allegri, G. (2019). A unified formulation for fatigue crack onset and growth via cohesive zone modelling. https://doi.org/10.13140/RG.2.2.13907.12328

American Association of State Highway and Transportation Officials. (2008). *Guide specifications for design of frp pedestrian bridges*. https://books.google.nl/books?id=nujkf647aTMC

Ascione, L., Caron, J.-F., Godonou, P., van IJselmuijden, K., Knippers, J., Mottram, T., Oppe, M., Sorensen, M., Taby, J., & Tromp, L. (2016). *Prospect for new guidance in the design of frp* (JRC report No. EUR 27666 EN). Publications Office of the European Union. Luxembourg, Publications Office of the European Union. https://doi.org/10.2788/22306

ASTM. (2004). *Standard test method for measuring the curved beam strength of a fiber-reinforced polymer-matrix composite*.

ASTM International. (2015). *Standard practice for statistical analysis of linear or linearized stress-life (S−N) and strain-life (ϵ−N) fatigue data*. https://standards.globalspec.com/std/14596503/e739

Bohm, G., Bonney, C., Dionisi, F., Farmer, N., Hardy, G., Henderson, J., Hobbs, M., Kansara, K., Kreysler, W., Martin, F., Royle, T., Tromp, E., & Wilson, H. (2023, January). *Structural use of fibre polymer composites*. The Institution of Structural Engineers.

Burns, L., Mouritz, A., Pook, D., & Feih, S. (2015). Bio-inspired hierarchical design of composite t-joints with improved structural properties. *Composites Part B: Engineering, 69*, 222–231. https://doi.org/https://doi.org/10.1016/j.compositesb.2014.09.041

Burns, L., Mouritz, A., Pook, D., & Feih, S. (2016). Strengthening of composite t-joints using novel ply design approaches. *Composites Part B: Engineering, 88*, 73–84. https://doi.org/https://doi.org/10.1016/j.compositesb.2015.10.032

CEN. (2005, May). *EN 1993-1-9:2005, eurocode 3: Design of steel structures - part 1-9: Fatigue*.

Cintra, G. G., Cardoso, D. C., Vieira, J. D., & Keller, T. (2021). Experimental investigation on the moment-rotation performance of pultruded frp web-flange junctions. *Composites Part B: Engineering, 222*, 109087. https://doi.org/https://doi.org/10.1016/j.compositesb.2021.109087

Coogler, K., Harries, K. A., Wan, B., Rizos, D. C., & Petrou, M. F. (2005). Critical evaluation of strain measurements in glass fiber-reinforced polymer bridge decks [Cited by: 24]. *Journal of Bridge Engineering, 10*(6), 704–712. https://doi.org/10.1061/(ASCE)1084-0702(2005)10:6(704)

CROW-CUR. (2019). *Aanbeveling 96:2019 vezelversterkte kunststoffen in bouwkundige en civiel-technische draagconstructies* (tech. rep.). CROW-CUR. Utrecht, Netherlands.

Engineer's Edge. (n.d.). *Curved circular beam stress calculator* [Accessed: April 10, 2024]. https://www.engineersedge.com/calculators/curved_circular_beam_stress_15734.htm

European Committee for Standardization. (2022). TS19101: Design of fibre-polymer composite structures. https://standards.cen.eu/

FiberCore Europe BV. (2007). Technical datasheet: Infracore inside.

Frans, P. (2012). Mesolevel modeling of failure in composite laminates: Constitutive, kinematic and algorithmic aspects. *Archives of Computational Methods in Engineering, 19*(3), 381–425. https://doi.org/10.1007/s11831-012-9076-y

Haghani, R., Al-Emrani, M., & Heshmati, M. (2012). Fatigue-prone details in steel bridges. *Buildings, 2*, 456–476. https://doi.org/10.3390/buildings2040456

Hindawi. (2019). Table 1: Summary of results obtained from various studies of mab production in different host cell lines. [[Online; accessed April 11, 2024]].

Karpenko, O., Peeters, T., Gommers, E., White, T., Tromp, L., & Pavlović, M. (2024). A study on fatigue resistance and structural integrity in web-core composite bridge deck panels. *21st European Conference on Composite Materials (ECCM21)*. https://webofproceedings.org/proceedings_series/ACE/ICCEME%202019/ICCEME19004.pdf

Kedward, K., Wilson, R., & McLean, S. (1989). Flexure of simply curved composite shapes. *Composites, 20*(6), 527–536. https://doi.org/https://doi.org/10.1016/0010-4361(89)90911-7

Lekhnitskii, S. G., Tsai, S., & Chéron, T. (1968). *Anisotropic plates* (Vol. 534). Gordon; Breach New York.

Mandell, J. F., Samborsky, D. D., Wang, L., & Wahl, N. K. (2003). New Fatigue Data for Wind Turbine Blade Materials. *Journal of Solar Energy Engineering, 125*(4), 506–514. https://doi.org/10.1115/1.1624089

Mottram, J. T., & Henderson, J. (Eds.). (2018). *Fibre-reinforced polymer bridges – guidance for designers*. Composites UK.

Nen-en 1990:2002+a1:2019 eurocode - grondslagen van het constructief ontwerp. (2002).

Onderzoeksgroep Schoonmeersen. (2020a). *Ontwerpmethodes en softwarematige analysetechnieken / design methods and software analysis techniques* (tech. rep.). Universiteit Gent.

Onderzoeksgroep Schoonmeersen. (2020b). *Richtlijnen en normen: Tetra project c-bridge / guidelines and standards: Tetra project c-bridge* (tech. rep.). Universiteit Gent.

Poulton, M., Sebastian, W., & Mottram, J. (2024). Dic study of strain concentrations and damage within web-flange junctions of pultruded gfrp bridge decking. *Composites Part A: Applied Science and Manufacturing, 179*, 108011. https://doi.org/https://doi.org/10.1016/j.compositesa.2024.108011

Reis, E. M., & Rizkalla, S. H. (2008). Material characteristics of 3-d frp sandwich panels. *Construction and Building Materials, 22*(6), 1009–1018. https://doi.org/https://doi.org/10.1016/j.conbuildmat.2007.03.023

Rijkswaterstaat. (2022, November). *Prognoserapport 2022 vervanging en renovatie rijkswaterstaat* (Rapport) (PDF | 10,0 MB). https://www.rijksoverheid.nl/documenten/rapporten/2022/11/30/bijlage-8-prognoserapport-vervanging-en-renovatie-2022-rijkswaterstaat

Ronald Grefhorst, M. (2020, December). *Material properties: Characteristic values* (Technical Report No. Version 1.3) (Document status: Final). FiberCore Europe BV.

Sebastian, W. (2018). Fibre waviness in pultruded bridge deck profiles: Geometric characterisation and consequences on ultimate behaviour. *Composites Part B: Engineering, 146*, 270–280. https://doi.org/https://doi.org/10.1016/j.compositesb.2018.03.042

Sebastian, W., Ralph, M., Poulton, M., & Goacher, J. (2017). Lab and field studies into effectiveness of flat steel plate – rubber pad systems as tyre substitutes for local loading of cellular gfrp bridge decking. *Composites Part B: Engineering, 125*, 100–122. https://doi.org/https://doi.org/10.1016/j.compositesb.2017.05.044

Shahverdi, M., Vassilopoulos, A., & Keller, T. (2011). A phenomenological analysis of mode i fracture of adhesively-bonded pultruded gfrp joints. *Engineering Fracture Mechanics - ENG FRACTURE MECH, 78*, 2161–2173. https://doi.org/10.1016/j.engfracmech.2011.04.007

Standards for Highways England. (2020). *CD 368: Design of Fibre Reinforced Polymer Bridges and Highway Structures* (Highway Structures & Bridges Design). Highways England.

Trask, R., Hallett, S., Helenon, F., & Wisnom, M. (2012). Influence of process induced defects on the failure of composite t-joint specimens. *Composites Part A: Applied Science and Manufacturing, 43*(4), 748–757. https://doi.org/https://doi.org/10.1016/j.compositesa.2011.12.021

Tromp, L. (2018). *Kansen voor vvk in de infrastructuur* (tech. rep.). Royal HaskoningDHV. Rotterdam.

van IJselmuijden, K., & Tromp, L. (2013, March). *Normen voor vezelversterkte kunststof (vvk)* [Presentation slides]. Royal HaskoningDHV, CUR Bouw & Infra, Stichting Koninklijk Nederlands Normalisatie Instituut (NEN). https://adoc.pub/normen-voor-vezelversterkte-kunststof-vvk.html

Vassilopoulos, A. P., & Keller, T. (2011). *Fatigue of fiber-reinforced composites* (1st ed.) [Hardcover ISBN: 978-1-84996-180-6, Softcover ISBN: 978-1-4471-2694-2, eBook ISBN: 978-1-84996-181-3]. Springer London. https://doi.org/10.1007/978-1-84996-181-3

Wang, Y., & Soutis, C. (2017). Fatigue behaviour of composite t-joints in wind turbine blade applications. *Applied Composite Materials, 24*(2), 461–475. https://doi.org/10.1007/s10443-016-9537-9

Yanes-Armas, S., de Castro, J., & Keller, T. (2016). Energy dissipation and recovery in web–flange junctions of pultruded gfrp decks. *Composite Structures, 148*, 168–180. https://doi.org/https://doi.org/10.1016/j.compstruct.2016.03.042

Zhang, C. (2018, November). *Reliability-based fatigue damage assessment and optimum maintenance strategy of offshore horizontal wind turbine blades* [Doctoral dissertation].

A

FRP Material Properties

3.4 Material properties

The ply properties used in the analysis are obtained via testing performed by Deon Research Center (DRC) for FiberCore Europe (FCE).

The test standards and the production process for the samples is detailed in “Material data-R2.0.3.docx”

			Direct measurements			After correction to design-Vf		
			E-glass/UP High Vf	E-glass/UP Low Vf	Carbon/UP High Vf	E-glass/UP High Vf	E-glass/UP Low Vf	Carbon/UP High Vf
Property	**Symbol**	**Unit**	**Char. Value**	**Char. Value**	**Char. Value**	**Char. Value**	**Char. Value**	**Char. Value**
Longitudional tensile modulus	ETx	GPa	47	25	119	42	22	109
Transverse tensile modulus	ETy	GPa	16,7	8,5	7,5	14,5	8,0	6,7
Longitudinal compressive modulus *1	ECx	GPa	(40)	(24)	(110)			
Transverse compressive modulus	ECy	GPa	15	11	22	13	10	20
Shear modulus	Gxy	GPa	4,8	3,7	6,7	4,2	3,5	6,1
Poisson ratio	vxy	-	0,27	0,27	0,28	0,27	0,27	0,28
Longitudinal tensile strength	σTx	MPa	948	382	1192	855	327	1084
Transverse tensile strength	σTy	MPa	59	24	12	59	24	12
Longitudinal compressive strength	σCx	MPa	439	479	554	395	410	503
Transverse compressive strength	σCy	MPa	138	130	52	138	130	52
Shear strength (0,2% offset)	τxy	MPa	39	32	44	39	32	44
Interlaminar shear strength	τxz	MPa	51	33	48	51	33	48
Allowable longitudinal tensile strain	εTx,max	%	2,01	1,50	1,00	2,01	1,50	1,00
Allowable transverse tensile strain	εTy,max	%	0,36	0,28	0,17	0,41	0,30	0,18
Allowable longitudinal compressive strain *2	εCx,max	%	0,93	1,89	0,46	0,93	1,89	0,46
Allowable transverse compressive strain *3	εCy,max	%	0,89	1,17	0,24	1,02	1,25	0,26
Allowable shear strain	γmax	%	0,81	0,87	0,65	0,93	0,92	0,72
Longitudinal linear coefficient of thermal expansion *4	αx	10^{-6} K^{-1}	8,57	13,60	0,61	9,22	15,45	0,85
Transverse linear coefficient of thermal expansion *4	αy	10^{-6} K^{-1}	31,38	48,31	30,97	35,77	59,56	35,16
Density *5	ρ	kg/m^3	2046	1641	1531	1962	1576	1500
Fiber volume fraction	Vf	%	60	32	55	54	27	50
Glass transition temperature (DMA, max tan delta)	Tg	°C	113	112	117			
Ply thickness 600gsm @ design Vf	t_p	mm				0,424	0,848	0,663

**1 Compressive moduli as measured in fibre direction is only reported for reference and may not be used for design.*

2 Determined as the ratio between longitudinal **compressive strength and longitudinal **tensile** modulus*

3 Determined as the ratio between transverse **compressive strength and transverse **compressive** modulus*

**4 Determined using Chamis' method at measured Vf resp. design Vf*

**5 Determined using Rule of Mixtures at measured Vf resp. design Vf, using supplier data*

Figure A.1: Material properties

Lay-up (option2) SELECTED

- **Proposal:**
  - Z-layers: 5-block overlap of 2x0/90 + 1x+/-45
  - 4-block overlap additional UD: 3x UD
  - Wrap core block: 3x+/-45

	Fibre-orientation (90degrees = span direction) *degrees*	Area weight *gsm*	Thickness *mm*	Direction-% %	*Comments*
Skin					
'Z'- shape:					
	0	1200	0,838	16,7%	
	90	1200	0,838	56,7%	
	+45	600	0,419	13,3%	
	-45	600	0,419	13,3%	
	subtotal	*3600*	*2,514*		
overlap: 5		*18000*	*12,570*		*...-block overlap for 'Z'*
Insert-UD's:					
	90	3600	2,514		*Not part of 'Z', added to top and bottom only*
	subtotal	*3600*	*2,514*		
overlap: 4		*14400*	*10,056*		*...-block overlap for UD*
From wrap:					
	+45	600	0,419		
	-45	600	0,419		
	subtotal	*1200*	*0,838*		
n: 3		*3600*	*2,514*		*...-times wrap*
Total		***36000***	***25,140***	***100,0%***	
Web					
From Z:	0	1200	1,676	11,1%	
"	90	1200	1,676	11,1%	
"	+45	600	0,838	38,9%	
"	-45	600	0,838	38,9%	
From wrap:	+45	3600	5,028		*Wraps from adjacent blocks on left + right*
"	-45	3600	5,028		*Wraps from adjacent blocks on left + right*
Total		***10800***	***15,084***	***100,0%***	*From: wrap + Z + wrap*

Figure A.2: Selected lay-up

B

WFJ SPECIMEN MEASUREMENTS

Number	thickness web (tw)1	thickness web (tw)2	thickness web (tw)3	thickness web (tw)avg	thickness skin (ts)1	thickness skin (ts)2	thickness skin (ts)3	thickness skin (ts)4	thickness skin (ts)avg	height T-joint (ht)	height skin (hs)	width (w)	distance top of skin to top of web (hw1)	distance bottom of skin to bottom of web (hw2)	length web (lw)	volume (mm^3)	weight (gram)	density (gram/m m3)	density (kg/m3)
B1	16.3	16.0	15.9	16.06667	27	27	27	27	27	100	144	78	69	58.93333	73	394747.6	745	0.001887	1887.282
B2	17.0	16.5	16.6	16.7	22	21	21	20	21	98	141	81	66	58.3	77	343998.9	621.2	0.001806	1805.82
B3	11.4	11.2	11.8	11.46667	25	26	25	25	25.25	98	139	77	68	59.53333	72.75	334484.2		0	0
B4	10.2	10.6	10.8	10.53333	25	24	25	25	24.75	101	141	79	64	66.46667	76.25	339140.4		0	0
B5	11.3	11.7	12.2	11.73333	24	24	24	24	24	99	138	78	62	64.26667	75	326976		0	0
B6	11.5	11.9	12.8	12.06667	21	22	21	20	21	101	141	79	70	58.93333	80	310180.3		0	0
B7	10.9	10.8	10.8	10.83333	25	29	24	25	25.75	101	148	80	62	75.16667	75.25	370096.7		0	0
B8	11.9	12.3	11.8	12	25	28	27	27	26.75	103	142	79	65	65	76.25	372366.5		0	0
B9	10.5	10.2	10.5	10.4	24	25	21	22	23	100	139	82	62	66.6	77	327819.6		0	0
B10	12.5	12.8	14.4	13.23333	27	29	27	27	27.5	100	147	78	68	65.76667	72.5	390149.5		0	0
B11	13.0	13.0	14.0	13.33333	25	25	24	25	24.75	101	145	80	70	61.66667	76.25	368433.3		0	0
B12	11.4	11.4	11.0	11.26667	27	27	23	24	25.25	101	116	81	37	67.73333	75.75	306378.5		0	0
T1	17.8	18.0	17.6	17.8	29	30	27	26	28	96	145	81	62	65.2	68	426902.4		0	0
T2	14.5	13.7	14.0	14.06667	30	32	27	29	29.5	96	146	81	64	67.93333	66.5	424637.1		0	0
T3	15.1	15.7	15.3	15.36667	27	27	26	26	26.5	98	150	76	67	67.63333	71.5	385602.5		0	0
T4	11.0	11.0	11.0	11	27	29	26	27	27.25	97	142	79	65	66	69.75	366303.3		0	0
T5	13.6	13.5	13.1	13.4	27	29	26	26	27	98	141	76	62	65.6	71	361638.4		0	0
T6	13.0	11.6	12.8	12.46667	27	29	27	27	27.5	97	141	77	63	65.53333	69.5	365282.9		0	0
T7	16.5	16.2	16.2	16.3	27	28	26	27	27	96	145	78	62	66.7	69	393096.6	720	0.001832	1831.611
T8	12.0	12.0	12.0	12	28	29	26	27	27.5	98	143	74	65	66	70.5	353609		0	0
T9	11.0	11.0	11.0	11	28	32	28	28	29	98	135	82	64	60	69	383268		0	0
T10	12.0	11.0	12.0	11.66667	28	30	26	27	27.75	98	140	78	65	63.33333	70.25	366957.5		0	0
T11	13.0	13.1	14.1	13.4	27	29	27	27	27.5	96	139	78	65	60.6	68.5	369751.2		0	0
T12	10.0	10.8	10.8	10.53333	31	29	27	28	28.75	97	109	82	69	29.46667	68.25	315917.3		0	0
Average	12.80833	12.75	13.02083	12.85972	26.375	27.5	25.33333	25.66667	26.21875	98.66667	139.875	78.91667	64	63.01528	72.44792				
StDev				2.159844					2.249774	1.99274	9.161889				3.654939				

Imperfections based on visual inspection			1=bad 2=ok 3=good		
T1	1	huge resin rich area on Z side, layer appears to be folded and makes a loop. Surface coating	B1	1	lots of wavyness in web, therefore very thick web. Vf is web very low
T2	2	wavyness at junction, web quite thick	B2	1	lots of wavyness in web, big pockets of resin rich areas at beginning of junction
T3	2	lots of wavyness at Z side	B3	3	very neat junction, resin rich area small. Very slightly wavy at junction
T4	3	neat junction, slightly larger resin rich area on one side	B4	3	slight wavyness at junction, resin rich area very small
T5	1	lots of wavyness and large resin rich area at Z side	B5	3	very neat junction, resin rich area small
T6	3	neat junction, slight gap in resin rich area	B6	3	neat, two small resin rich areas on one side
T7	2	lots of wavyness and resin rich areas on Z side, web thickness very large. Large resin rich area outside of fiber layers	B7	2	neat, larger resin rich area on Z-side
T8	3	neat junction, resin rich area slightly larger. Slight wavyness at Z side	B8	3	slight wavyness at junction, resin rich area very small
T9	3	very neat junction, with surface coating on flange	B9	3	very neat, slight wavyness at one side
T10	3	neat junction with hole in resin rich area. Small resin rich area on Z side	B10	2	on one side more wavyness and multiple resin rich areas
T11	2	wavyness at junction, and large resin rich area on Z side	B11	2	two resin rich areas in junction, more wavyness in web
T12	2	large gap on Z side of junction, surface coating on flange	B12	2	neat junction, but resin rich area quite large. Flange on Z side very small

C

CALIBRATION REPORT

Current Calibration Info

General

Calibration date	29-1-2024 14:37:42

Calibrated sensor

Sensor name	ARAMIS Adjustable Base
Measuring volume	Adjustable measuring volume
Camera support	Adjustable 500
Working distance	767 mm
Camera angle	25°
Camera distance	300 mm
Serial number	no identifier

Calibration object

Object type	Panel (Triple Scan)
Name	CP40/170/43880
Certification date	19-8-2021
Certification ID	100999/D-K-21312-01-00/2021-08
Calibration points	3657 points
Certified lengths	243.256 / 243.257 mm
Certification temperature	20.0 °C
Expansion coefficient	$6.94 \times 10^{-6}\ K^{-1}$
Calibration temperature	21.3 °C

Calibration settings

Camera lenses	50.00 mm
Snap mode	Single snap
Max. ellipse residual	0.088 (gray value adjustment)

Calibration Result

Calibration deviation	0.064 Pixels
Calibration deviation (check)	OK (limit value: 0.100 Pixels)
Camera angle	24.6°
Height variance	119 mm
Measuring volume	195 / 140 / 125 mm

D

STRESS IN CURVED BEAM CALCULATION

Tangential and Radial stress calculation WFJ T10

$b := 78\ mm$ $R_i := 5.0536\ mm$ Inner radius non-Z side

$R_{i.z} := 7.7808\ mm$ Inner radius Z-side

$r := 8.1479\ mm$ Location where crack initiated non Z-side

$r_z := 19.4508\ mm$ crack location Z-side, this case outer radius because
$t_w := 11.67 \cdot mm$ crack is outside outer radius

$t_{w.GOM} := 9.7780\ mm$

$t_w := t_w = 11.67\ mm$

$R_o := R_i + t_w = 16.724\ mm$ Outer radius assumed to be sum of inner radius + thickness.

$R_{o.z} := R_{i.z} + t_w = 19.451\ mm$

$t := R_o - R_i = 11.67\ mm$ Thickness deviates from 15mm nominal thickness

$F := 2.097\ kN$ $a_{br} := 62\ mm - R_i = 56.946\ mm$ arm before radius

$M := F \cdot a_{br} = 0.119\ kN \cdot m$

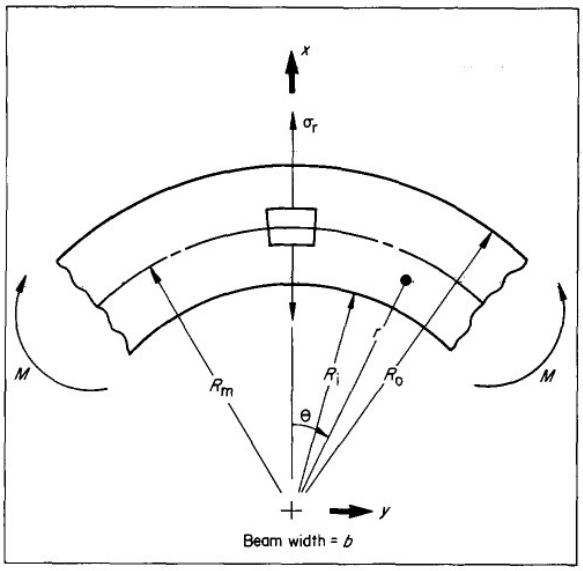

Fig. 6 Uniform moment loading on curved beam

$c := \frac{R_i}{R_o} = 0.302$ constant value 'c' needed for equation

$k := \left(\frac{1}{0.95}\right)^{\frac{1}{2}} = 1.026$ constant value 'k' needed for equation

$$g := \frac{1-c^2}{2} - \frac{k}{k+1} \cdot \frac{\left(1-c^{k+1}\right)^2}{1-c^{2k}} + \frac{k \cdot c^2}{k-1} \cdot \frac{\left(1-c^{k-1}\right)^2}{1-c^{2k}} = -0.002$$

constant value 'g' needed for equation

$$r_{max.eq} := \left(\frac{(k+1) \cdot \left(1-c^{(k-1)}\right) \cdot c \cdot \left(R_i \cdot R_o\right)^k}{(k-1) \cdot \left(1-c^{(k+1)}\right)} \right)^{\frac{1}{2k}} = 8.203 \ mm$$ Theoretical crack position

$r = 8.148 \ mm$ Actual crack position

Stress a theoretical crack position, open side

radial stress

$$\sigma_r := -\frac{M}{R_o^{\,2} \cdot b \cdot g} \cdot \left(1 - \frac{1 - c^{k+1}}{1 - c^{2k}} \cdot \left(\frac{r}{R_o} \right)^{k-1} - \frac{1 - c^{k-1}}{1 - c^{2k}} \, c^{k+1} \cdot \left(\frac{R_o}{r} \right)^{k+1} \right) = 21.861 \ \textbf{\textit{MPa}}$$

tangential stress

$$\sigma_\theta := -\frac{M}{R_o^{\,2} \cdot b \cdot g} \cdot \left(1 - \frac{1 - c^{k+1}}{1 - c^{2k}} \cdot k \cdot \left(\frac{r}{R_o} \right)^{k-1} + \frac{1 - c^{k-1}}{1 - c^{2k}} \, k \cdot c^{k+1} \cdot \left(\frac{R_o}{r} \right)^{k+1} \right) = 22.748 \ \textbf{\textit{MPa}}$$

End load on a curved beam, (next page)

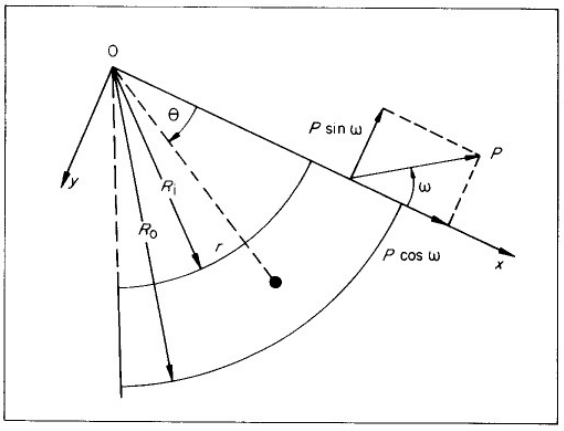

Fig. 8 Arbitrary end load on curved beam

End load on curved beam

$E_\theta := 13601.5\ \textbf{MPa}$ Values from FEM

$E_{r.FEM} := 19406.89\ \textbf{MPa}$ $E_r := 0.95 \cdot E_\theta = (1.292 \cdot 10^4)\ \textbf{MPa}$ $\frac{E_\theta}{E_r} = 1.053$

$v_{r\theta} := 0.24$

$G_{r\theta} := 3516.921\ \textbf{MPa} = (3.517 \cdot 10^3)\ \textbf{MPa}$

$$\beta := \left(1 + \frac{E_\theta}{E_r}\left(1 - 2 \cdot v_{r\theta}\right) + \frac{E_\theta}{G_{r\theta}}\right)^{0.5} = 2.327$$

$$g_1 := \frac{2}{\beta}\left(1 - c^\beta\right) + \left(1 + c^\beta\right) \cdot \ln(c) = -0.464$$

$$r_{max.eq} := \left(\frac{R_o{}^\beta}{2\left(1-\beta\right)}\left(1 + c^\beta - \left(\left(1 + c^\beta\right)^2 + 4 \cdot c^\beta \cdot \left(\beta^2 - 1\right)\right)^{\frac{1}{2}}\right)\right)^{\frac{1}{\beta}} = 7.63\ \textbf{mm}$$

$P := F = (2.097 \cdot 10^3)\ \textbf{N}$

$\theta := \frac{\pi}{4}$ location of stress, is 45deg for open side $\omega := 0$ angel of force is 0 deg

$$\sigma_{r.P} := \frac{P}{R_o \cdot b \cdot g_1}\frac{R_o}{r}\left(\left(\frac{r}{R_o}\right)^\beta + c^\beta\left(\frac{R_o}{r}\right)^\beta - 1 - c^\beta\right) \cdot \sin(\theta + \omega) = 2.74\ \textbf{MPa}$$

$$\sigma_{\theta.P} := \frac{P}{R_o \cdot b \cdot g_1}\frac{R_o}{r}\left((1+\beta) \cdot \left(\frac{r}{R_o}\right)^\beta + (1-\beta) \cdot c^\beta\left(\frac{R_o}{r}\right)^\beta - 1 - c^\beta\right) \cdot \sin(\theta + \omega) = 4.394\ \textbf{MPa}$$

$$\tau_{r\theta} := \frac{-P}{R_o \cdot b \cdot g_1}\frac{R_o}{r}\left(\left(\frac{r}{R_o}\right)^\beta + c^\beta\left(\frac{R_o}{r}\right)^\beta - 1 - c^\beta\right) \cdot \cos(\theta + \omega) = -2.74\ \textbf{MPa}$$

$\sigma_{r.plus} := \sigma_r + \sigma_{r.P} = 24.601\ \textbf{MPa}$ $\sigma_{\theta.plus} := \sigma_\theta + \sigma_{\theta.P} = 27.141\ \textbf{MPa}$

$\tau_{r\theta.plus} := \tau_{r\theta} = -2.74\ \textbf{MPa}$

Stress at theorectical crack position, closed side

$R_i := R_{i.z} = 7.781\ mm$ $R_o := R_{o.z} = 19.451\ mm$

$c := \frac{R_i}{R_o} = 0.4$ constant value 'c' needed for equation

$g := \frac{1-c^2}{2} - \frac{k}{k+1} \cdot \frac{\left(1-c^{k+1}\right)^2}{1-c^{2k}} + \frac{k \cdot c^2}{k-1} \cdot \frac{\left(1-c^{k-1}\right)^2}{1-c^{2k}} = -0.001$

$k = 1.026$

$r_{max.eq} := \left(\frac{(k+1) \cdot \left(1-c^{(k-1)}\right) \cdot c \cdot \left(R_i \cdot R_o\right)^k}{(k-1) \cdot \left(1-c^{(k+1)}\right)} \right)^{\frac{1}{2k}} = 11.493\ mm$

$r := r_z = 19.451\ mm$

Moments are reversed for closed side, see diagram paper

radial stress

$\sigma_r := \frac{M}{{R_o}^2 \cdot b \cdot g} \cdot \left(1 - \frac{1-c^{k+1}}{1-c^{2k}} \cdot \left(\frac{r}{R_o}\right)^{k-1} - \frac{1-c^{k-1}}{1-c^{2k}}\, c^{k+1} \cdot \left(\frac{R_o}{r}\right)^{k+1} \right) = \left(2.166 \cdot 10^{-13}\right)\ MPa$

tangential stress

$\sigma_\theta := \frac{M}{{R_o}^2 \cdot b \cdot g} \cdot \left(1 - \frac{1-c^{k+1}}{1-c^{2k}} \cdot k \cdot \left(\frac{r}{R_o}\right)^{k-1} + \frac{1-c^{k-1}}{1-c^{2k}}\, k \cdot c^{k+1} \cdot \left(\frac{R_o}{r}\right)^{k+1} \right) = 52.661\ MPa$

End load on curved beam

$g_1 := \frac{2}{\beta} \left(1-c^\beta\right) + \left(1+c^\beta\right) \cdot \ln(c) = -0.267$

$r_{max.eq} := \left(\frac{{R_o}^\beta}{2\left(1-\beta\right)} \left(1 + c^\beta - \left(\left(1+c^\beta\right)^2 + 4 \cdot c^\beta \cdot \left(\beta^2 - 1\right) \right)^{\frac{1}{2}} \right) \right)^{\frac{1}{\beta}} = 11.04\ mm$

$P = 2.097\ kN$ $r = 19.451\ mm$

$\theta := 30 \cdot \frac{\pi}{180} = 0.524$ location of stress, is 30 deg for closed side

$\omega := 0$ direction of loading force

Force dicrection is reversed for closed side, see diagram paper

$$\sigma_{r.P} := -\frac{P}{R_o \cdot b \cdot g_1} \frac{R_o}{r} \left(\left(\frac{r}{R_o} \right)^{\beta} + c^{\beta} \left(\frac{R_o}{r} \right)^{\beta} - 1 - c^{\beta} \right) \cdot \sin(\theta + \omega) = -2.153 \cdot 10^{-16} \ \textit{MPa}$$

$$\sigma_{\theta.P} := -\frac{P}{R_o \cdot b \cdot g_1} \frac{R_o}{r} \left((1+\beta) \cdot \left(\frac{r}{R_o} \right)^{\beta} + (1-\beta) \cdot c^{\beta} \left(\frac{R_o}{r} \right)^{\beta} - 1 - c^{\beta} \right) \cdot \sin(\theta + \omega) = 5.302 \ \textit{MPa}$$

$$\tau_{r\theta} := \frac{P}{R_o \cdot b \cdot g_1} \frac{R_o}{r} \left(\left(\frac{r}{R_o} \right)^{\beta} + c^{\beta} \left(\frac{R_o}{r} \right)^{\beta} - 1 - c^{\beta} \right) \cdot \cos(\theta + \omega) = \left(3.728 \cdot 10^{-16} \right) \ \textit{MPa}$$

$\sigma_{r.cl} := \sigma_r + \sigma_{r.P} = \left(2.164 \cdot 10^{-13} \right) \ \textit{MPa}$ $\sigma_{\theta.cl} := \sigma_{\theta} + \sigma_{\theta.P} = 57.963 \ \textit{MPa}$

$\tau_{r\theta.cl} := \tau_{r\theta} = \left(3.728 \cdot 10^{-16} \right) \ \textit{MPa}$

Transform from 60deg to 45deg

$\theta_{deg} := (45 - 60) = -15$ $\theta := \theta_{deg} \cdot \frac{\pi}{180} = -0.262$

$$\sigma_{r.cl.rot} := \frac{\sigma_{r.cl} + \sigma_{\theta.cl}}{2} + \frac{\sigma_{r.cl} - \sigma_{\theta.cl}}{2} \cdot \cos(2 \cdot \theta) + \tau_{r\theta.cl} \cdot \sin(2 \cdot \theta) = 3.883 \ \textit{MPa}$$

$$\sigma_{\theta.cl.rot} := \frac{\sigma_{r.cl} + \sigma_{\theta.cl}}{2} - \frac{\sigma_{r.cl} - \sigma_{\theta.cl}}{2} \cdot \cos(2 \cdot \theta) + \tau_{r\theta.cl} \cdot \sin(2 \cdot \theta) = 54.08 \ \textit{MPa}$$

$$\tau_{r\theta.cl.rot} := -\frac{\sigma_{r.cl} - \sigma_{\theta.cl}}{2} \cdot \sin(2 \cdot \theta) + \tau_{r\theta.cl} \cdot \cos(2 \cdot \theta) = -14.491 \ \textit{MPa}$$

Sum the stresses:

$\sigma_r := \sigma_{r.plus} + \sigma_{r.cl.rot} = 28.484\ \textbf{MPa}$ Radial stress

$\sigma_\theta := \sigma_{\theta.plus} + \sigma_{\theta.cl.rot} = 81.222\ \textbf{MPa}$

$\tau_{xy} := \tau_{r\theta.plus} + \tau_{r\theta.cl.rot} = -17.23\ \textbf{MPa}$

Principal stresses

$$\sigma_1 := \left(\frac{\sigma_r + \sigma_\theta}{2}\right) + \sqrt[2]{\left(\frac{\sigma_r - \sigma_\theta}{2}\right)^2 + \tau_{xy}{}^2} = 86.352\ \textbf{MPa}$$

$$\sigma_2 := \left(\frac{\sigma_r + \sigma_\theta}{2}\right) - \sqrt[2]{\left(\frac{\sigma_r - \sigma_\theta}{2}\right)^2 + \tau_{xy}{}^2} = 23.353\ \textbf{MPa}$$

$$\tau_{max} := \frac{\sigma_1 - \sigma_2}{2} = 31.499\ \textbf{MPa}$$

$$\theta_p := \frac{1}{2} \cdot \tan\left(\frac{2 \cdot \tau_{xy}}{\sigma_1 - \sigma_2}\right)^{-1} = -0.821$$ Angle of principal plane (rad)

$$\theta_p \cdot \frac{180}{\pi} = -47.042$$ Angle of principal plane (degrees)

Tangential and Radial stress calculation WFJ T3

$b := 76\ mm$ $R_i := 2.8851\ mm$ Inner radius non-Z side

$R_{i.z} := 8.2058\ mm$ Inner radius Z-side

$r := 5.3703\ mm$ Location where crack initiated non Z-side

$r_z := 20.5706\ mm$ crack location Z-side

$t_w := 15.37 \cdot mm$ $t_{w.GOM} := 13.8954\ mm$

$t_w := t_w = 15.37\ mm$

$R_o := R_i + t_w = 18.255\ mm$ Outer radius assumed to be sum of inner radius + thickness.

$R_{o.z} := R_{i.z} + t_w = 23.576\ mm$

$t := R_o - R_i = 15.37\ mm$ Thickness deviates from 15mm nominal thickness

$F := 2.06707\ kN$ $a_{br} := 60\ mm - R_i = 57.115\ mm$ arm before radius

$M := F \cdot a_{br} = 0.118\ kN \cdot m$

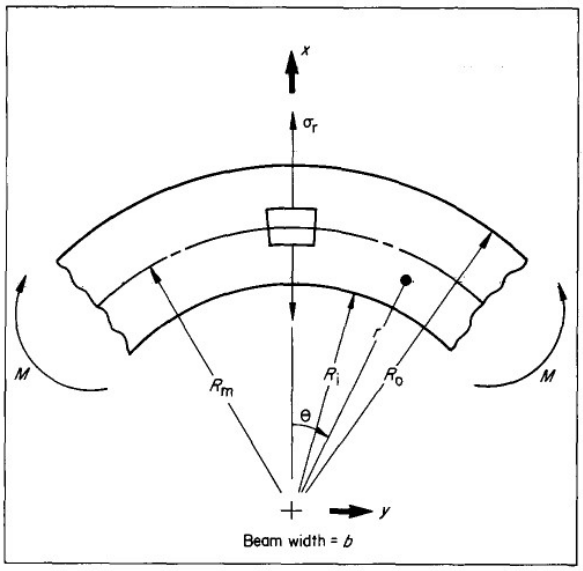

Fig. 6 Uniform moment loading on curved beam

$c := \frac{R_i}{R_o} = 0.158$ constant value 'c' needed for equation

$k := \left(\frac{1}{0.95}\right)^{\frac{1}{2}} = 1.026$ constant value 'k' needed for equation

$$g := \frac{1-c^2}{2} - \frac{k}{k+1} \cdot \frac{\left(1-c^{k+1}\right)^2}{1-c^{2k}} + \frac{k \cdot c^2}{k-1} \cdot \frac{\left(1-c^{k-1}\right)^2}{1-c^{2k}} = -0.004$$

constant value 'g' needed for equation

$$r_{max.eq} := \left(\frac{(k+1) \cdot \left(1-c^{(k-1)}\right) \cdot c \cdot \left(R_i \cdot R_o\right)^k}{(k-1) \cdot \left(1-c^{(k+1)}\right)} \right)^{\frac{1}{2k}} = 5.616 \ mm$$ Theoretical crack position

$r = 5.37 \ mm$ Actual crack position

Stress a theoretical crack position, open side

radial stress

$$\sigma_r := -\frac{M}{R_o^{\,2} \cdot b \cdot g} \cdot \left(1 - \frac{1 - c^{k+1}}{1 - c^{2k}} \cdot \left(\frac{r}{R_o} \right)^{k-1} - \frac{1 - c^{k-1}}{1 - c^{2k}} \, c^{k+1} \cdot \left(\frac{R_o}{r} \right)^{k+1} \right) = 21.528 \ \textbf{\textit{MPa}}$$

tangential stress

$$\sigma_\theta := -\frac{M}{R_o^{\,2} \cdot b \cdot g} \cdot \left(1 - \frac{1 - c^{k+1}}{1 - c^{2k}} \cdot k \cdot \left(\frac{r}{R_o} \right)^{k-1} + \frac{1 - c^{k-1}}{1 - c^{2k}} \, k \cdot c^{k+1} \cdot \left(\frac{R_o}{r} \right)^{k+1} \right) = 24.293 \ \textbf{\textit{MPa}}$$

End load on a curved beam, (next page)

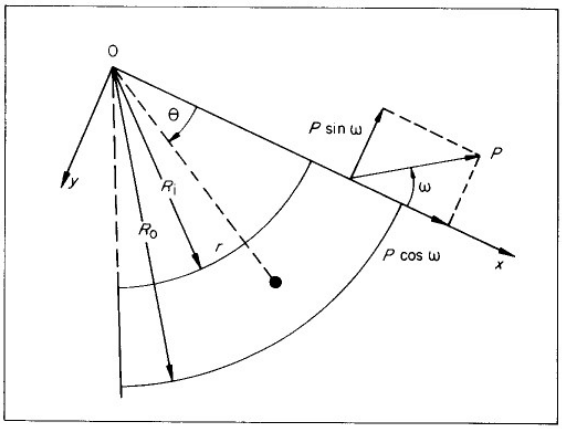

Fig. 8 Arbitrary end load on curved beam

End load on curved beam

$E_\theta := 13601.5\ \textit{MPa}$ Values from FEM

$E_{r.FEM} := 19406.89\ \textit{MPa}$ $E_r := 0.95 \cdot E_\theta = (1.292 \cdot 10^4)\ \textit{MPa}$ $\frac{E_\theta}{E_r} = 1.053$

$v_{r\theta} := 0.24$

$G_{r\theta} := 3516.921\ \textit{MPa} = (3.517 \cdot 10^3)\ \textit{MPa}$

$$\beta := \left(1 + \frac{E_\theta}{E_r}\left(1 - 2 \cdot v_{r\theta}\right) + \frac{E_\theta}{G_{r\theta}}\right)^{0.5} = 2.327$$

$$g_1 := \frac{2}{\beta}\left(1 - c^\beta\right) + \left(1 + c^\beta\right) \cdot \ln(c) = -1.022$$

$$r_{max.eq} := \left(\frac{R_o{}^\beta}{2\left(1-\beta\right)}\left(1 + c^\beta - \left(\left(1 + c^\beta\right)^2 + 4 \cdot c^\beta \cdot \left(\beta^2 - 1\right)\right)^{\frac{1}{2}}\right)\right)^{\frac{1}{\beta}} = 4.698\ \textit{mm}$$

$P := F = (2.067 \cdot 10^3)\ \textit{N}$

$\theta := \frac{\pi}{4}$ location of stress, is 45deg for open side $\omega := 0$ angel of force is 0 deg

$$\sigma_{r.P} := \frac{P}{R_o \cdot b \cdot g_1}\frac{R_o}{r}\left(\left(\frac{r}{R_o}\right)^\beta + c^\beta\left(\frac{R_o}{r}\right)^\beta - 1 - c^\beta\right) \cdot \sin(\theta + \omega) = 2.522\ \textit{MPa}$$

$$\sigma_{\theta.P} := \frac{P}{R_o \cdot b \cdot g_1}\frac{R_o}{r}\left(\left(1+\beta\right) \cdot \left(\frac{r}{R_o}\right)^\beta + \left(1-\beta\right) \cdot c^\beta\left(\frac{R_o}{r}\right)^\beta - 1 - c^\beta\right) \cdot \sin(\theta + \omega) = 3.97\ \textit{MPa}$$

$$\tau_{r\theta} := \frac{-P}{R_o \cdot b \cdot g_1}\frac{R_o}{r}\left(\left(\frac{r}{R_o}\right)^\beta + c^\beta\left(\frac{R_o}{r}\right)^\beta - 1 - c^\beta\right) \cdot \cos(\theta + \omega) = -2.522\ \textit{MPa}$$

$\sigma_{r.plus} := \sigma_r + \sigma_{r.P} = 24.05\ \textit{MPa}$ $\sigma_{\theta.plus} := \sigma_\theta + \sigma_{\theta.P} = 28.263\ \textit{MPa}$

$\tau_{r\theta.plus} := \tau_{r\theta} = -2.522\ \textit{MPa}$

Stress at theorectical crack position, closed side

$R_i := R_{i.z} = 8.206\ mm$ $R_o := R_{o.z} = 23.576\ mm$

$c := \frac{R_i}{R_o} = 0.348$ constant value 'c' needed for equation

$g := \frac{1-c^2}{2} - \frac{k}{k+1} \cdot \frac{\left(1-c^{k+1}\right)^2}{1-c^{2k}} + \frac{k \cdot c^2}{k-1} \cdot \frac{\left(1-c^{k-1}\right)^2}{1-c^{2k}} = -0.002$

$k = 1.026$

$r_{max.eq} := \left(\frac{(k+1) \cdot \left(1-c^{(k-1)}\right) \cdot c \cdot \left(R_i \cdot R_o\right)^k}{(k-1) \cdot \left(1-c^{(k+1)}\right)} \right)^{\frac{1}{2k}} = 12.718\ mm$

$r := r_z = 20.571\ mm$

Moments are reversed for closed side, see diagram paper

radial stress

$\sigma_r := \frac{M}{{R_o}^2 \cdot b \cdot g} \cdot \left(1 - \frac{1-c^{k+1}}{1-c^{2k}} \cdot \left(\frac{r}{R_o}\right)^{k-1} - \frac{1-c^{k-1}}{1-c^{2k}}\, c^{k+1} \cdot \left(\frac{R_o}{r}\right)^{k+1} \right) = -3.835\ MPa$

tangential stress

$\sigma_\theta := \frac{M}{{R_o}^2 \cdot b \cdot g} \cdot \left(1 - \frac{1-c^{k+1}}{1-c^{2k}} \cdot k \cdot \left(\frac{r}{R_o}\right)^{k-1} + \frac{1-c^{k-1}}{1-c^{2k}}\, k \cdot c^{k+1} \cdot \left(\frac{R_o}{r}\right)^{k+1} \right) = 22.261\ MPa$

End load on curved beam

$g_1 := \frac{2}{\beta} \left(1-c^\beta\right) + \left(1+c^\beta\right) \cdot \ln(c) = -0.36$

$r_{max.eq} := \left(\frac{{R_o}^\beta}{2\left(1-\beta\right)} \left(1 + c^\beta - \left(\left(1+c^\beta\right)^2 + 4 \cdot c^\beta \cdot \left(\beta^2 - 1\right) \right)^{\frac{1}{2}} \right) \right)^{\frac{1}{\beta}} = 12.039\ mm$

$P = 2.067\ kN$ $r = 20.571\ mm$

$\theta := 30 \cdot \frac{\pi}{180} = 0.524$ location of stress, is 30 deg for closed side

$\omega := 0$ direction of loading force

Force dicrection is reversed for closed side, see diagram paper

$$\sigma_{r.P} := -\frac{P}{R_o \cdot b \cdot g_1} \frac{R_o}{r} \left(\left(\frac{r}{R_o} \right)^{\beta} + c^{\beta} \left(\frac{R_o}{r} \right)^{\beta} - 1 - c^{\beta} \right) \cdot \sin(\theta + \omega) = -0.44 \ \textbf{MPa}$$

$$\sigma_{\theta.P} := -\frac{P}{R_o \cdot b \cdot g_1} \frac{R_o}{r} \left((1+\beta) \cdot \left(\frac{r}{R_o} \right)^{\beta} + (1-\beta) \cdot c^{\beta} \left(\frac{R_o}{r} \right)^{\beta} - 1 - c^{\beta} \right) \cdot \sin(\theta + \omega) = 2.166 \ \textbf{MPa}$$

$$\tau_{r\theta} := \frac{P}{R_o \cdot b \cdot g_1} \frac{R_o}{r} \left(\left(\frac{r}{R_o} \right)^{\beta} + c^{\beta} \left(\frac{R_o}{r} \right)^{\beta} - 1 - c^{\beta} \right) \cdot \cos(\theta + \omega) = 0.763 \ \textbf{MPa}$$

$\sigma_{r.cl} := \sigma_r + \sigma_{r.P} = -4.276 \ \textbf{MPa}$ $\sigma_{\theta.cl} := \sigma_{\theta} + \sigma_{\theta.P} = 24.427 \ \textbf{MPa}$

$\tau_{r\theta.cl} := \tau_{r\theta} = 0.763 \ \textbf{MPa}$

Transform from 60deg to 45deg

$\theta_{deg} := (45 - 60) = -15$ $\theta := \theta_{deg} \cdot \frac{\pi}{180} = -0.262$

$$\sigma_{r.cl.rot} := \frac{\sigma_{r.cl} + \sigma_{\theta.cl}}{2} + \frac{\sigma_{r.cl} - \sigma_{\theta.cl}}{2} \cdot \cos(2 \cdot \theta) + \tau_{r\theta.cl} \cdot \sin(2 \cdot \theta) = -2.734 \ \textbf{MPa}$$

$$\sigma_{\theta.cl.rot} := \frac{\sigma_{r.cl} + \sigma_{\theta.cl}}{2} - \frac{\sigma_{r.cl} - \sigma_{\theta.cl}}{2} \cdot \cos(2 \cdot \theta) + \tau_{r\theta.cl} \cdot \sin(2 \cdot \theta) = 22.123 \ \textbf{MPa}$$

$$\tau_{r\theta.cl.rot} := -\frac{\sigma_{r.cl} - \sigma_{\theta.cl}}{2} \cdot \sin(2 \cdot \theta) + \tau_{r\theta.cl} \cdot \cos(2 \cdot \theta) = -6.515 \ \textbf{MPa}$$

Sum the stresses:

$\sigma_r := \sigma_{r.plus} + \sigma_{r.cl.rot} = 21.316\ \textbf{MPa}$

$\sigma_\theta := \sigma_{\theta.plus} + \sigma_{\theta.cl.rot} = 50.386\ \textbf{MPa}$

$\tau_{xy} := \tau_{r\theta.plus} + \tau_{r\theta.cl.rot} = -9.038\ \textbf{MPa}$

Principal stresses

$\sigma_1 := \left(\frac{\sigma_r + \sigma_\theta}{2}\right) + \sqrt[2]{\left(\frac{\sigma_r - \sigma_\theta}{2}\right)^2 + \tau_{xy}{}^2} = 52.966\ \textbf{MPa}$

$\sigma_2 := \left(\frac{\sigma_r + \sigma_\theta}{2}\right) - \sqrt[2]{\left(\frac{\sigma_r - \sigma_\theta}{2}\right)^2 + \tau_{xy}{}^2} = 18.735\ \textbf{MPa}$

$\tau_{max} := \frac{\sigma_1 - \sigma_2}{2} = 17.116\ \textbf{MPa}$

$\theta_p := \frac{1}{2} \cdot \tan\left(\frac{2 \cdot \tau_{xy}}{\sigma_1 - \sigma_2}\right)^{-1} = -0.857$ Angle of principal plane (rad)

$\theta_p \cdot \frac{180}{\pi} = -49.115$ Angle of principal plane (degrees)

Tangential and Radial stress calculation WFJ T4

$b := 79\ mm$ $R_i := 3.7049\ mm$ Inner radius non-Z side

$R_{i.z} := 9.5354\ mm$ Inner radius Z-side

$r := 7.4757\ mm$ Location where crack initiated non Z-side

$r_z := 17.9605\ mm$ crack location Z-side

$t_w := 11.0 \cdot mm$ $t_{w.GOM} := 10.2453\ mm$

$t_w := t_w = 11\ mm$

$R_o := R_i + t_w = 14.705\ mm$ Outer radius assumed to be sum of inner radius + thickness.

$R_{o.z} := R_{i.z} + t_w = 20.535\ mm$

$t := R_o - R_i = 11\ mm$ Thickness deviates from 15mm nominal thickness

$F := 1.787987\ kN$ $a_{br} := 60\ mm - R_i = 56.295\ mm$ arm before radius

$M := F \cdot a_{br} = 0.101\ kN \cdot m$

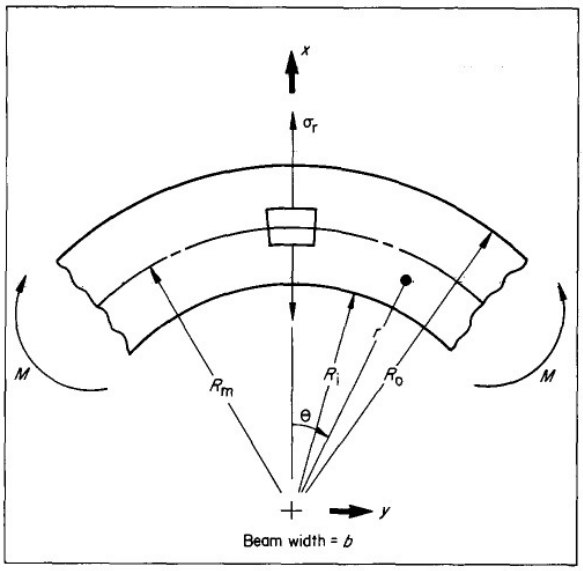

Fig. 6 Uniform moment loading on curved beam

$c := \frac{R_i}{R_o} = 0.252$ constant value 'c' needed for equation

$k := \left(\frac{1}{0.95}\right)^{\frac{1}{2}} = 1.026$ constant value 'k' needed for equation

$$g := \frac{1-c^2}{2} - \frac{k}{k+1} \cdot \frac{\left(1-c^{k+1}\right)^2}{1-c^{2k}} + \frac{k \cdot c^2}{k-1} \cdot \frac{\left(1-c^{k-1}\right)^2}{1-c^{2k}} = -0.003$$

constant value 'g' needed for equation

$$r_{max.eq} := \left(\frac{(k+1) \cdot \left(1-c^{(k-1)}\right) \cdot c \cdot \left(R_i \cdot R_o\right)^k}{(k-1) \cdot \left(1-c^{(k+1)}\right)} \right)^{\frac{1}{2k}} = 6.358 \ mm$$ Theoretical crack position

$r = 7.476 \ mm$ Actual crack position

Stress a theoretical crack position, open side

radial stress

$$\sigma_r := -\frac{M}{R_o^{\,2} \cdot b \cdot g} \cdot \left(1 - \frac{1 - c^{k+1}}{1 - c^{2k}} \cdot \left(\frac{r}{R_o} \right)^{k-1} - \frac{1 - c^{k-1}}{1 - c^{2k}} \, c^{k+1} \cdot \left(\frac{R_o}{r} \right)^{k+1} \right) = 22.834 \ \textbf{\textit{MPa}}$$

tangential stress

$$\sigma_\theta := -\frac{M}{R_o^{\,2} \cdot b \cdot g} \cdot \left(1 - \frac{1 - c^{k+1}}{1 - c^{2k}} \cdot k \cdot \left(\frac{r}{R_o} \right)^{k-1} + \frac{1 - c^{k-1}}{1 - c^{2k}} \, k \cdot c^{k+1} \cdot \left(\frac{R_o}{r} \right)^{k+1} \right) = 7.405 \ \textbf{\textit{MPa}}$$

End load on a curved beam, (next page)

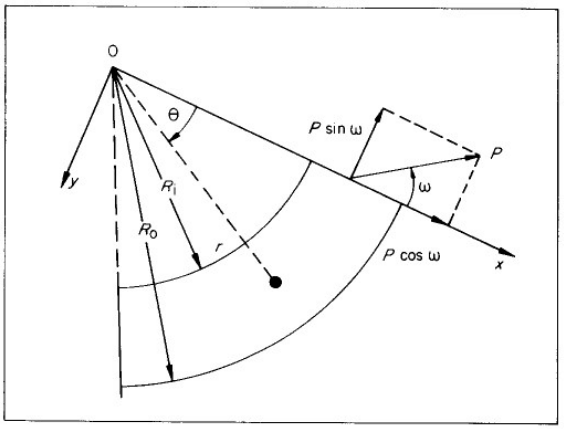

Fig. 8 Arbitrary end load on curved beam

End load on curved beam

$E_\theta := 13601.5\ \textit{MPa}$ Values from FEM

$E_{r.FEM} := 19406.89\ \textit{MPa}$ $E_r := 0.95 \cdot E_\theta = (1.292 \cdot 10^4)\ \textit{MPa}$ $\frac{E_\theta}{E_r} = 1.053$

$v_{r\theta} := 0.24$

$G_{r\theta} := 3516.921\ \textit{MPa} = (3.517 \cdot 10^3)\ \textit{MPa}$

$$\beta := \left(1 + \frac{E_\theta}{E_r}\left(1 - 2 \cdot v_{r\theta}\right) + \frac{E_\theta}{G_{r\theta}}\right)^{0.5} = 2.327$$

$$g_1 := \frac{2}{\beta}\left(1 - c^\beta\right) + \left(1 + c^\beta\right) \cdot \ln(c) = -0.61$$

$$r_{max.eq} := \left(\frac{R_o{}^\beta}{2\left(1-\beta\right)}\left(1 + c^\beta - \left(\left(1 + c^\beta\right)^2 + 4 \cdot c^\beta \cdot \left(\beta^2 - 1\right)\right)^{\frac{1}{2}}\right)\right)^{\frac{1}{\beta}} = 5.762\ \textit{mm}$$

$P := F = (1.788 \cdot 10^3)\ \textit{N}$

$\theta := \frac{\pi}{4}$ location of stress, is 45deg for open side $\omega := 0$ angel of force is 0 deg

$$\sigma_{r.P} := \frac{P}{R_o \cdot b \cdot g_1}\frac{R_o}{r}\left(\left(\frac{r}{R_o}\right)^\beta + c^\beta\left(\frac{R_o}{r}\right)^\beta - 1 - c^\beta\right) \cdot \sin(\theta + \omega) = 2.241\ \textit{MPa}$$

$$\sigma_{\theta.P} := \frac{P}{R_o \cdot b \cdot g_1}\frac{R_o}{r}\left((1+\beta) \cdot \left(\frac{r}{R_o}\right)^\beta + (1-\beta) \cdot c^\beta\left(\frac{R_o}{r}\right)^\beta - 1 - c^\beta\right) \cdot \sin(\theta + \omega) = 2.143\ \textit{MPa}$$

$$\tau_{r\theta} := \frac{-P}{R_o \cdot b \cdot g_1}\frac{R_o}{r}\left(\left(\frac{r}{R_o}\right)^\beta + c^\beta\left(\frac{R_o}{r}\right)^\beta - 1 - c^\beta\right) \cdot \cos(\theta + \omega) = -2.241\ \textit{MPa}$$

$\sigma_{r.plus} := \sigma_r + \sigma_{r.P} = 25.075\ \textit{MPa}$ $\sigma_{\theta.plus} := \sigma_\theta + \sigma_{\theta.P} = 9.548\ \textit{MPa}$

$\tau_{r\theta.plus} := \tau_{r\theta} = -2.241\ \textit{MPa}$

Stress at theorectical crack position, closed side

$R_i := R_{i.z} = 9.535\ mm$ $R_o := R_{o.z} = 20.535\ mm$

$c := \frac{R_i}{R_o} = 0.464$ constant value 'c' needed for equation

$g := \frac{1-c^2}{2} - \frac{k}{k+1} \cdot \frac{\left(1-c^{k+1}\right)^2}{1-c^{2k}} + \frac{k \cdot c^2}{k-1} \cdot \frac{\left(1-c^{k-1}\right)^2}{1-c^{2k}} = -9.008 \cdot 10^{-4}$

$k = 1.026$

$r_{max.eq} := \left(\frac{(k+1) \cdot \left(1-c^{(k-1)}\right) \cdot c \cdot \left(R_i \cdot R_o\right)^k}{(k-1) \cdot \left(1-c^{(k+1)}\right)} \right)^{\frac{1}{2k}} = 13.336\ mm$

$r := r_z = 17.961\ mm$

Moments are reversed for closed side, see diagram paper

radial stress

$\sigma_r := \frac{M}{{R_o}^2 \cdot b \cdot g} \cdot \left(1 - \frac{1-c^{k+1}}{1-c^{2k}} \cdot \left(\frac{r}{R_o}\right)^{k-1} - \frac{1-c^{k-1}}{1-c^{2k}}\, c^{k+1} \cdot \left(\frac{R_o}{r}\right)^{k+1} \right) = -6.09\ MPa$

tangential stress

$\sigma_\theta := \frac{M}{{R_o}^2 \cdot b \cdot g} \cdot \left(1 - \frac{1-c^{k+1}}{1-c^{2k}} \cdot k \cdot \left(\frac{r}{R_o}\right)^{k-1} + \frac{1-c^{k-1}}{1-c^{2k}}\, k \cdot c^{k+1} \cdot \left(\frac{R_o}{r}\right)^{k+1} \right) = 33.39\ MPa$

End load on curved beam

$g_1 := \frac{2}{\beta} \left(1-c^\beta\right) + \left(1+c^\beta\right) \cdot \ln(c) = -0.181$

$r_{max.eq} := \left(\frac{{R_o}^\beta}{2\left(1-\beta\right)} \left(1 + c^\beta - \left(\left(1+c^\beta\right)^2 + 4 \cdot c^\beta \cdot \left(\beta^2 - 1\right) \right)^{\frac{1}{2}} \right) \right)^{\frac{1}{\beta}} = 12.978\ mm$

$P = 1.788\ kN$ $r = 17.961\ mm$

$\theta := 30 \cdot \frac{\pi}{180} = 0.524$ location of stress, is 30 deg for closed side

$\omega := 0$ direction of loading force

Force dicrection is reversed for closed side, see diagram paper

$$\sigma_{r.P} := -\frac{P}{R_o \cdot b \cdot g_1} \frac{R_o}{r} \left(\left(\frac{r}{R_o} \right)^{\beta} + c^{\beta} \left(\frac{R_o}{r} \right)^{\beta} - 1 - c^{\beta} \right) \cdot \sin(\theta + \omega) = -0.72 \ \textbf{MPa}$$

$$\sigma_{\theta.P} := -\frac{P}{R_o \cdot b \cdot g_1} \frac{R_o}{r} \left((1+\beta) \cdot \left(\frac{r}{R_o} \right)^{\beta} + (1-\beta) \cdot c^{\beta} \left(\frac{R_o}{r} \right)^{\beta} - 1 - c^{\beta} \right) \cdot \sin(\theta + \omega) = 3.364 \ \textbf{MPa}$$

$$\tau_{r\theta} := \frac{P}{R_o \cdot b \cdot g_1} \frac{R_o}{r} \left(\left(\frac{r}{R_o} \right)^{\beta} + c^{\beta} \left(\frac{R_o}{r} \right)^{\beta} - 1 - c^{\beta} \right) \cdot \cos(\theta + \omega) = 1.248 \ \textbf{MPa}$$

$\sigma_{r.cl} := \sigma_r + \sigma_{r.P} = -6.81 \ \textbf{MPa}$ $\sigma_{\theta.cl} := \sigma_{\theta} + \sigma_{\theta.P} = 36.754 \ \textbf{MPa}$

$\tau_{r\theta.cl} := \tau_{r\theta} = 1.248 \ \textbf{MPa}$

Transform from 60deg to 45deg

$\theta_{deg} := (45 - 60) = -15$ $\theta := \theta_{deg} \cdot \frac{\pi}{180} = -0.262$

$$\sigma_{r.cl.rot} := \frac{\sigma_{r.cl} + \sigma_{\theta.cl}}{2} + \frac{\sigma_{r.cl} - \sigma_{\theta.cl}}{2} \cdot \cos(2 \cdot \theta) + \tau_{r\theta.cl} \cdot \sin(2 \cdot \theta) = -4.516 \ \textbf{MPa}$$

$$\sigma_{\theta.cl.rot} := \frac{\sigma_{r.cl} + \sigma_{\theta.cl}}{2} - \frac{\sigma_{r.cl} - \sigma_{\theta.cl}}{2} \cdot \cos(2 \cdot \theta) + \tau_{r\theta.cl} \cdot \sin(2 \cdot \theta) = 33.212 \ \textbf{MPa}$$

$$\tau_{r\theta.cl.rot} := -\frac{\sigma_{r.cl} - \sigma_{\theta.cl}}{2} \cdot \sin(2 \cdot \theta) + \tau_{r\theta.cl} \cdot \cos(2 \cdot \theta) = -9.811 \ \textbf{MPa}$$

Sum the stresses:

$\sigma_r := \sigma_{r.plus} + \sigma_{r.cl.rot} = 20.559$ ***MPa***

$\sigma_\theta := \sigma_{\theta.plus} + \sigma_{\theta.cl.rot} = 42.76$ ***MPa***

$\tau_{xy} := \tau_{r\theta.plus} + \tau_{r\theta.cl.rot} = -12.051$ ***MPa***

Principal stresses

$$\sigma_1 := \left(\frac{\sigma_r + \sigma_\theta}{2}\right) + \sqrt[2]{\left(\frac{\sigma_r - \sigma_\theta}{2}\right)^2 + \tau_{xy}{}^2} = 48.044 \text{ MPa}$$

$$\sigma_2 := \left(\frac{\sigma_r + \sigma_\theta}{2}\right) - \sqrt[2]{\left(\frac{\sigma_r - \sigma_\theta}{2}\right)^2 + \tau_{xy}{}^2} = 15.275 \text{ MPa}$$

$$\tau_{max} := \frac{\sigma_1 - \sigma_2}{2} = 16.385 \text{ MPa}$$

$$\theta_p := \frac{1}{2} \cdot \tan\left(\frac{2 \cdot \tau_{xy}}{\sigma_1 - \sigma_2}\right)^{-1} = -0.553$$ Angle of principal plane (rad)

$$\theta_p \cdot \frac{180}{\pi} = -31.658$$ Angle of principal plane (degrees)

Tangential and Radial stress calculation WFJ T5

$b := 76\ mm$ $R_i := 3.8442\ mm$ Inner radius non-Z side

$R_{i.z} := 7.9928\ mm$ Inner radius Z-side

$r := 6.5721\ mm$ Location where crack initiated non Z-side

$r_z := 20.0594\ mm$ crack location Z-side

$t_w := 13.4 \cdot mm$ $t_{w.GOM} := 11.9888\ mm$

$t_w := t_w = 13.4\ mm$

$R_o := R_i + t_w = 17.244\ mm$ Outer radius assumed to be sum of inner radius + thickness.

$R_{o.z} := R_{i.z} + t_w = 21.393\ mm$

$t := R_o - R_i = 13.4\ mm$ Thickness deviates from 15mm nominal thickness

$F := 2.60019\ kN$ $a_{br} := 60\ mm - R_i = 56.156\ mm$ arm before radius

$M := F \cdot a_{br} = 0.146\ kN \cdot m$

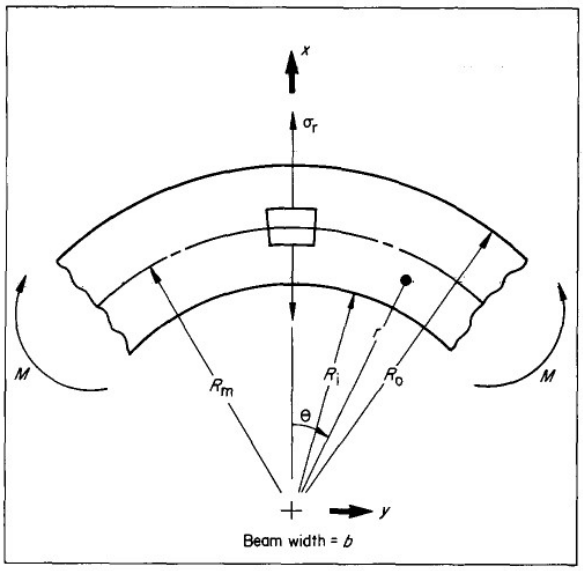

Fig. 6 Uniform moment loading on curved beam

$c := \frac{R_i}{R_o} = 0.223$ constant value 'c' needed for equation

$k := \left(\frac{1}{0.95}\right)^{\frac{1}{2}} = 1.026$ constant value 'k' needed for equation

$$g := \frac{1-c^2}{2} - \frac{k}{k+1} \cdot \frac{\left(1-c^{k+1}\right)^2}{1-c^{2k}} + \frac{k \cdot c^2}{k-1} \cdot \frac{\left(1-c^{k-1}\right)^2}{1-c^{2k}} = -0.003$$

constant value 'g' needed for equation

$$r_{max.eq} := \left(\frac{(k+1) \cdot \left(1-c^{(k-1)}\right) \cdot c \cdot \left(R_i \cdot R_o\right)^k}{(k-1) \cdot \left(1-c^{(k+1)}\right)} \right)^{\frac{1}{2k}} = 6.834 \ mm$$ Theoretical crack position

$r = 6.572 \ mm$ Actual crack position

Stress a theoretical crack position, open side

radial stress

$$\sigma_r := -\frac{M}{R_o^{\,2} \cdot b \cdot g} \cdot \left(1 - \frac{1 - c^{k+1}}{1 - c^{2k}} \cdot \left(\frac{r}{R_o} \right)^{k-1} - \frac{1 - c^{k-1}}{1 - c^{2k}} \, c^{k+1} \cdot \left(\frac{R_o}{r} \right)^{k+1} \right) = 27.088 \ \textbf{\textit{MPa}}$$

tangential stress

$$\sigma_\theta := -\frac{M}{R_o^{\,2} \cdot b \cdot g} \cdot \left(1 - \frac{1 - c^{k+1}}{1 - c^{2k}} \cdot k \cdot \left(\frac{r}{R_o} \right)^{k-1} + \frac{1 - c^{k-1}}{1 - c^{2k}} \, k \cdot c^{k+1} \cdot \left(\frac{R_o}{r} \right)^{k+1} \right) = 31.46 \ \textbf{\textit{MPa}}$$

End load on a curved beam, (next page)

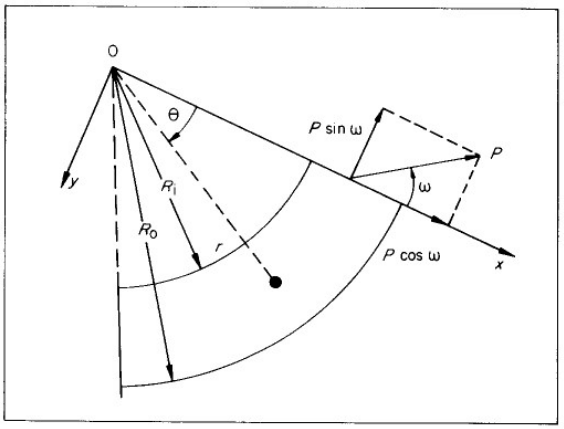

Fig. 8 Arbitrary end load on curved beam

End load on curved beam

$E_\theta := 13601.5\ \textit{MPa}$ Values from FEM

$E_{r.FEM} := 19406.89\ \textit{MPa}$ $E_r := 0.95 \cdot E_\theta = (1.292 \cdot 10^4)\ \textit{MPa}$ $\frac{E_\theta}{E_r} = 1.053$

$v_{r\theta} := 0.24$

$G_{r\theta} := 3516.921\ \textit{MPa} = (3.517 \cdot 10^3)\ \textit{MPa}$

$$\beta := \left(1 + \frac{E_\theta}{E_r}\left(1 - 2 \cdot v_{r\theta}\right) + \frac{E_\theta}{G_{r\theta}}\right)^{0.5} = 2.327$$

$$g_1 := \frac{2}{\beta}\left(1 - c^\beta\right) + \left(1 + c^\beta\right) \cdot \ln(c) = -0.713$$

$$r_{max.eq} := \left(\frac{R_o{}^\beta}{2\left(1-\beta\right)}\left(1 + c^\beta - \left(\left(1 + c^\beta\right)^2 + 4 \cdot c^\beta \cdot \left(\beta^2 - 1\right)\right)^{\frac{1}{2}}\right)\right)^{\frac{1}{\beta}} = 6.074\ \textit{mm}$$

$P := F = (2.6 \cdot 10^3)\ \textit{N}$

$\theta := \frac{\pi}{4}$ location of stress, is 45deg for open side $\omega := 0$ angel of force is 0 deg

$$\sigma_{r.P} := \frac{P}{R_o \cdot b \cdot g_1}\frac{R_o}{r}\left(\left(\frac{r}{R_o}\right)^\beta + c^\beta\left(\frac{R_o}{r}\right)^\beta - 1 - c^\beta\right) \cdot \sin(\theta + \omega) = 3.289\ \textit{MPa}$$

$$\sigma_{\theta.P} := \frac{P}{R_o \cdot b \cdot g_1}\frac{R_o}{r}\left((1+\beta) \cdot \left(\frac{r}{R_o}\right)^\beta + (1-\beta) \cdot c^\beta\left(\frac{R_o}{r}\right)^\beta - 1 - c^\beta\right) \cdot \sin(\theta + \omega) = 5.465\ \textit{MPa}$$

$$\tau_{r\theta} := \frac{-P}{R_o \cdot b \cdot g_1}\frac{R_o}{r}\left(\left(\frac{r}{R_o}\right)^\beta + c^\beta\left(\frac{R_o}{r}\right)^\beta - 1 - c^\beta\right) \cdot \cos(\theta + \omega) = -3.289\ \textit{MPa}$$

$\sigma_{r.plus} := \sigma_r + \sigma_{r.P} = 30.377\ \textit{MPa}$ $\sigma_{\theta.plus} := \sigma_\theta + \sigma_{\theta.P} = 36.925\ \textit{MPa}$

$\tau_{r\theta.plus} := \tau_{r\theta} = -3.289\ \textit{MPa}$

Stress at theorectical crack position, closed side

$R_i := R_{i.z} = 7.993\ mm$ $R_o := R_{o.z} = 21.393\ mm$

$c := \frac{R_i}{R_o} = 0.374$ constant value 'c' needed for equation

$g := \frac{1-c^2}{2} - \frac{k}{k+1} \cdot \frac{\left(1-c^{k+1}\right)^2}{1-c^{2k}} + \frac{k \cdot c^2}{k-1} \cdot \frac{\left(1-c^{k-1}\right)^2}{1-c^{2k}} = -0.002$

$k = 1.026$

$r_{max.eq} := \left(\frac{(k+1) \cdot \left(1-c^{(k-1)}\right) \cdot c \cdot \left(R_i \cdot R_o\right)^k}{(k-1) \cdot \left(1-c^{(k+1)}\right)} \right)^{\frac{1}{2k}} = 12.092\ mm$

$r := r_z = 20.059\ mm$

Moments are reversed for closed side, see diagram paper

radial stress

$\sigma_r := \frac{M}{{R_o}^2 \cdot b \cdot g} \cdot \left(1 - \frac{1-c^{k+1}}{1-c^{2k}} \cdot \left(\frac{r}{R_o}\right)^{k-1} - \frac{1-c^{k-1}}{1-c^{2k}}\, c^{k+1} \cdot \left(\frac{R_o}{r}\right)^{k+1} \right) = -3.081\ MPa$

tangential stress

$\sigma_\theta := \frac{M}{{R_o}^2 \cdot b \cdot g} \cdot \left(1 - \frac{1-c^{k+1}}{1-c^{2k}} \cdot k \cdot \left(\frac{r}{R_o}\right)^{k-1} + \frac{1-c^{k-1}}{1-c^{2k}}\, k \cdot c^{k+1} \cdot \left(\frac{R_o}{r}\right)^{k+1} \right) = 43.152\ MPa$

End load on curved beam

$g_1 := \frac{2}{\beta} \left(1-c^\beta\right) + \left(1+c^\beta\right) \cdot \ln(c) = -0.312$

$r_{max.eq} := \left(\frac{{R_o}^\beta}{2\left(1-\beta\right)} \left(1 + c^\beta - \left(\left(1+c^\beta\right)^2 + 4 \cdot c^\beta \cdot \left(\beta^2 - 1\right) \right)^{\frac{1}{2}} \right) \right)^{\frac{1}{\beta}} = 11.536\ mm$

$P = 2.6\ kN$ $r = 20.059\ mm$

$\theta := 30 \cdot \frac{\pi}{180} = 0.524$ location of stress, is 30 deg for closed side

$\omega := 0$ direction of loading force

Force dicrection is reversed for closed side, see diagram paper

$$\sigma_{r.P} := -\frac{P}{R_o \cdot b \cdot g_1} \frac{R_o}{r} \left(\left(\frac{r}{R_o} \right)^{\beta} + c^{\beta} \left(\frac{R_o}{r} \right)^{\beta} - 1 - c^{\beta} \right) \cdot \sin(\theta + \omega) = -0.336 \ \textbf{MPa}$$

$$\sigma_{\theta.P} := -\frac{P}{R_o \cdot b \cdot g_1} \frac{R_o}{r} \left((1+\beta) \cdot \left(\frac{r}{R_o} \right)^{\beta} + (1-\beta) \cdot c^{\beta} \left(\frac{R_o}{r} \right)^{\beta} - 1 - c^{\beta} \right) \cdot \sin(\theta + \omega) = 4.399 \ \textbf{MPa}$$

$$\tau_{r\theta} := \frac{P}{R_o \cdot b \cdot g_1} \frac{R_o}{r} \left(\left(\frac{r}{R_o} \right)^{\beta} + c^{\beta} \left(\frac{R_o}{r} \right)^{\beta} - 1 - c^{\beta} \right) \cdot \cos(\theta + \omega) = 0.582 \ \textbf{MPa}$$

$\sigma_{r.cl} := \sigma_r + \sigma_{r.P} = -3.417 \ \textbf{MPa}$ $\sigma_{\theta.cl} := \sigma_{\theta} + \sigma_{\theta.P} = 47.551 \ \textbf{MPa}$

$\tau_{r\theta.cl} := \tau_{r\theta} = 0.582 \ \textbf{MPa}$

Transform from 60deg to 45deg

$\theta_{deg} := (45 - 60) = -15$ $\theta := \theta_{deg} \cdot \frac{\pi}{180} = -0.262$

$$\sigma_{r.cl.rot} := \frac{\sigma_{r.cl} + \sigma_{\theta.cl}}{2} + \frac{\sigma_{r.cl} - \sigma_{\theta.cl}}{2} \cdot \cos(2 \cdot \theta) + \tau_{r\theta.cl} \cdot \sin(2 \cdot \theta) = -0.294 \ \textbf{MPa}$$

$$\sigma_{\theta.cl.rot} := \frac{\sigma_{r.cl} + \sigma_{\theta.cl}}{2} - \frac{\sigma_{r.cl} - \sigma_{\theta.cl}}{2} \cdot \cos(2 \cdot \theta) + \tau_{r\theta.cl} \cdot \sin(2 \cdot \theta) = 43.846 \ \textbf{MPa}$$

$$\tau_{r\theta.cl.rot} := -\frac{\sigma_{r.cl} - \sigma_{\theta.cl}}{2} \cdot \sin(2 \cdot \theta) + \tau_{r\theta.cl} \cdot \cos(2 \cdot \theta) = -12.238 \ \textbf{MPa}$$

Sum the stresses:

$\sigma_r := \sigma_{r.plus} + \sigma_{r.cl.rot} = 30.084$ ***MPa***

$\sigma_\theta := \sigma_{\theta.plus} + \sigma_{\theta.cl.rot} = 80.771$ ***MPa***

$\tau_{xy} := \tau_{r\theta.plus} + \tau_{r\theta.cl.rot} = -15.528$ ***MPa***

Principal stresses

$$\sigma_1 := \left(\frac{\sigma_r + \sigma_\theta}{2}\right) + \sqrt[2]{\left(\frac{\sigma_r - \sigma_\theta}{2}\right)^2 + \tau_{xy}{}^2} = 85.149 \text{ MPa}$$

$$\sigma_2 := \left(\frac{\sigma_r + \sigma_\theta}{2}\right) - \sqrt[2]{\left(\frac{\sigma_r - \sigma_\theta}{2}\right)^2 + \tau_{xy}{}^2} = 25.705 \text{ MPa}$$

$$\tau_{max} := \frac{\sigma_1 - \sigma_2}{2} = 29.722 \text{ MPa}$$

$$\theta_p := \frac{1}{2} \cdot \tan\left(\frac{2 \cdot \tau_{xy}}{\sigma_1 - \sigma_2}\right)^{-1} = -0.868$$ Angle of principal plane (rad)

$$\theta_p \cdot \frac{180}{\pi} = -49.755$$ Angle of principal plane (degrees)

Tangential and Radial stress calculation WFJ B2

$b := 81\ mm$ $R_i := 5.3362\ mm$ Inner radius non-Z side

$R_{i.z} := 6.0739\ mm$ Inner radius Z-side

Location where crack initiated non Z-side:

$r_1 := 12.052\ mm$ $r_2 := 8.9234\ mm$
$r := r_2 = 8.923\ mm$

crack location Z-side:

$r_{z.1} := 18.8725\ mm$ $r_{z.2} := 18.6664\ mm$

$r_z := r_{z.2} = 18.666\ mm$

$t_w := 16.7 \cdot mm$ $t_{w.GOM} := 15.3228\ mm$

$t_w := t_w = 16.7\ mm$

$R_o := R_i + t_w = 22.036\ mm$ Outer radius assumed to be sum of inner radius + thickness.

$R_{o.z} := R_{i.z} + t_w = 22.774\ mm$

$t := R_o - R_i = 16.7\ mm$ Thickness deviates from 15mm nominal thickness

$F_1 := 1.73215\ kN$ $F_2 := 1.6644\ kN$

$F := F_2 = 1.664\ kN$

$a_{br} := 60\ mm - R_i = 54.664\ mm$ arm before radius

$M := F \cdot a_{br} = 0.091\ kN \cdot m$

This specimen had a different failure mode and had a first crack and a second crack
After the first crack this model can not really be applied, but it will be done anyway to gain insight

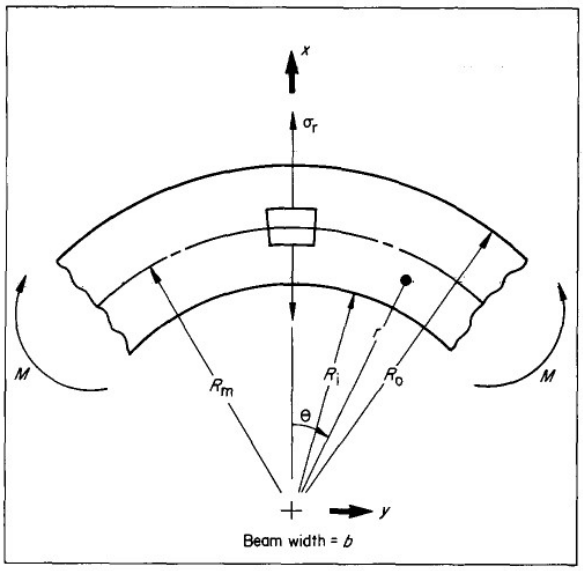

Fig. 6 Uniform moment loading on curved beam

$c := \frac{R_i}{R_o} = 0.242$ constant value 'c' needed for equation

$k := \left(\frac{1}{0.95}\right)^{\frac{1}{2}} = 1.026$ constant value 'k' needed for equation

$$g := \frac{1-c^2}{2} - \frac{k}{k+1} \cdot \frac{\left(1-c^{k+1}\right)^2}{1-c^{2k}} + \frac{k \cdot c^2}{k-1} \cdot \frac{\left(1-c^{k-1}\right)^2}{1-c^{2k}} = -0.003$$

constant value 'g' needed for equation

$$r_{max.eq} := \left(\frac{(k+1) \cdot \left(1-c^{(k-1)}\right) \cdot c \cdot \left(R_i \cdot R_o\right)^k}{(k-1) \cdot \left(1-c^{(k+1)}\right)} \right)^{\frac{1}{2k}} = 9.265 \ mm$$ Theoretical crack position

$r = 8.923 \ mm$ Actual crack position

Stress a theoretical crack position, open side

radial stress

$$\sigma_r := -\frac{M}{R_o^{\,2} \cdot b \cdot g} \cdot \left(1 - \frac{1 - c^{k+1}}{1 - c^{2k}} \cdot \left(\frac{r}{R_o} \right)^{k-1} - \frac{1 - c^{k-1}}{1 - c^{2k}} \, c^{k+1} \cdot \left(\frac{R_o}{r} \right)^{k+1} \right) = 9.524 \ \textbf{\textit{MPa}}$$

tangential stress

$$\sigma_\theta := -\frac{M}{R_o^{\,2} \cdot b \cdot g} \cdot \left(1 - \frac{1 - c^{k+1}}{1 - c^{2k}} \cdot k \cdot \left(\frac{r}{R_o} \right)^{k-1} + \frac{1 - c^{k-1}}{1 - c^{2k}} \, k \cdot c^{k+1} \cdot \left(\frac{R_o}{r} \right)^{k+1} \right) = 11.157 \ \textbf{\textit{MPa}}$$

End load on a curved beam, (next page)

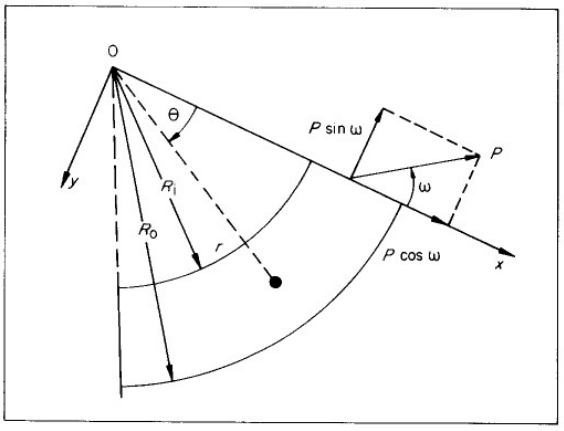

Fig. 8 Arbitrary end load on curved beam

End load on curved beam

$E_\theta := 13601.5\ \textit{MPa}$ Values from FEM

$E_{r.FEM} := 19406.89\ \textit{MPa}$ $E_r := 0.95 \cdot E_\theta = (1.292 \cdot 10^4)\ \textit{MPa}$ $\frac{E_\theta}{E_r} = 1.053$

$v_{r\theta} := 0.24$

$G_{r\theta} := 3516.921\ \textit{MPa} = (3.517 \cdot 10^3)\ \textit{MPa}$

$$\beta := \left(1 + \frac{E_\theta}{E_r}\left(1 - 2 \cdot v_{r\theta}\right) + \frac{E_\theta}{G_{r\theta}}\right)^{0.5} = 2.327$$

$$g_1 := \frac{2}{\beta}\left(1 - c^\beta\right) + \left(1 + c^\beta\right) \cdot \ln(c) = -0.643$$

$$r_{max.eq} := \left(\frac{R_o{}^\beta}{2\left(1-\beta\right)}\left(1 + c^\beta - \left(\left(1 + c^\beta\right)^2 + 4 \cdot c^\beta \cdot \left(\beta^2 - 1\right)\right)^{\frac{1}{2}}\right)\right)^{\frac{1}{\beta}} = 8.345\ \textit{mm}$$

$P := F = (1.664 \cdot 10^3)\ \textit{N}$

$\theta := 45 \cdot \frac{\pi}{180}$ location of stress, is 45deg for open side $\omega := 0$ angel of force is 0 deg

$$\sigma_{r.P} := \frac{P}{R_o \cdot b \cdot g_1}\frac{R_o}{r}\left(\left(\frac{r}{R_o}\right)^\beta + c^\beta\left(\frac{R_o}{r}\right)^\beta - 1 - c^\beta\right) \cdot \sin(\theta + \omega) = 1.552\ \textit{MPa}$$

$$\sigma_{\theta.P} := \frac{P}{R_o \cdot b \cdot g_1}\frac{R_o}{r}\left((1+\beta) \cdot \left(\frac{r}{R_o}\right)^\beta + (1-\beta) \cdot c^\beta\left(\frac{R_o}{r}\right)^\beta - 1 - c^\beta\right) \cdot \sin(\theta + \omega) = 2.615\ \textit{MPa}$$

$$\tau_{r\theta} := \frac{-P}{R_o \cdot b \cdot g_1}\frac{R_o}{r}\left(\left(\frac{r}{R_o}\right)^\beta + c^\beta\left(\frac{R_o}{r}\right)^\beta - 1 - c^\beta\right) \cdot \cos(\theta + \omega) = -1.552\ \textit{MPa}$$

$\sigma_{r.plus} := \sigma_r + \sigma_{r.P} = 11.076\ \textit{MPa}$ $\sigma_{\theta.plus} := \sigma_\theta + \sigma_{\theta.P} = 13.772\ \textit{MPa}$

$\tau_{r\theta.plus} := \tau_{r\theta} = -1.552\ \textit{MPa}$

Stress at theorectical crack position, closed side

$R_i := R_{i.z} = 6.074\ mm$ $R_o := R_{o.z} = 22.774\ mm$

$c := \frac{R_i}{R_o} = 0.267$ constant value 'c' needed for equation

$$g := \frac{1-c^2}{2} - \frac{k}{k+1} \cdot \frac{\left(1-c^{k+1}\right)^2}{1-c^{2k}} + \frac{k \cdot c^2}{k-1} \cdot \frac{\left(1-c^{k-1}\right)^2}{1-c^{2k}} = -0.003$$

$k = 1.026$

$$r_{max.eq} := \left(\frac{(k+1) \cdot \left(1-c^{(k-1)}\right) \cdot c \cdot \left(R_i \cdot R_o\right)^k}{(k-1) \cdot \left(1-c^{(k+1)}\right)} \right)^{\frac{1}{2k}} = 10.248\ mm$$

$r := r_z = 18.666\ mm$

Moments are reversed for closed side, see diagram paper

radial stress

$$\sigma_r := \frac{M}{{R_o}^2 \cdot b \cdot g} \cdot \left(1 - \frac{1-c^{k+1}}{1-c^{2k}} \cdot \left(\frac{r}{R_o}\right)^{k-1} - \frac{1-c^{k-1}}{1-c^{2k}}\, c^{k+1} \cdot \left(\frac{R_o}{r}\right)^{k+1} \right) = -3.291\ MPa$$

tangential stress

$$\sigma_\theta := \frac{M}{{R_o}^2 \cdot b \cdot g} \cdot \left(1 - \frac{1-c^{k+1}}{1-c^{2k}} \cdot k \cdot \left(\frac{r}{R_o}\right)^{k-1} + \frac{1-c^{k-1}}{1-c^{2k}}\, k \cdot c^{k+1} \cdot \left(\frac{R_o}{r}\right)^{k+1} \right) = 12.077\ MPa$$

End load on curved beam

$$g_1 := \frac{2}{\beta}\left(1-c^\beta\right) + \left(1+c^\beta\right) \cdot \ln(c) = -0.563$$

$$r_{max.eq} := \left(\frac{{R_o}^\beta}{2\left(1-\beta\right)} \left(1 + c^\beta - \left(\left(1+c^\beta\right)^2 + 4 \cdot c^\beta \cdot \left(\beta^2 - 1\right) \right)^{\frac{1}{2}} \right) \right)^{\frac{1}{\beta}} = 9.367\ mm$$

$P = 1.664\ kN$ $r = 18.666\ mm$

$\theta := 30 \cdot \frac{\pi}{180} = 0.524$ location of stress, is 30 deg for closed side

$\omega := 0$ direction of loading force

Force dicrection is reversed for closed side, see diagram paper

$$\sigma_{r.P} := -\frac{P}{R_o \cdot b \cdot g_1} \frac{R_o}{r} \left(\left(\frac{r}{R_o} \right)^{\beta} + c^{\beta} \left(\frac{R_o}{r} \right)^{\beta} - 1 - c^{\beta} \right) \cdot \sin(\theta + \omega) = -0.336 \ \textbf{MPa}$$

$$\sigma_{\theta.P} := -\frac{P}{R_o \cdot b \cdot g_1} \frac{R_o}{r} \left((1+\beta) \cdot \left(\frac{r}{R_o} \right)^{\beta} + (1-\beta) \cdot c^{\beta} \left(\frac{R_o}{r} \right)^{\beta} - 1 - c^{\beta} \right) \cdot \sin(\theta + \omega) = 0.93 \ \textbf{MPa}$$

$$\tau_{r\theta} := \frac{P}{R_o \cdot b \cdot g_1} \frac{R_o}{r} \left(\left(\frac{r}{R_o} \right)^{\beta} + c^{\beta} \left(\frac{R_o}{r} \right)^{\beta} - 1 - c^{\beta} \right) \cdot \cos(\theta + \omega) = 0.582 \ \textbf{MPa}$$

$\sigma_{r.cl} := \sigma_r + \sigma_{r.P} = -3.627 \ \textbf{MPa}$ $\sigma_{\theta.cl} := \sigma_{\theta} + \sigma_{\theta.P} = 13.007 \ \textbf{MPa}$

$\tau_{r\theta.cl} := \tau_{r\theta} = 0.582 \ \textbf{MPa}$

Transform from 60deg to 45deg

$\theta_{deg} := (45 - 60) = -15$ $\theta := \theta_{deg} \cdot \frac{\pi}{180} = -0.262$

$$\sigma_{r.cl.rot} := \frac{\sigma_{r.cl} + \sigma_{\theta.cl}}{2} + \frac{\sigma_{r.cl} - \sigma_{\theta.cl}}{2} \cdot \cos(2 \cdot \theta) + \tau_{r\theta.cl} \cdot \sin(2 \cdot \theta) = -2.803 \ \textbf{MPa}$$

$$\sigma_{\theta.cl.rot} := \frac{\sigma_{r.cl} + \sigma_{\theta.cl}}{2} - \frac{\sigma_{r.cl} - \sigma_{\theta.cl}}{2} \cdot \cos(2 \cdot \theta) + \tau_{r\theta.cl} \cdot \sin(2 \cdot \theta) = 11.602 \ \textbf{MPa}$$

$$\tau_{r\theta.cl.rot} := -\frac{\sigma_{r.cl} - \sigma_{\theta.cl}}{2} \cdot \sin(2 \cdot \theta) + \tau_{r\theta.cl} \cdot \cos(2 \cdot \theta) = -3.655 \ \textbf{MPa}$$

Sum the stresses:

$\sigma_r := \sigma_{r.plus} + \sigma_{r.cl.rot} = 8.273$ ***MPa***

$\sigma_\theta := \sigma_{\theta.plus} + \sigma_{\theta.cl.rot} = 25.374$ ***MPa***

$\tau_{xy} := \tau_{r\theta.plus} + \tau_{r\theta.cl.rot} = -5.207$ ***MPa***

Principal stresses

$$\sigma_1 := \left(\frac{\sigma_r + \sigma_\theta}{2}\right) + \sqrt[2]{\left(\frac{\sigma_r - \sigma_\theta}{2}\right)^2 + \tau_{xy}{}^2} = 26.834 \text{ MPa}$$

$$\sigma_2 := \left(\frac{\sigma_r + \sigma_\theta}{2}\right) - \sqrt[2]{\left(\frac{\sigma_r - \sigma_\theta}{2}\right)^2 + \tau_{xy}{}^2} = 6.812 \text{ MPa}$$

$$\tau_{max} := \frac{\sigma_1 - \sigma_2}{2} = 10.011 \text{ MPa}$$

$$\theta_p := \frac{1}{2} \cdot \tan\left(\frac{2 \cdot \tau_{xy}}{\sigma_1 - \sigma_2}\right)^{-1} = -0.873$$ Angle of principal plane (rad)

$$\theta_p \cdot \frac{180}{\pi} = -50.022$$ Angle of principal plane (degrees)

E

SN CURVE TEST DATA

Specimen	Juction	Load (kN)	Load per Jı	Load perce	Cycles (N)	Cycles (N)r	strain DIC (	nom_stres	fail criteria	w (mm3)	Moment (I	Moment/w
mean static		4.13	2.067	100%								
B7-B10	B7	3	1.5	70%	1		0.4	52.05	1	1564.815	81448.61	1018.108
B7-B10	B10	3	1.5	70%	1		0.379	49.31738	1	2276.574	112274.7	1439.419
B9-B4	B4	2	1	50%	1		0.275	35.78438	1631	1460.856	52275.83	661.7194
B9-B4	B9	2	1	50%	1		0.156	20.2995	1	1478.187	30006.45	365.9323
B6-B8	B6	0.8	0.4	20%	runout	2078208	0.055	7.156875	runout	1917.125	13720.63	173.6788
B6-B8	B8	0.8	0.4	20%	20004		0.181	23.55263	30006	1896	44655.78	565.263
T2-T6	T2	2.4	1.2	60%	814		0.237	30.83963	814	2671.26	82380.66	1017.045
T2-T6	T6	2.4	1.2	60%	1		0.155	20.16938	1	1994.528	40228.39	522.4466
B11-T11	B11	1.2	0.6	30%	70540		0.134	17.43675	80541	2369.185	41310.89	516.3862
B11-T11	T11	1.2	0.6	30%	runout	2759417	0.11	14.31375	runout	2334.28	33412.3	428.3628
B11-T11	T11	1.6	0.8	40%	runout	832879	0.104	13.533	runout	2334.28	31589.81	404.9976
B11-T11	T11	2	1	50%	runout	1256134	0.146	18.99825	runout	2334.28	44347.24	568.5543

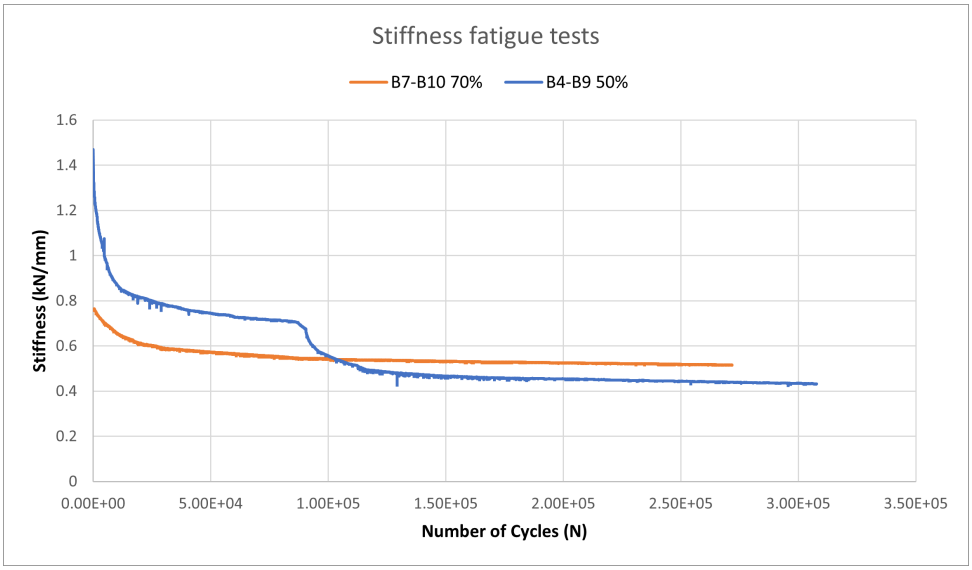

Figure E.1: Stiffness during fatigue tests 1

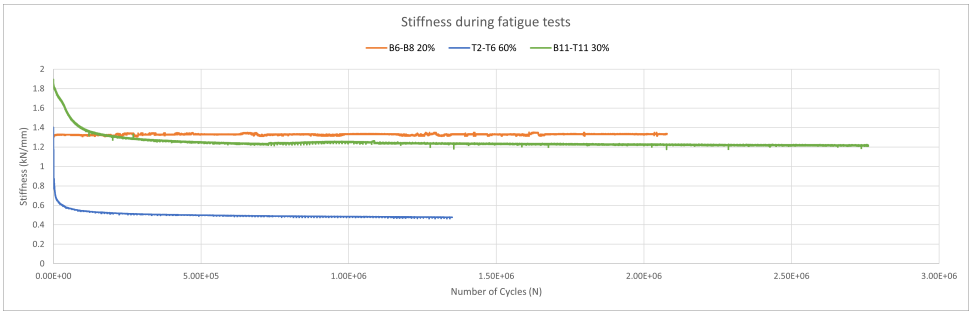

Figure E.2: Stiffness during fatigue tests 2

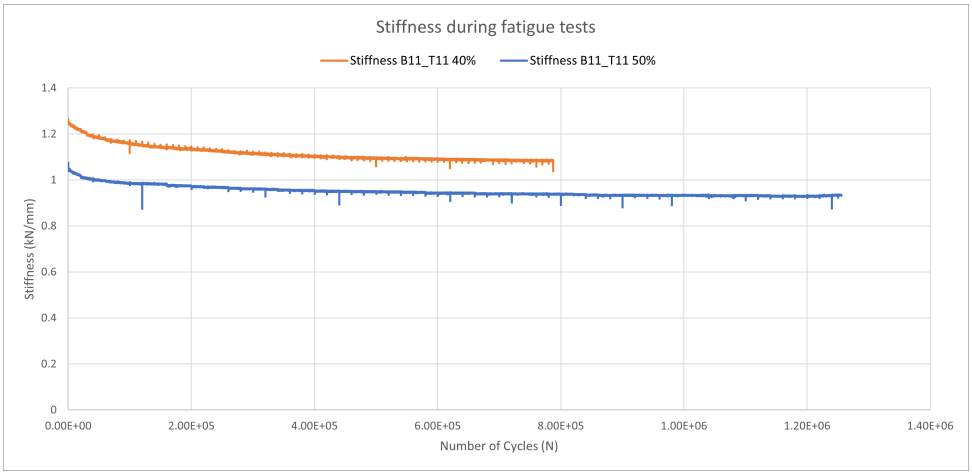

Figure E.3: Stiffness during fatigue tests 3